Evaluation of photocatalytic activity of porous films by in-situ environmental ellipsometric analysis

Ronghua Li

Université Pierre et Marie Curie

ED 397 : Physique et Chimie des Matériaux

Laboratoire de Chimie de la Matière Condensée de Paris

Evaluation of photocatalytic activity of porous films by in-situ environmental ellipsometric analysis

Par Ronghua LI

Dirigée par David GROSSO

Soutenance Prevué le 2 Mars 2016

Devant un jury composé de :

Pr. L. MALFATTI	Università degli Studi di Sassari	Rapporteur
Pr. C.COULBEAU JUSTIN	Université Paris Sud	Rapporteur
Pr. C. CHANEAC	Université de Paris 6	Examinateur
Dr. A. CATTONI	LPN-CNRS	Examinateur
Dr. M. FAUSTINI	Université de Paris 6	Invité
Pr. D. GROSSO	Aix-Marseille Université	Directeur de thèse

Contents

General Introduction

Because of their exceptional intrinsic physical chemical properties, TiO_2-based materials have been extensively studied as potential material to be used in photocatalysis, as self-cleaning optical coatings, for solar energy conversion, for energy storage, or in sensing. In particular crystalline mesoporous thin films exhibit increased photocatalytic activities due to their exceptionally high surface area and to the high number of active sites. However the study and the optimization of the photocatalysis in such porous media is not easy to be done due to the fact that the catalytic process is highly dependent from several environmental and structural parameters. In addition, most of the photocatalysis investigation techniques are performed in liquid media while in most cases TiO_2 photocatalytic films find application in air. Recently, spectroscopic ellipsometry proved to be a power tool to follow in situ photodegradation of organic species impregnated into (or in the vicinity) of TiO_2 layers during UV irradiation. In particular, the local photocatalytic activity and the radical's lifetime were deduced by monitoring the variation of refractive index of each independent layer. This simple proof of concept opened therefore wide perspectives for a comprehensive study of the photocatalysis in such medias taking into account the structural parameters of the active layer (composition, pore size, porous volume, interconnection…) and environmental conditions (UV exposure time, wavelength, humidity…).

The research activities of this thesis were essentially focused on (i) the fabrication of mesoporous TiO_2-based photoactive thin films with tunable composition and nanostructure and (ii) their utilization as platform for fundamental study of the photocatalytic process by in-situ ellipsometry. The mesoporous films with tunable nanostructure will be fabricated by coupling sol-gel chemistry, block-copolymer self-assembly and highly controlled liquid deposition techniques. Among modern analytical tools, 2D-GISAXS, ellipsometry and ellipso-porosimetry, SEM-FEG, HR-TEM and WAXS, were used to obtain a large set of relevant information on such layers.

The manuscript is organized in 4 chapters:

Chapter 1 introduces the state-of-the-art in TiO_2 materials and their photocatalytic properties in particular the case of mesoporous titinia thin films. In this regard, the notions of sol-gel chemistry, Evaporation Induced Self-Assembly (EISA) and dip-coating deposition are introduced. In the second part, we review the main characterisation techniques to evaluate the

photocatalytic activity of titania films. The in-situ ellipsometric analysis is also presented by discussing the previous studies on photocatalysis.

In Chapter 2 a model TiO_2 mesoporous film was analysed by in-situ ellipsometry for fundamental investigations of the photocatalytic process kinetics as function of the environmental composition (O_2 and humidity) and the organic pollutant (lauric acid or methylene blue). The photocatalytic efficiencies of porous thin films were evaluated by following the refractive index diminution associated to the decomposition of impregnated organic pollutants. The large amount of information obtain by in-situ ellipsometry has allowed the proposition of photodegradation mechanisms in the studied conditions.

In Chapter 3, we focus on the photocatalytic films: composite mesoporous TiO_2/SiO_2 films were fabricated by sol-gel chemistry. From the applicative point of view the goal here is to prepare photoactive films with tunable optical properties in order to be applied on optical devices or to be transparent on glass. A structural study on the films porous network and composition was conducted. In-situ ellispometry was also used to determine the photodegradation kinetics into the composite films and to clarify the photocatalytic mechanism.

In Chapter 4, the discussion of the results and some perspective are finally reported. In addition, the articles published during the thesis on the latter works are given in annex.

This work was supported by China Council Scholarship.

CHAPTER 1

Generality

1.1 Titania photocatalytic activity

1.1.1 Titania photocatalytic properties

Due to the continuously increasing world's population and the substantial development of industry, imperious demand for environment protection and production of green energy has been brought out nowadays. Semiconductor-based photocatalytic processes has shown a great potential to conquer the problem and presents additional advantages related to sustainability, cost-effectiveness and cleanness. Among these semiconductors titanium dioxide is conclusively the most promising one.

Indeed, as a non-toxic, wide band-gap (larger than 3.0 eV) semiconductor and because of its brightness, very high refractive index, and extraordinary chemical stability, titanium dioxide (TiO_2) has been widely used in the twentieth century in industries of paint, optics, cosmetics, food science, etc. Since Fujishima and Honda discovered the photocatalytic water splitting on TiO_2 electrode under ultraviolet light in 1972,[1] massive efforts have been devoted to TiO_2 material research, which led to great potential applications in areas such as photovoltaics, photocatalysis, photo and electro chromism, sensors, optics, separation, biomaterial technologies and advanced nanocomposites.[2-4]

The bandgap Eg is defined as the energy difference between the edges of the conduction and the valence bands and determines the minimum energy necessary for optical excitation. It amounts to 3.2 eV for the frequently used anatase titania crystal phase, thus indicating that only light of wavelengths shorter than 390 nm can be absorbed (Figure 1.1). The band edge positions of several semiconductors are presented in Figure 1.1.[5] The internal energy scale is given on the left in comparison to the vacuum level, and on the right in comparison to the normal hydrogen electrode (NHE).

For applications in UV-Visible spectral range (solar or artificial irradiations), semiconductors with lower band gap energy are more preferred. However, p-type low-band gap semiconductors usually suffer from serious stability problems associated to photoanodic corrosion. On the other hand, n-type semiconducting oxides are stable towards photoanodic corrosion, since they can only absorb UV light.

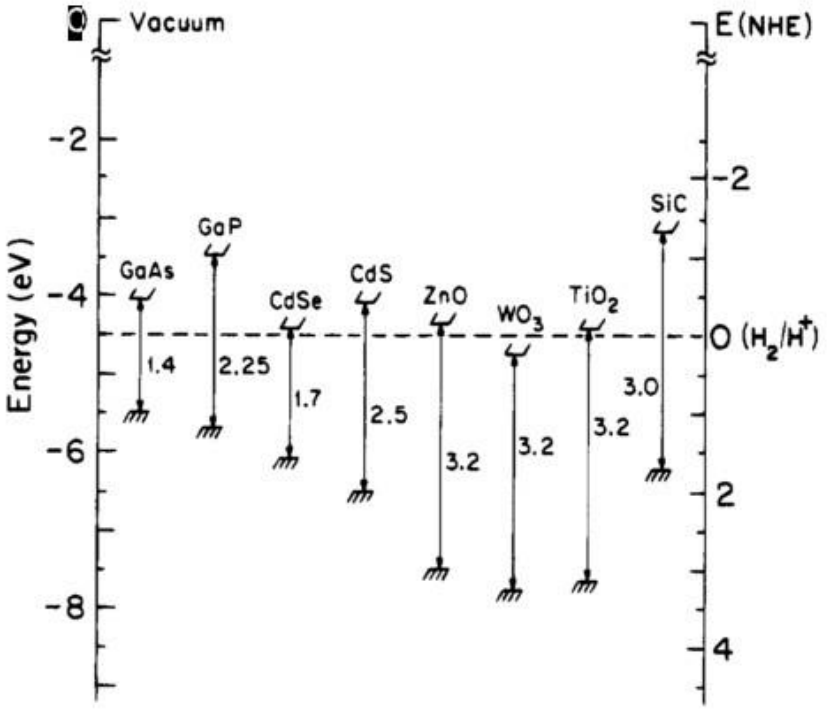

Figure 1.1 *Band-edge positions and band-gap energies of various semiconductors in aqueous electrolytes at pH=1.*[5]

Among the semiconductors shown in Figure 1.1, some could be excited by UV or visible light. The redox potentials of the edges of the valence and the conductive bands can promote series of oxidative and reductive reactions. But some of the candidates do not have long term stability. For example, the metal sulphide semiconductors, especially cadmium sulphide (CdS) and zinc sulphide (ZnS), are unstable since they undergo photoanodic corrosion. Hematite (α-Fe_2O_3) is not stable because of the photoanodic corrosion under visible light irradiation.[6] Despite a similar bang gap at 3.2 eV, ZnO is not widely employed due to its low chemical stability. It would even be photo-degraded upon excitation. Tungsten oxide (WO_3) is active in the visible region but its photocatalytic efficiency is much lower than that of titanium dioxide (TiO_2). Anatase titania appears thus to be the most attractive of this class of semicondutors and has for such reason been extensively studied in the past decades.

An analysis of the published scientific literature that indicates that research on photocatalytic materials and applications experiences a continuous growth. Figure 1.2 shows that TiO_2 is still by far the most used one,[7] even though it can only harvest ultraviolet irradiations that is to say less than 5% QA of the solar spectrum and can therefore not be used for indoor

applications where no UV irradiation is present.

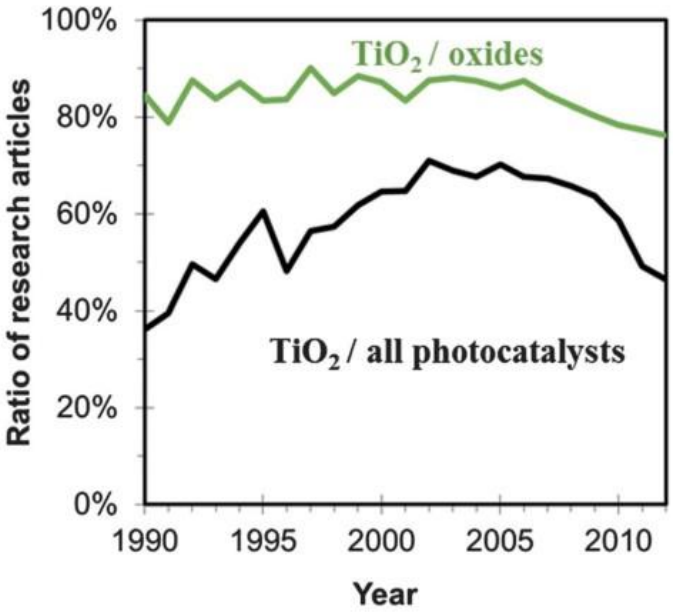

Figure 1.2 *Yearly evolution of the titania predominance in the scientific literature on photocatalysis estimated as the percentage of articles devoted to TiO_2 among those related to oxide semiconductors or out of the total. Source: Scopus.*

There are two approaches aimed at solving the problem. The first most studied strategy to develop new visible photocatalysts is to extend the absorption of TiO_2 in the visible range through the surface or bulk doping like TiO_2 doped with carbon,[8] nitrogen,[9] fluorine,[10] or sulfur.[11] However, the methods used for the doping element introduction are not fully controlled, and the low thermal stability of these compounds limits their applications. Moreover, these dopants may act as recombination centers between photogenerated electrons and holes and consequently decrease photocatalyst efficiency. Another approach is to design completely different materials that can absorb photons in the visible range.[12] For example, in our lab, photocatalytic properties of bismuth-base oxides have been investigated deeply for visible light pollutant photodegradation. As shown in table 1, bismuth-based oxides such as $BiVO_4$ and Bi_2WO_6, showed a photocatalytic activity under UV and also visible irradiation. Nevertheless, the photocatalytic efficiency of Bi_2WO_6 is low in the visible range and twice less than TiO_2 in UV range.[13-15]

Table 1. *Characteristics of the different bismuth-based oxides.*[14]

	surface area ($m^2 \cdot g^{-1}$)	band gap (eV)	RhB degradation after 2 h of irradiation (%)	stearic acid degradation formal constant ($\times 10^{-2}$ min^{-1})		
			visible light	visible light	UV LED	blue LED
$BiVO_4$-TZ	3	2.36	0	–	–	–
$BiVO_4$-TS	1	2.30	28	–	–	–
$BiVO_4$-MS	3	2.46	38	0	–	–
$BiVO_4$-X	10	2.51	29	0	–	–
$BiVO_4$-SDS	11	2.44	100[b]	1.5	110 ± 10	9 ± 1
$BiVO_4$-pH4	11	2.47	0	0	–	–
Bi_2WO_6-MW-SDS	21	2.84	–	8.5	140 ± 10	8 ± 1
TiO_2 P25	49	3.15	–	–	300 ± 40	0

[a]Note: Measurement error on surface area is 0.5 $m^2 \cdot g^{-1}$ and on band gap value is 0.01 eV. [b]RhB degradation measured at λ = 555 nm; N-de-ethylation mechanism is discussed below. UV LED: λ_{max} = 385 nm. Blue LED: λ_{max} = 445 nm.

When exited in UV, electron-hole pairs are generated in Titania. Holes could effect on organic decomposition. Because the potential of the holes in the valence band is low it can oxide most organic compounds. Applications could be roughly specified into two main fields that are environment (photocatalysis and sensing) and II) energy (photovoltaics and water splitting). Since the urgent demand in energy and clean environments, TiO_2 nanomaterials play a more and more important role and it pushes further more research based on it. The processing of titanium dioxide as thin films is required in most of these new promising fields. Especially for the application in photocatalysis, to get a high photocatalytic activity, it is necessary to use well-controlled crystalline materials with accessible mesoporosity associated high surface area. In such optimal conditions, adsorptive capacity of pollutant molecules is improved before been easily degraded.

1.1.2 Different Titania lattice structures

The commonly known polymorphs of TiO_2 occuring in nature are anatase (tetragonal, space group $I4_1/amd$, symmetry D_{4h}), rutile (tetragonal, space group $P4_2$ / mnm, symmetry D_{4h}), brookite (orthorhombic, space group $P4_2$ / mnm, symmetry D_{4h}), and TiO_2 (B) (mzonoclinic, space group C2/m). Four other Titania have been synthesized in high pressures from the rutile or anatase phases: TiO_2 (II) ("columbite", (α-PbO_2) space group Pbcn), TiO_2 (III) ("baddeleyite", space group I4/m), TiO_2 (H) ("hollandite", space group I4/m), TiO_2 (R) ("ramsdellite", space group Pbnm).[16]

Rutile is the most thermodynamically stable polymorph of TiO_2 at all temperatures, whereas

anatase and brookite are metastable phases and can be transformed into rutile by thermal treatment. Figure 1.3 shows the unit cell structures of the rutile and anatase crystals.[17] They both have tetragonal crystal structures and contain six atoms per unit cell. But the distortion of the TiO_6 octahedron of anatase is a bit larger than that of rutile. Meanwhile, the average distance between the Ti^{4+} ions for anatase is smaller, which makes it thermodynamically less stable. The metastable anatase and brookite phases can convert irreversibly to the equilibrium rutile phase upon heating above temperatures in the range 600°-800°C depending on the crystal size and the impurity content.[18]

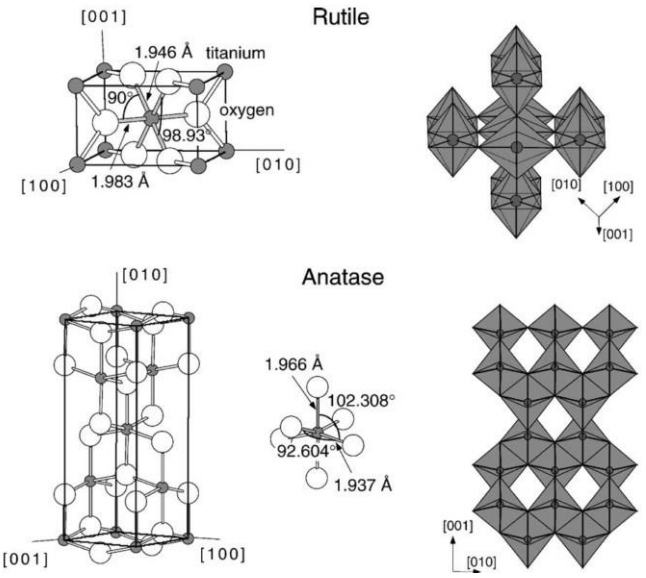

Figure 1.3 *Representations of the TiO_2 rutile and anatase forms.*[17]

The dense lattice planes in anatase is (101) followed by (100) and (001), while for rutile it is (100). As studied by UV-VIS spectroscopy, the band gap of anatase (101) was determined to be 3.2 eV compared to 3.0 eV for rutile (100).[16] The difference is due to a shift of the conduction band in anatase by 0.2 eV, whereas the position of the valence band remains unaffected.[18] On an absolute scale, the position of the anatase conduction band is given with -4.4eV.[1]

Anatase is more commonly used for photocatalytic application. It is generally considered to be more active than rutile.[17] Anatase with higher crystallinity is also preferred since it offers fewer defects acting as recombination sites between photo-generated electrons and holes.[18] The physicochemical properties of the three phases are very different from each other, and

they are closely related to the synthesis conditions. Anatase is the most thermodynamically stable among the three nanocrystalline phases if the size of the particles is less than 11 nm, brookite is the most stable phase between 11 nm and 35 nm, and rutile is the most stable when for sizes larger than 35 nm.[19] Thus, the synthesis conditions are very important and the synthesis parameters such as the crystal structure, surface morphology, and phase stability should be controlled and optimized.

1.1.3 Titania photocatalytic mechanisms

Semiconductors could be photocatalytic because of their special electronic energy structure. Differently from metals which have continuous electronic states, semiconductors possess a void energy region. This energy distance, which is called band gap, extends from the top of the filled valence band to the bottom of the empty conduction band, and makes the recombination of an electron and hole difficult. The band gap of the semiconductor gives the excited hole-electron pairs sufficient time (in the nanosecond regime) to transfer charges to the surface where adsorbed species sit and can be degraded through redox reactions. This phenomenon applied in solution or in gas phase (air environment) and is addressed as heterogeneous photocatalysis.[20]

Figure 1.4 shows a TiO_2 nanoparticle with superimposed on it a simple electronic structure of the TiO_2 valence band (VB) states, the conduction band (CB) states and the bandgap. The first step is absorption of photons to form electron-hole pairs. The heterogeneous photocatalysis activity is shown in the enlarged section of Figure 1.4. The electron from the valence band could be excited to the conductive band under energy equal to or more than the band gap of the semiconductor, which creates an electron-hole pair. Secondly, to successfully contact with the absorbate, the excited free electron has to be transferred to the surface of the semiconductor particle. The ability of it is governed by the band energy position of the semiconductor and the redox potentials of the adsorbate. The potential of accepter have to be lower (more positive) than the conductive band of the semiconductor and the potential of donor higher (more negative) than the valence band of the semiconductor.

Figure 1.4 illustrated some ways of the deexcitation pathway for the electrons and holes. The photo induced electron-hole pairs migrate to the surface of the semiconductor where they can be transfered to the absorbed species (mainly organic). Pathway C illustrates the reduction of

acceptors at the surface, happening by donating the photo induced electron to the acceptor, usually oxygen in an aerated solution. While pathway D describes at the same time the migration of the photo-induced hole to the surface to catch an electron from the donor species during its oxidation. Meanwhile, pathway A and B show the recombination of the active electron-hole pair that may happen at the surface or in the volume of the semiconductor particle. The action gives back energy releasing heat in a non-radiative transfer.

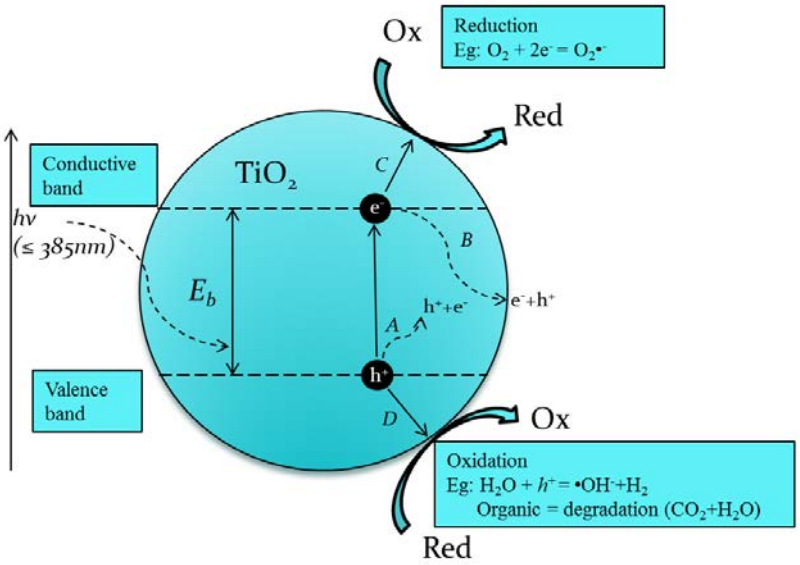

Figure 1.4 *Schematic photoexcitation in a Titania crystal followed by de-excitation events.*

Finally, the chemical reactions happening on the surface lead to the end of the heterogeneous photocatalytic mechanism. Apparently this final activity depends on the redox active sites and surface area. As well known, even though the generated electrons and holes have thermodynamically sufficient potentials, they will still have to recombine with each other if the active sites for redox reactions do not exist on the surface.[18]

Due to its enormous potential and efficiency to decompose organic contaminates (which is well known as AOP-advanced oxidation process) in water and air, semiconductor heterogeneous photocatalysis have been developed since 1970s. Numerous studies on photocatalytic oxidation process to decompose and mineralize recalcitrant organic compounds have been investigated during the past several decades.[21] Among the many semiconductor photo catalysts: TiO_2, ZnO, Fe_2O_3, CdS, ZnS, In TiO_2, the powerful electron-hole pairs occur by excitation with ultraviolet light energy higher than 3.2 eV (λ<387nm) (equal 1). These electron-hole pairs have an oxidizing potential of 2.9 eV versus NHE, which

is enough to oxidize most pollutants.

The mechanism is described in below. In equation (2) the h_{VB}^+ could catch the electron of the organic and oxide it into carbon dioxide and water finally. However, the h_{VB}^+ could generate the radicals •OH which has the second highest oxidation potential (2.8eV) (except the strongest oxidant-fluorine). Due to its electrophilic nature, the •OH radical could convert almost all the electron rich organic molecules to carbon dioxide and water (equation 4). The electron which are excited at the conductive band could react with O_2 forming an anion radical O_2•- which could lead to •OH finally through equation 6 and 7.[23]

$$TiO_2 + hv\ (<387nm) \rightarrow e_{CB}^- + h_{VB}^+ \quad (1)$$

$$h_{VB}^+ + R \rightarrow \text{intermediates} \rightarrow CO_2 + H_2O \quad (2)$$

$$H_2O + h_{VB}^+ \rightarrow \bullet OH + H^+ \quad (3)$$

$$\bullet OH + R \rightarrow \text{intermediates} \rightarrow CO_2 + H_2O \quad (4)$$

$$e_{CB}^- + O_2 \rightarrow O_2\bullet^- \quad (5)$$

$$O_2\bullet^- + 2H^+ \rightarrow H_2O_2 \quad (6)$$

$$H_2O_2 + 2h_{VB}^+ \rightarrow 2\bullet OH \quad (7)$$

R = the organic compound.

1.1.4 Factors affecting the photocatalytic activity

The photocatalytic activity is influenced by both the photocatalyst itself and the environment. Firstly, the structure of the photocatalyst decides the different energy level structure. The band gap and the species redox potential are also critical parameters. As we explained in the photocatalytic mechanism, the speed of the redox reaction depends on the potential of the acceptor and donor compare to the semiconductor band-gap.

Secondly, the electron migration is affected not only by the crystal structure, but also by the crystal crystallinity, defects and particle size which strongly affect the electron-hole transfer step as shown in figure 1.5. The boundaries and defects act as recombination centers. Better crystallized particles have fewer defects which lead to better photocatalytic activity. Mentioning about the particle size, a smaller particle offers shorter migration distance for the photogenerated electrons and holes to reach the reaction sites on the surface, decreasing the probability for recombination.[21] On the other hand, quantum confinement causes small

particle band gap to widen, blue shifting the absorption spectrum.

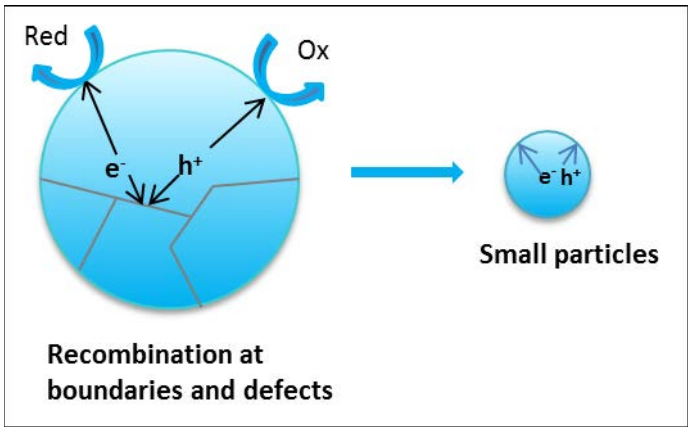

Figure 1.5 *Effect of particle size and boundary on photocatalytic activity.*

Thirdly, the photocatalytic activity of TiO_2 also dependents on surface area. Surface area acts as a favourable factor that increases the density of active sites by unit weight. In addition high surface area is needed for photocatalytic degradation because it allows faster and greater adsorption of organic compounds. It is reported that concentration of surface hydroxyl groups also affect the photocatalytic activity.[22] This is the reason why mesoporous films occur as a interesting system to integrate photocatalytic activity onto an optical surface.

Concerning environment, it is well-known that the initial concentration of the target compound, the presence of coexisting compound, the UV light intensity, the oxygen concentration, the temperature, the potential solvent (air) dynamics, the pH, and the water concentration are the main parameters affecting the degradation rate.[23,24] Concerning photocatalysis in air on films, one can imagine also that humidity and oxygen, which supply the initial redox radicals, may influence the photocatalytic activity, as it will be discussed in Chapter 2.

1.1.5 Photoinduced superhydrophilicity

Companied by photocatalytic activity, the surface of TiO_2 film turns to super-hydrophilic (Photoinduced SuperHydrophilicity (PSH)) when exposed to UV illumination, allowing both water and oil to spread.[25-29] So the surface contaminants may be detached from TiO_2 surface

if interaction between the semiconductor surface and water is preferred.

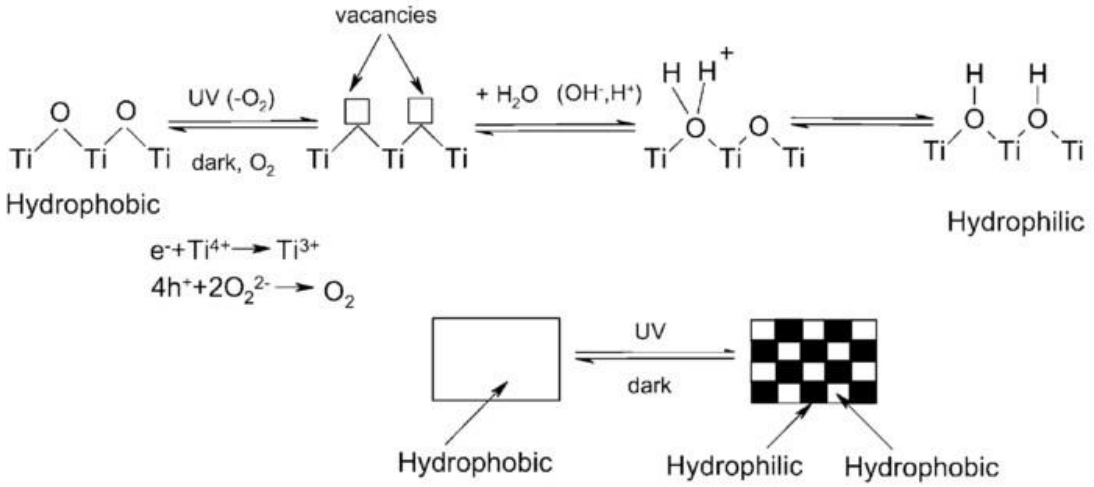

Figure 1.6 *Mechanism of photoinduced superhydrophilicity of TiO_2.*

The mechanism of PSH is illustrated in Figure 1.6.[30] PSH involves reduction of Ti(IV) cations to Ti(III) by reduction and simultaneous trapping of holes at lattice sites (usually bridging oxygen) or close to the surface of the semiconductor. Under UV irradiation, the bond between titanium and oxygen weaken and allows oxygen departure and vacancies creation. The subsequent dissociative adsorption of water at the site renders it more hydroxylated. An increased amount of chemisorbed –OH leads to an increase of hydrogen bonding interaction between H_2O and –OH. Water can easily spread across the surface and hydrophilic properties will be enhanced.[31,32] The longer the surface is illuminated with UV light, the smaller the contact angle for water becomes.[27,28] As far as the geometry of the surface is concerned, the hydrophilic properties are known to be enhanced by fine surface roughness.[31-34] By mixing the TiO_2 with oxide partners or host oxides such as SiO_2 is attempted. A study of the photocatalytic activity of the composited TiO_2/SiO_2 mesoporous film would be illustrated in Chapter 3.

1.2 Mesoporous titanium dioxide thin films

1.2.1 Introduction

As discussed in the previous section, titanium dioxide is indeed the most studied photocatalyst. New promising fields for nanostructured titania that include catalysis, information technology, non-linear optics, energy transfer devices, biomedical, selective sensors, absorbents, implant technology et al. require its processing as thin film.[35] These applications require stable materials with a well defined crystalline structure, highly controlled crystallite size and shape as well as a high, available surface area and accessible pore networks to ensure contact with catalytic substrates, polymers or nanospecies. In addition, titania thin films are transparent in the visible region, non-toxic and can be fabricated by relatively cheap wet processing methods. As high surface area is needed to get more efficiency in photocatalytic activity, it is not surprising to observe a much higher activity in mesoporous film than in dense films.[36]

Porous materials are classically classified in three types depending on their pore size. What we are more interested in are the mesoporosity, which corresponds to pore size between 2 and 50 nm. While the other two types are: microporous materials with pore sizes below 2 nm and macroporous materials with pore sizes superior to 50 nm.[37-39] Mesoporous materials can adopt different geometry (lamellar, 2D hexagonal, 3D hexagonal and cubic) depending on the processing conditions. A number of strategies lead to nanostructured TiO_2 thin films from soft chemistry methods (sol-gel).[40-44]

For a better understanding, a global stategy for the fabrication of functional coatings is shown in Figure 1.7 for the case of dip-coating technique. It consists in a sequence of successive steps that involves (i) the initial chemical solution formulation, (ii) the solution spreading on the surface of the substrate, (iii) the evaporation of the liquid solution layer, (iv) the layer post processing, and finally (v) the layer final treatment for stabilisation.

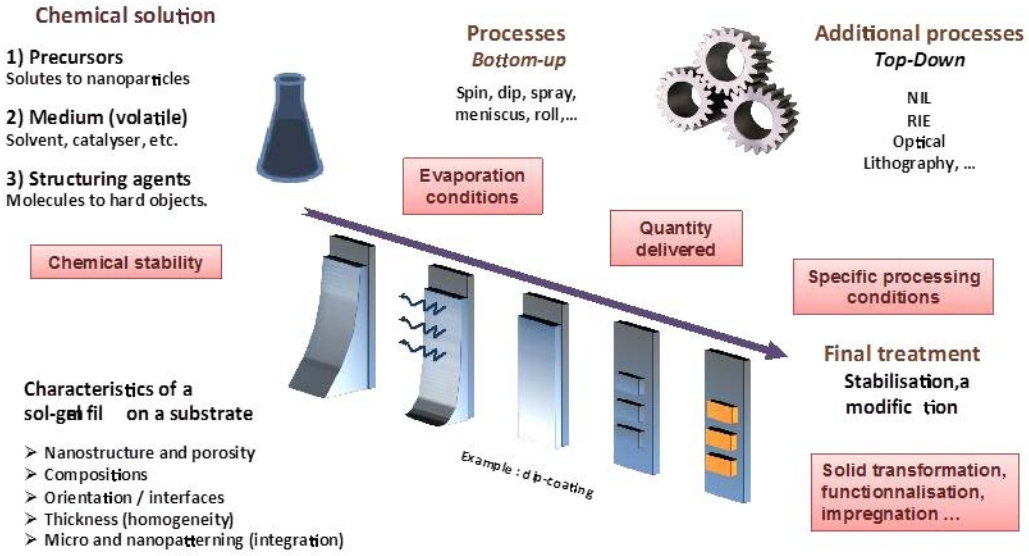

Figure 1.7 *Scheme of the various steps involved for the fabrication of functional coatings by dip-coating.*

In reality, these steps can all be individually addressed because they are separated in time, except for steps (ii) and (iii) since they are intimately linked in the space-time dimension of the processing. However, because controlling both the solution spreading and evaporation simultaneously is extremely difficult, one does his best to select conditions for which viscous flow dynamic and evaporation can be separately addressed. Step (iv) is not systematic but it can applied in multilayer systems for which a prestabilisation may be needed between each layers, or for patterning the intermediate sol-gel layer by embossing, by NIL, or by lift off approaches for instance.

Various methods of mesoporous titania thin films fabrication were developed. Two main routes, either from molecular or nanoparticulate precursors (preformed nanosized titania particle precursors[45]) or non-ionic templates (the chloride route[46], used chelating agents[47]) exist. It is reported that templating strategies represent an important advance for all the issues regarding pore control and sample homogeneity.[48] While a great amount of work was dedicated to silica,[49-52] less effort was devoted to mesoporous titania films.[53,54]

The synthesis if mesoporous titania powder was first achieved using a ligand-assisted templating route and produces channel-like or lamellar pore structure.[55,56] To control condensation, some complexing agents were explored, such as peroxide,[57] atranes[58] or alkyl amines.[59,60] However, these methods did not permit full control of pore structure, size and

distribution and were not easily extended to films. On the other hand, the preparation of thin films from $TiCl_4$ precursors, allowed a better control on the condensation due to the higher acidity of the solutions, and yield mesoporous films with an good degree of ordering.[61, 62]

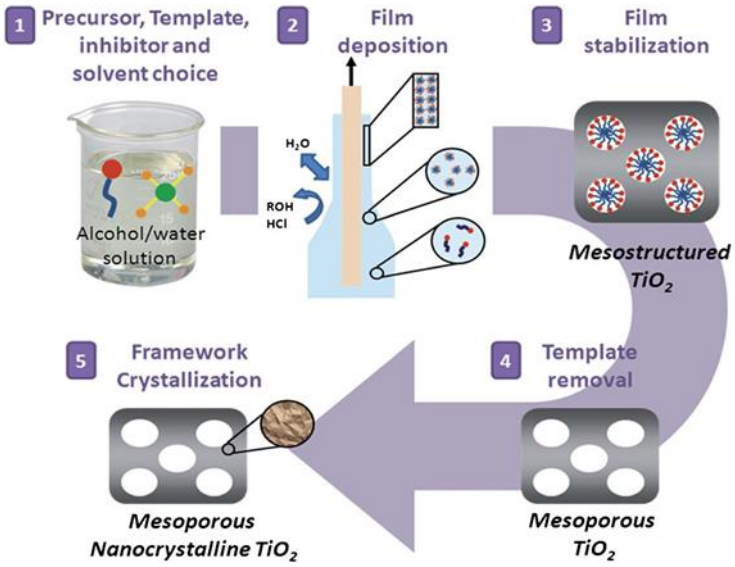

Figure 1.8 *Scheme of the sequence of steps involved in the production of mesoporous titania thin films.*[63]

For non-ionic template strategy, the mesostructuration process of TiO_2 films generally involves five important steps: 1) precursor, template, inhibitor and solvent choice and preparation of the initial solution, 2) film deposition from chemical solutions, 3) controlled post-synthesis aging, 4) template removal, 5) wall crystallization. This sequence is schematized in Figure 1.8.[63] All steps are of the same importance and all have to be well controlled in order to get well designed periodically mesoporous films. Thin film formation from chemical solutions is thus a multi-steps process that involves controls at chemistry and processing levels. The following parts are dedicated to the comprehension of the complex phenomena, taking place along the subsequent steps.

1.2.2 Initial Solution Preparation

The initial solution is of foremost important to the pore formation and is addressed as the chemical conditions. In order to fit the high curvature of the micelles during self-assembly, it is important to keep the titanium entities as small as possible and hydrophilic enough to promote the interaction with the hydrophilic part of the surfactant. It implies the following components: 1) a low surface tension solvent to improve wettability and cut back the reactivity of the inorganic species by dilution; 2) an inorganic hydrolysis/condensation agent, such as water; 3) the precursor, an inorganic species, whether molecular, cluster-like, or nanosized; 4) a supermolecular template, a surfactant, acting as porogen; 5) a condensation controlling agent or inhibitor. These chemical conditions must be fixed in order to control accurately the Ti-O-Ti bond polycondensation. There are synthesis methods for both molecular and pre-formed building blocks (nanoparticles) precursors. When using molecular precursors, the condensation is controlled by adding acidic inhibitor or chelating agents. For nanoparticle precursor, the size have to be properly controlled to a narrow distribution and make it much smaller than the gyration radius of the template.

Towards mesoporous titania thin films, $TiCl_4$ or $Ti(OR)_4$ (OR: ethoxide, i-propoxide, n-but-oxide) are most used as precursors in a classic synthesis. The solution is prepared by adding the precursor slowly into the solvent (usually ethanol solution) with vigorous stirring. When titania alkoxides are used, it is necessary to add acid or chelating agents. For both precursors (alcoxides or salts), the intermediate species are controlled by chemical equilibrium existing between the free and the coordinated nucleophilic species (z, u, v) while the ratio of condensation (x, y) is decided by the sol-gel ratio h=[H_2O]:[Ti] and p=[H+]:[Ti]. The same solution is thus obtained from different precursors, as shown:

$$TiCl_4 \xrightarrow{EtOH,\ H_2O} TiO_x(OH)_y(OH_2)_z Cl_u(OEt)_v + HCl + EtOH$$

$$Ti(OR)_4 \xrightarrow{EtOH,\ H_2O,\ HCl} TiO_x(OH)_y(OH_2)_z Cl_u(OR)_v + HCl + EtOH$$

During the synthesis of mesoporous titania, the precursors such as titanium alkoxides and titanium tetrachloride, usually goes to hydrolysis and condensation very rapidly resulting into precipitation and could not form mesopores. It's of critical important to add inhibitor to control the synthesis and condensation. So acidic species or some chelating agents has to be added for the use of $Ti(OR)_4$ precursor to control the condensation. Some chelating agents (such as acetate or diketonate) are used as efficient growth inhibitor, which induces well

ordered mesopore structure. Unfortunatly the higher content of organic leads to a greater contraction and collapse during thermal treatment. Hydrochloride acid is generally used in these conditions to prevent fast condensation (instead of organic chalting agents). HCl is however, not required for $TiCl_4$ precursor, since the solution becomes naturally very acidic upon hydrolysis. Anyway, the use of alkoxides and chlorides lead to similar intermediates as the formation of Ti(IV) species is governed by the same chemical exchanges in the same environment.

The porous system with a variety of ordering was influenced by different hydrolysis-condensation conditions (sol-gel ratio h and p). Soler-Illia, G J A A et al investigated this aspect by ^{17}O NMR of acidic titanium ethoxide solution with a different p = [H+] : [Ti(IV)] ratio.[64,65] The study showed larger signals belonging to μ2−, μ3−, μ4−oxo bridges appear in less acidic solutions (p=1), which reveal more polydisperse and more condensed, larger Ti-oxo polymers. While in more acidic solutions (p=4), a small amount of μ2-oxo bridges single signal was observed indicative of smaller building blocks more suitable mesostructuring. This was further confirmed by SAXS investigations of F127 templated films that revealed a higher mesostructure ordering with smaller, less condensed building blocks. This may due to the smaller dimensions of the blocks leading to a higher flexibility toward the template curvature during solvent evaporation when the mesostructure starts to form.[63] Aging conditions may also influences the Ti-O-Ti condensation process in solution.

Preformed nanocrystalline titania has also been used as organic precursor to obtain film with crystalline character at relatively low temperature while the molecular precursor results in amorphous or semi crystalline wall. The titania nanoparticles are produced by presynthesis after hydrolysis and condensation.

Working as a structure directing agent, the choice of the template is principally important to control the porous network and the pore size. The properties of the mesoporous films are related to the porosity %vol, pore size and pore size distribution. Most of the mesoporous titania thin films are synthesised by using structure directing templates with non-ionic hydrophilic blocks. Amphiphilic block copolymers (ABC) are particularly suitable templates which lead to ordered mesoporous materials.

Triblock copolymers [$HO(CH_2CH_2O)n-(CH_2CH(CH_3)O)m(CH_2CH_2O)nH$, Pluronic F127(average n/m=106/70) and Pluronic P123(average n/m=20/70)] are the well- known commonly used amphiphilic block copolymers as structure directing agents.

More recently tailor-made block copolymers have become more and more used. In this new family of template we can cite poly(etylene-co-butylene)-b-poly(ethylene oxide) (also called "KLE"), poly(isobutylene)-b-poly(ethylene oxide) (PIB-b-PEO), poly(styrene)-b-poly(ethylene oxide) (PS-b-PEO) and poly(butadyene)-b-poly(ethylene oxide) (PB-b-PEO); the hydrophic part is chemically and thermally more stable than the PPO family and allows the synthesis of a variety of mesoporous thin films in less drastic experimental conditions. In addition the higher hydrophobic contrast achieved in these templates gives them the ability to self-assemble faster and in a broader range of solvent.

1.2.3 Chemical Solution Deposition

A great number of different chemical, physicochemical and physical techniques could be used for preparing thin films. While physical deposition techniques are preferred for dense thin films, porous films are generally accessed by chemical solution deposition (CSD) approach, such as dip, spin, meniscus, and spray coatings. They are seen as alternatives to dry deposition techniques, such as PVD, CVD or PEVCD, because they combine excellent control of the thinner layer structure and composition rapidly and low cost. Among the various available techniques, some are already commonly used in various R&D and production industries, such as dip coating or spin coating, while others are still in their infancy and are in the process of being well understood and mastered, such as spray or ink-jet coating. Each technique has advantages and drawbacks related to reproducibility, substrate size and morphology, thickness control and homogeneity, accessibility, system handling, disposability, etc. The choice usually depends on the coating requirements and the production line.

With no doubt, dip coating is the easiest way to form a mesoporous film of optical quality. It offers the maximum control over the evaporation conditions, which permits the deposition of difficult solutions, or the control of unique characteristics (composition, mesostructure, etc.).

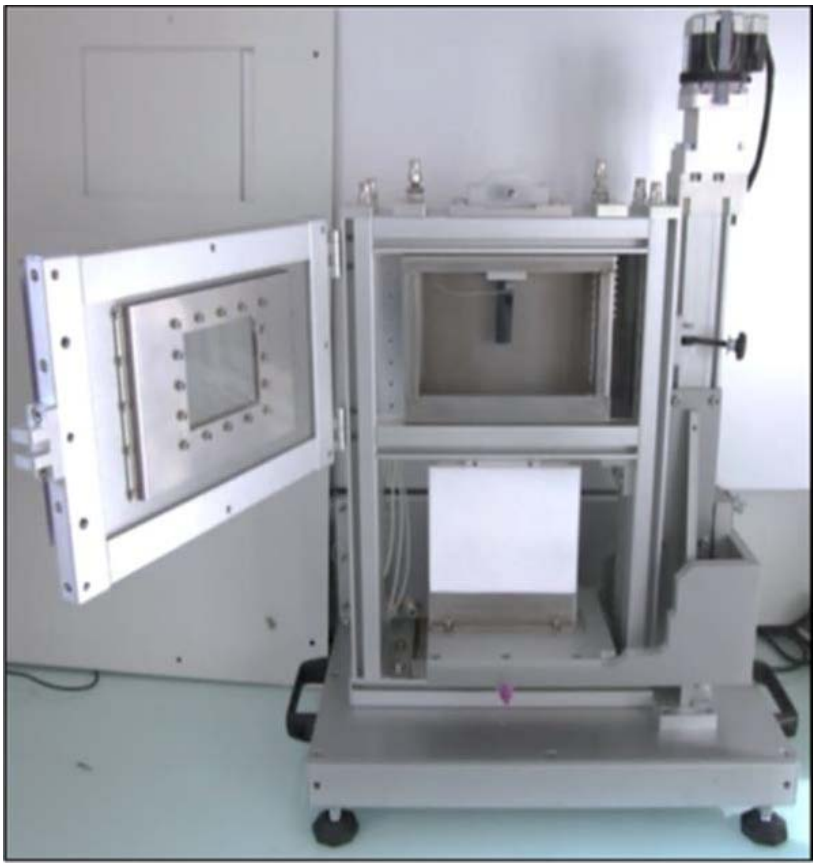

Figure 1.9 *Typical dip coater : the reservoir is isolated from the drying chamber after deposition, reservoir are slits that can assemble to allow small to large sample deposition with a minimal quantity of the solution; the high quality motor allows motion from 0.005 to 100 mm.s^{-1} (the motion can be programed to performed different thicknesses on the same sample), drying atmosphere can be controlled using a controlled gentle flux off gas and controlled temperatures up to 200°C.*

A very performing dip-coater (see Figure 1.9), has been recently built up in our lab. From a practical point of view the dip-coating technique is the simplest method to deposit a thin layer from a chemical solution. The substrate is immersed into the sol-gel solution and eventually extracted at constant speed (normally vertical), provoking the deposition of a layer of solution that cover the substrate. The fluid-dynamics involved in the formation via dip-coating are extremely complex.

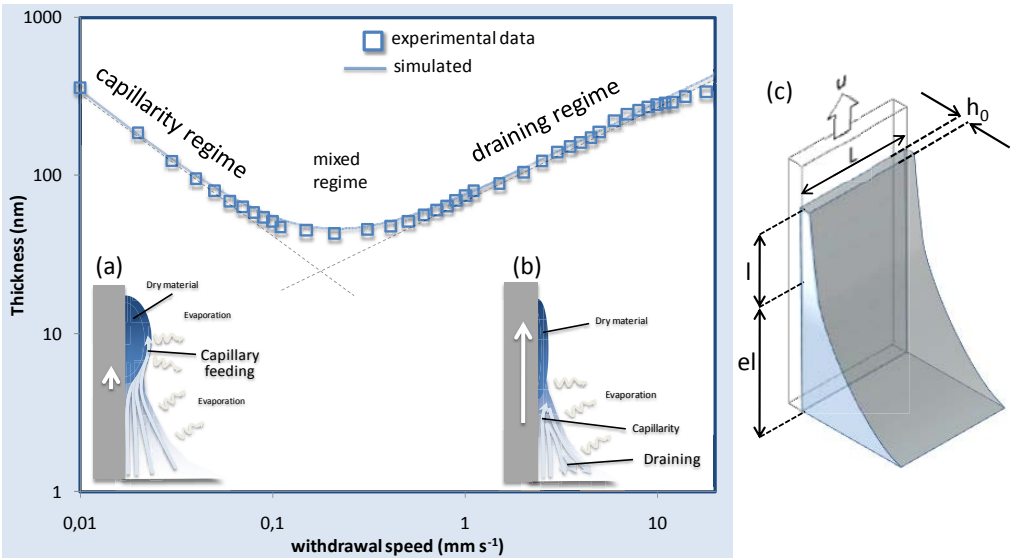

Figure 1.10 *Plot of the thickness versus withdrawal speed (log-log scale) for methyl functionalized mesoporous silica system dipped at 25°C. Inside the plot: schemes of the meniscus region for both capillarity (a) and draining (b) regimes involved at low and fast withdrawal speeds.*

Some models have been proposed to describe the formation of a homogeneous fluid layers by dip-coating. The most referred one is the Landau-Levich model[66] for which the thickness of a Newtonian and non-evaporating fluid on the surface of the substrate is described by the equilibrium between the adhesion of the fluid on the substrate and gravity induced viscous drag. However the Landau-Levich model describes only partially the behaviour for evaporating, non-Newtonian sol-gel systems. A typical plot of the evolution of film thickness versus withdrawal speed for a sol-gel derived hybrid silica is reported in Figure 1.10. For all the dipping temperatures two distinct regimes of deposition are visible for both speed extremities, while the minimal thickness is obtained for an intermediate regime. The "capillary regime" of deposition is found at speed below 0.1 mm.s^{-1}. In these conditions, the deposition is governed by the convective hydrodynamic flow induced by the faster evaporation at the triple-phases line. The "draining regime" corresponds to the conventional range of withdrawal speeds (> 1 mm.s^{-1}) where the thickness/speed dependence is fairly well described by the classical Landau-Levich model, that relies on the gravity induced viscous drag opposing the adhesion of the fluid on the substrate. Hereafter, the two regimes will be discussed in detail:

Model for the capillarity regime: At low withdrawal speeds, solvent evaporation becomes faster than the motion of the drying line (three-phases-frontier), which leads to the continuous feeding of the upper part of the meniscus by the solution through capillarity raise. In what follows, it is assumed that the evaporation rate is constant and the mass conservation law tells that the rate of film volume formation (F) can be related to the rate of solution feeding the upper zone of the drying line, which is directly related to the rate of solution undergoing evaporation (E). If c_i is the solution inorganic molar concentration and α_i the volume fraction of inorganic material in the final film, that can be deduced from the refractive index,[67] one can write:

$$F = \frac{c_i M_i}{\square_i \square_i} E = k_i E \tag{8}$$

F and E are in $m^3 s^{-1}$, while M_i and ρ_i are the molar weight and the density of the thermally stabilized inorganic material respectively. These chemical solution characteristics can be replaced by k_i, that is the material proportion constant for each solution. The rate of film formation F corresponds to the variation of film volume with time, which leads to

$$\frac{dV_f}{dt} = \frac{h_0 L dl}{dt} = \frac{c_i M_i}{\square_i \square_i} E \tag{9}$$

With V_f, h_0, l and L being the volume, the thickness, the height and the width of the considered final film respectively. Since L is constant and l varies with the withdrawal speed u=dl/dt, equation (9) can be transformed into (10).

$$h_0 = \frac{c_i M_i}{\square_i \square_i} \frac{E}{L} \frac{1}{u} = k_i \frac{E}{L} \frac{1}{u} \tag{10}$$

The h_0/k_i versus 1/u plot gives a straight line when the capillarity/evaporation regime is dominating the formation of the film, for which the slope corresponds to the rate of solution consuming E/L (in $m^2.s^{-1}$). The latter value is thus deduced experimentally, and can then be reintroduced in equation (10) to predict the thickness with respect to withdrawal rate in the capillarity regime. The latter tendency confirms that the thickness proportionally varies with u at the power -1 in these dip-coating conditions, while Le Berre et al. found a power of -1.1 with their horizontal set-up.[68]

Model for the draining regime: For high speed values, the formation of film is usually

described by the Landau-Levich equation (11) that allows to predict the thickness (h_S) of a non-evaporating Newtonian fluid (the solution here) deposited by dip-coating with respect to the fluid physical-chemical properties and the deposition processing conditions such as speed and temperature. This equation was established considering that the fluid thickness is homogeneous all over the substrate surface if the speed is constant, which is due to a delicate balance between the viscous drag and the wetting property of the fluid with the substrate surface.

$$h_s = \frac{0.94\eta_s^{2/3}}{\gamma_{LS}^{1/6}(\rho_s g)^{1/2}} u^{2/3} \tag{11}$$

η_S, γ_{LS}, ρ_S are the viscosity, the surface tension, and the density of the fluid respectively, while g is the standard gravity. In the present case the fluid is the initial solution. For the modelling one considers that the solution behaves as a Newtonian fluid (which is an approximation since the viscosity and surface tension change with evaporation that simultaneously induces concentration increase and condensation). The evaporation is taken into account by introducing the material proportion constant k_i in the equation while the physico-chemical constants of the solution are gathered into a global constant D such that equation (11), describing the fluid equilibrium thickness, becomes equation (12), describing the final film thickness, disregarding the evaporation-dependent parameters.

$$h_0 = k_i D u^{2/3} \tag{12}$$

For the Landau-Levich-based model to be verified, D must be constant whatever the value of u. D can be calculated from experimental data since one know k_i and h_0 for each speed. D values are reported for various sol-gel solutions.[66] D can be extracted from experimental points, in a range of u where D is rather constant, and can then be reintroduced in equation (10) to predict the thickness with respect to the withdrawal rate in the draining regime.

Combining models to describe simultaneous both regimes: At intermediate u values, both regime of film formation are overlapping and must be taken into account. Summing both contributions (equations (10) and (12) into equation (13)), allows a fairly well description of the final thickness with respect to the speed, suggesting that each regime does not influence significantly the other one when overlapping.

$$h_0 = k_i\left(\frac{E}{Lu} + Du^{2/3}\right) \tag{13}$$

The global evolution of the thickness described by this equation perfectly matches the experimental points, especially at intermediate u values. Since the thickness reaches a minimum value h_{0min} at intermediate critical speed u_c, the derivative of equation (13) must be null for $u = u_c$. u_c can thus be calculated using relation (13) for which $(dh_0/du) = 0$.

$$u_C = \left(\frac{2DL}{3E}\right)^{3/5} \tag{14}$$

Adjusting final thickness by dip-coating may also be achieved by playing on the dilution parameter k_i. Because viscosity does not change too much when changing the concentration in a reasonable range of a typical sol-gel solution, the thickness is quasi proportional to the initial sol-gel concentration in both capillary and draining regimes. It is thus easy to adjust the thickness if the processing conditions are fixed. On the other hand, increasing evaporation rate can be tuned by lowering partial vapor pressure of component to evaporate in the drying chamber or by simply increasing atmospheric temperature. While increasing evaporation rate has no significant effect in the draining regime, it is a critical parameter in the capillary regime. Experimental investigations confirmed that final film thickness is proportional to evaporation rate at low withdrawal speed as revealed by equation (13). It was also demonstrated that optical quality sol-gel films can be processed from pure aqueous solutions at temperatures above 40°C since surface tension of water drops down with increasing temperature, speeding up evaporation and improving the wetting properties of the solution.[69]

For a given solution, a thickness lower limit exists, that cannot be overcome except by dilution of the initial solution. On the other hand, thicker films can be obtained with highly diluted solutions at ultra-low withdrawal speeds than at high speeds. This is important when species to deposit cannot be dissolved or dispersed in high concentrations. Increasing temperature allows depositing thicker films in the capillarity regime, which is extremely be useful when the solvent is poorly volatile such as water.[69] Since any wetting solvent will give a meniscus, solvent with high surface tension such as water again can be used without dewetting problems, which are always encountered in the draining regime. Dip-coating conformation allows also to process films with one-directional thickness gradients by programming withdrawal speed along the dipping direction, which is very useful for sampling the influence of the thickness on a single substrate sample, or also to construct multi

wavelengths interferometry monochromators. Dip-coating may also be attractive because it is solution waste-free, since the whole quantity of solution that is withdrawn forms the final layer. On the other its main drawback lays in the fact that all faces of the substrate will be coated, which is not often required when manufacturing optical devices. Another drawback exists when coating in the capillary regime. Because of the slow meniscus motion, a stick-and-slip effect may occur in certain conditions, which produces periodical fluctuation in thickness. While these fluctuations are typically of only a few tens of nanometer, they are not detrimental to the film cohesion but only affect the visible aspect of the layer. This effect is thus not a problem for applications that do not require optical homogeneity such as sensors or electrodes.

1.2.4 Evaporation Induced Self-Assembly Method

Evaporation induced self-assembly method (EISA) is compatible with chemical solution deposition (CSD) techniques. Among the wide variety of synthesis strategies developed so far, evaporation induced self-assembly (EISA) method is considered of most convenient and promising method for porous film preparation which was first proposed and reported by Ogawa, Ozin's and Brinker's groups.[70-72] Other approaches such as polymer layer casting, growth at solution/air interfaces, or electrochemical deposition have been attempted with more or less success. But these methods do not ensure good reproducibility and mesostructured control as well as EISA can.

In the EISA approach, the templating agent and the inorganic precursors are gathered in the same solution, for which chemical conditions, for example composition, stoichiometry, addition of polymerization catalyst or inhibiting agent, aging time, etc., are adjusted so as to favour homogeneous dispersion of both parts. At the drying line, the film reaches a tunable steady state in which the mesostructure can be changed by the humidity or the temperature of the environment.

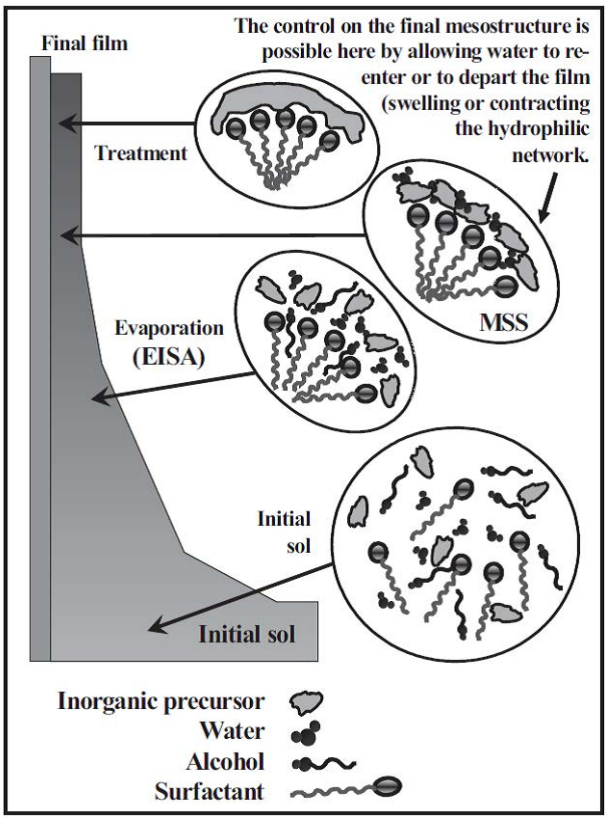

Figure 1.11 *Mesostructured thin-film formation through evaporation induced self-assembly by dip-coating.*[73]

As shown in Figure 1.11, the mechanism of EISA was reported by Grosso et al[73]. The assembly process by dip-coating can be illustrated by 4 steps. The EISA process could overlap the whole dip-coating process with the four steps. Step 1: the isotropic initial sol where the condensation is optimally slowed down. Step 2: the evaporation proceeds and micelles start to form above the CMC (critical micellar concentration). As also observed by Crepaldi and co-workers during evaporation of the ethanol-based solution, H_2O and HCl gradually concentrate during dip-coating.[74] The fast evaporation of EtOH, is accompanied by HCl and H_2O concentration and pH drop into the coating . Step 3: the evaporation is complete; the film equilibrates with its environment and the final mesostructure is selected by adjusting the RH before further inorganic condensation. The third step is also called the Tuneable Steady State (or Modulable Steady State), where the system is flexible and changes with the atmosphere composition (i.e. relative humidity), could lead to modifications of the mesostructure. Moreover, since water molecules inside thin films play an important role (micellar curvature and viscosity variations, hydrolysis of the remaining non-hydrolyzed

precursor) in the formation of the liquid-crystalline phase, the fast water equilibrium appears to be a critical point due to the competition of this process with the inorganic condensation. Step 4: the inorganic network is condensed enough so that the hybrid mesostructure is stabilized. Indeed the aim is to limit as far as possible chemical modifications and possible phase separation resulting from solubility heterogeneity between non volatile species (i.e. cations or hydrophobic organosilanes aggregation).

1.2.5 Aging

Considering the existence of a Tunable Steady State, aging freshly dip-coating films under controlled environmental humidity and temperature is a crucial step during the formation of well-ordered mesostructure.[75] Crepaldi et al introduced the typical ageing step at 50% relative humidity atmosphere. Even if the high humidity promotes template rearrangement, more than 70% humidity could destroy the meso-ordering because excessive mount of water induces high film swelling.[76] Soler-Illia et al reported that a highly ordered mesoporosity can be achieved by a prolonged treatment at RH between 20 to 50%.[63] It was reported that a purely aqueous solution, composed of only water, $TiCl_4$ and F127 leads to a similar mesoporous structure, without the need of a humidity treatment, which clearly simplifies the problem.[77] To do so, films were processed by dip-coating in warm atmosphere (40-80°C) to prevent dewetting. The high quantity of water in the solution makes obsolete the use of a humidity treatment.

However, the humidity treatment is also inducing to faster condensation of the inorganic network through elimination of HCl. In order to optimize a better process to obtain highly organized mesoporous titania thin films, a series of study was investigated that reports the influence of relative humidity on the kinetics of condensation of F127 templated mesoporous titania thin films from $TiCl_4$ precursors.[63]

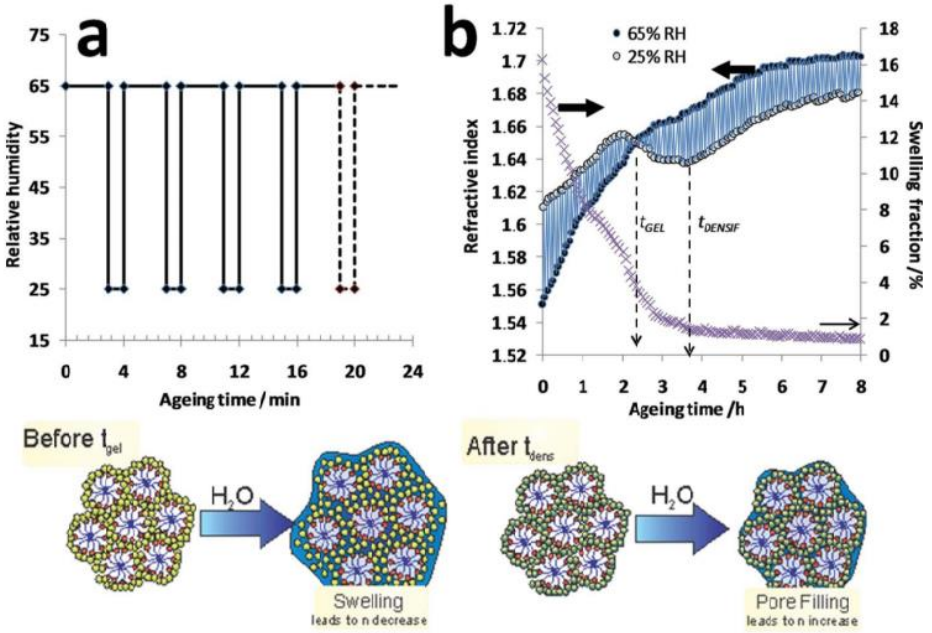

Fig. 1.12 *(a) Relative humidity variation program used in the in situ ellipsometry ageing of a freshly deposited titania–template film; $TiCl_4$ was used as precursor, and F127 as the template; (b) refractive index at 633 nm (left axis) and film swelling fraction upon RH change from 25% to 65% (right axis) plotted versus ageing time at 30°C. Closed symbols: n633 at 65%RH; open symbols: n633 at 25%RH. Arrows mark the t_{gel} and t_{dens}, see discussion in the text. Upon water uptake, mesostructure swelling or pore filling processes take place depending on the framework condensation, as sketched in the lower part.*[63]

After dip-coating, films were immediately aged within an environment chamber where the temperature was maintained at 30°C and the humidity was cycled between 65% to 25%. The thickness and refractive index variations induced by the latter cycling were monitored using in situ ellipsometry. As shown in Figure 1.12, the film swells and its refractive index decreases significantly for high humidity, while the reverse occurs at low humidity. The swelling amplitude and the difference in refractive tends to decrease with time which is attributed to the condensation of the inorganic matrix. At t_{gel} (a definition time for gel condensation), the variation of refractive index reverse its tendency suggesting that the porosity starts to be created into the material. At t_{dens} (a definition time for rigid structure which means no more contraction), the swelling becomes even less and the mean refractive index increases with ageing time suggesting a densification through extended condensation of the network. After t_{dens} one may consider the structure to be locked into its final structure.

This experiment confirms that the as-prepared mesostructure is indeed alive and responds to humidity through adsorption into the material. Infiltrated water modifies the thickness and the chemical reactions of condensation through elimination of HCl. An optimal aging time exists at t_{dens}. This time depends on the temperature and can be considerably reduced for slightly higher temperature as a result of faster molecular exchange (2 or 3 minutes is enough above 34°C). In such conditions, mesoporous TiO_2 films with a relatively high porosity and with narrow pore size distribution can be prepared in a faster way. Interestingly, the porosity appears to be highly accessible since large constrictions are present. In this thesis, this approach will be used to prepare the TiO_2 films.

1.2.6 Crystallization by thermal treatment

As well known for many applications the accessible porosity and the crystallized titania structure are both critical factors. Fortunately, these properties could be controlled by thermal treatment. In our group, a in-situ thermal ellipsometric analysis, was conducted on F127 templated TiO_2 mesoporous films as shown in Figure 1.13 A). It was first demonstrated that below 200°C, structure consolidation occurs through condensation and water evaporation, which cost a z-axis shrinkage about ca. 25%-35%.[78] Secondly, between 250°C and 350°C, the F127 template is removed and the porosity is generated together with a further densification of the inorganic network, which causes an additional z-axis uniaxial shrinkage of ca. 20%-30%. Thirdly, above 350°C, crystallite nucleation takes place and growth followed by diffusive sintering. [78-80]

The control of the thermal treatment step is of crucial importance for obtaining the desired mesoporous nanocrystalline final material. As suggested by D. Grosso et al., a short time thermal treatment at high temperature[78] is favoured to get the confined nanocrystals since it favours fast nucleation, which was confirmed by Kirsch et al.[81] A one dimensional diffusion controlled crystallite growth would take place along with the fast nucleation. After that, it is noted that the thermal heating rate may not be a crucial factor for crystalline growth because of a low-dimensional diffusion-controlled regime.[82]

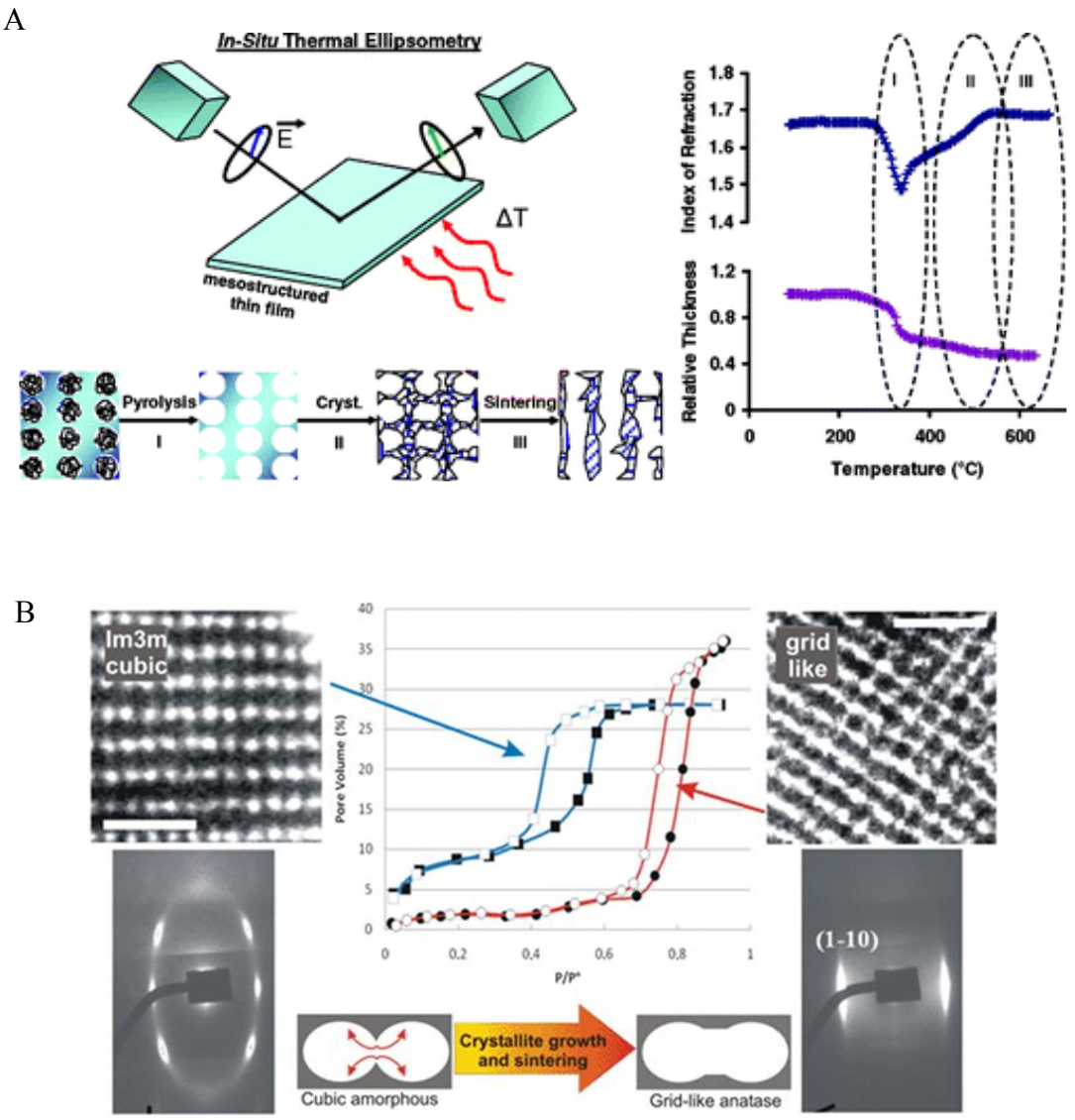

Figure 1.13 *A) In-situ thermal ellipsometry scheme (left), evolution of refractive index and thickness vs temperature (right). B) Evolution from a cubic pore symmetry obtained at 350 °C (left) to grid-like pores obtained at a short treatment at 600 °C (right) mesostructure upon thermal treatment, as witnessed by TEM, SAXS and EP. Scale bars represent 50 nm.*

This morphological evolution can be visualized in Figure 1.13 (B) (nanoscale ref. For example, a (110) oriented cubic Im3m structure (obtained at 350°C) experiences successively unidirectional shrinkage, nucleation-growth and diffusive sintering when heated at 600°C. This leads to pore merging in the direction where the interpore walls are thinner. The resulting structure can be defined as a "grid-like" structure. This structure is recognised by the GI-SAXS diffraction signals corresponding to the lateral periodicity derived from the (1–

10) cubic peaks at $q_z = 0$ (Figure 1.13 B). As a result of the sintering process, the film interpore connectivity is modified as proven by the observed evolution of the adsorption /desorption isotherms. The cubic structure obtained at 350 °C presents an wide hysteresis loop, typical of mesopores with restrictions. The adsorption-desorption curve of a grid-like mesostructure obtained after a short thermal treatment to 600 °C presents a narrow loop with parallel branches that is similar to the ones obtained for open-ended cylindrical pores.

1.3 Photocatalytic characterization of TiO_2 films

1.3.1 Introduction

The photocatalytic efficiency of mesoporous titania films is usually investigated through impregnation of an organics probe into the porosity and monitoring of its degradation upon UV irradiation. Many methods based on various types of probes and on various types of analysis technique have been explored, which all present advantages and drawbacks. Dyes are commonly used as model pollutants, partly because their concentration can be easily monitored using a spectrometer. However, it was also studied that as dyes absorb light, especially in the visible range, the influence of this photoabsorption should be excluded for evaluation of the real photocatalytic activity of photocatalysts.[83] Another alternative would be to use fluorescent probes for which emission variation can be followed spectroscopically (7-hydroxycoumarin by coumarin and 2-hydroxyterephthalic acid by terephthalic).[84] The characteristic study of photocatalytic activity of TiO_2 thin films varies with the different probes. With impregnated dyes, one would use UV-Visible spectroscopy,[80] while with impregnated fluorescent probes, the photocatalytic activity could be studied by fluorescence spectroscopy.[85] With adsorbed lauric acid, the photocatalytic activity can be monitored though the variation of water contact angle at the TiO_2 thin film surface.[80]

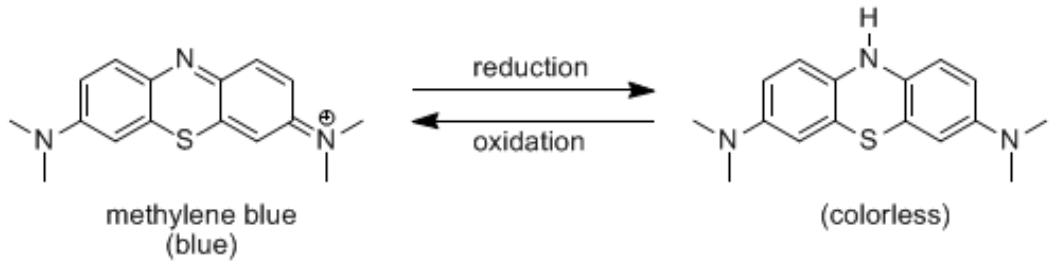

(1)

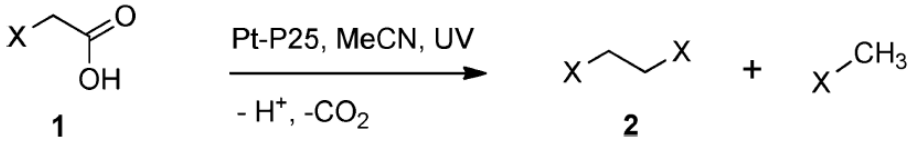

(2)

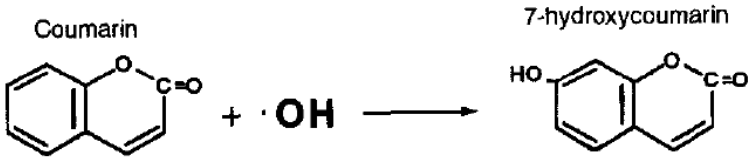

(3)

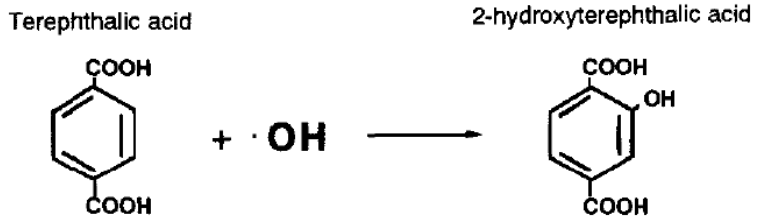

(4)

Figure 1.14 *Examples of formation of products as the result of the reactions between the probe molecules and the electron-hole pairs or radicals: (1) reaction of mathelyne blue (3) reaction between •OH and coumarin; (4) reaction between •OH and terephthalic acid.*

Lauric acid was selected as probe in our study (chapter 2 and chapter 3), as it's physical-chemical properties make simple its homogeneous infiltration and stabilization within mesoporous films.[86,87] Also because the decomposition of carboxylic acids of the same type at TiO_2 interfaces under UV radiation has been extensively studied.[88] By analogy with the photo-Kolbé reaction, The first step was expected to be hole capture by the carboxylic acid at the TiO_2 surface to generate the corresponding radical cation.[89,90] Loss of a proton would then generate an alkyloxyl radical, $RCH_2C(O)O•$, which would rapidly eject CO_2 to produce an alkyl radical, $RCH_2•$.[91-94] Lauric acid could also generate water among the photocatalysis,

which could accelerate the organic decomposition.

In the following, some techniques for photocatalytic characterize are first introduced before exposing the ellipsometry measurement approach that has been used in the present study.

1.3.2 Photocatalytic characterization techniques

1.3.2.1 UV-visible absorption spectroscopy

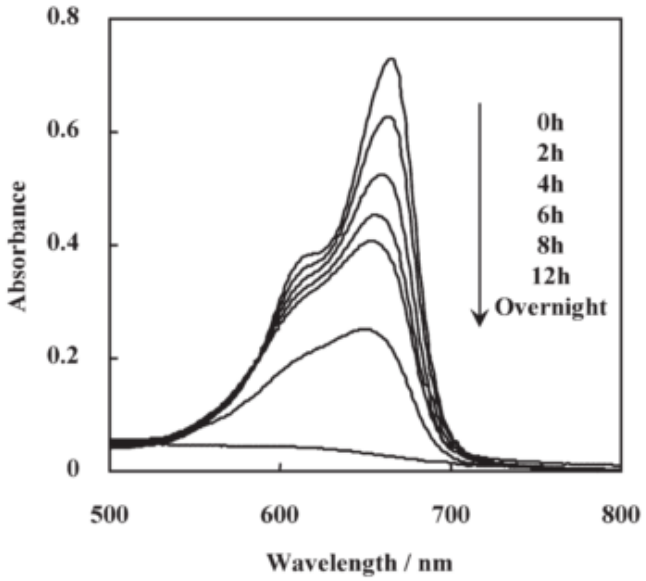

Figure 1.15 *Variation of absorption spectra of MB-TiO_2 films calcined at 600°C upon UV irradiation.*[80]

Ultraviolet-visible spectroscopy or ultraviolet-visible spectrophotometry (UV-Vis) refers to absorption spectroscopy or reflectance spectroscopy in the ultraviolet-visible spectral region. The absorption of light in the visible range directly affects the perceived colour of the chemicals involved. In this region of the electromagnetic spectrum, molecules undergo electronic transitions from the ground state to the excited state. Many molecules absorb ultraviolet or visible light. Absorbance is directly proportional to the path length and the concentration of the absorbing species. Beer's law states that $A = \varepsilon bc$, where ε is a constant of proportionality, called the absorptivity, b is the path length and c is the concentration of the absorbing species.

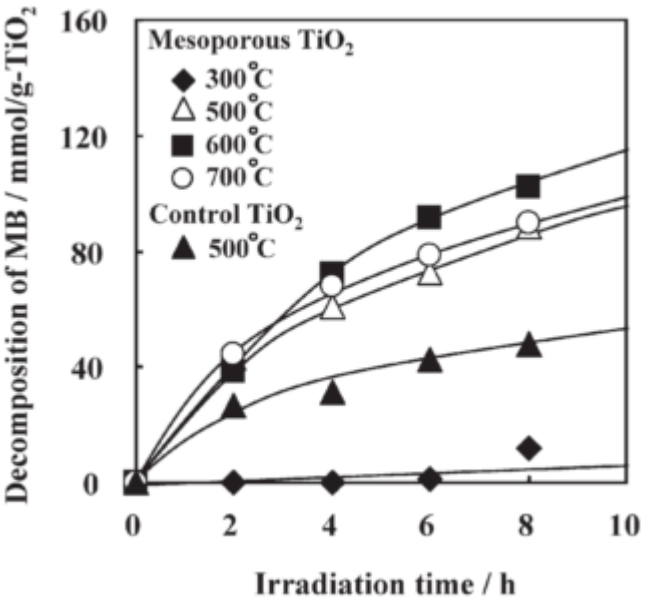

Figure 1.16 *Photodegradation of MB over TiO_2 films calcined at various temperatures under UV light irradiation.*[80]

Different molecules absorb radiation of different wavelengths. An absorption spectrum will show a number of absorption bands corresponding to structural groups within the molecule. The variation of a specific absorbance (peak of absorption) is used to determinate the degradation percentage (%) of the associated molecular probe using the following equation:

$$\mathrm{D} = \frac{A_0 - A_t}{A_0} \times 100\% \qquad (15)$$

Where D is degradation percentage, A_0 and A_t are the absorbance of the samples at UV irradiation time 0 and t, respectively. UV-Visible spectroscopy has been used to detect, for the first time, the photocatalytic activity of mesoporous TiO_2 films by study the absorption spectra of MB solution under UV light irradiation.[80,95]

As the photocatalytic reaction proceeded, the amount of MB decreased while a blue shift of the maximum peak around 650-665 nm was observed, which is caused by photo oxidative N-demethylation of MB resulting from the production of intermediate species. The amount of MB decomposition over mesoporous TiO_2 is deduced from the corresponding absorption band decrease as shown in Figure 1.15. In that study[80] and as illustrated in Figure 1.16, the photocatalytic efficiency of the mesoporous TiO_2 films was investigated for different

calcination temperatures. It has demonstrated that samples obtained at 600°C showed the best photocatalytic activity due to the ideal combination of good crystalline network and highly accessible porosity.

1.3.2.2 Fluorescence spectroscopy

Fluorescence spectroscopy (also known as fluorometry or spectrofluorometry) is a type of electromagnetic spectroscopy which analyses fluorescence from a sample. It involves a beam of light, usually UV, that excites electrons of certain valence orbitals into orbitals of higher energy, which then emit a photon of lower energy upon relaxation. Fluorescence spectroscopy was used for the determination of the photocatalytic activity. K. Ishibashi et al. have adapted the use of coumarin or terephthalic acid solution to measure •OH production on TiO_2 photocatalysis. The method relies on the fluorescent signal generated by the hydroxylation of coumarin or terephthalic acid. Then the tentative detection of •OH generated at the water/TiO_2 interface was suggested based on the technique.[96]

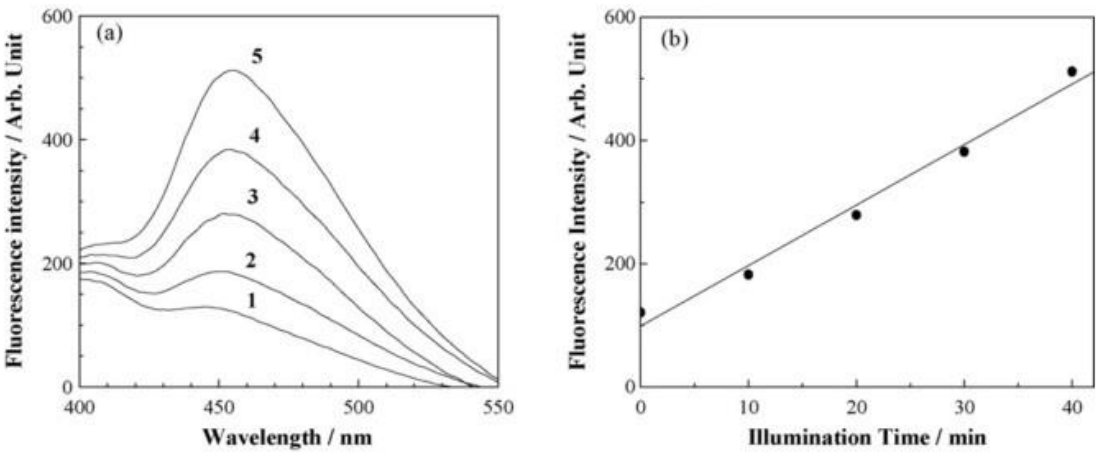

Figure 1.17 *Fluorescence spectra of coumarin solution (1.0μmolL^{-1}, pH3) after light illumination of (1) 0, (2) 10, (3) 20, (4) 30, and (5) 40min on P25-coated glass slide and (b) the time dependence of the flurescence intensity at 456nm.*[84]

Guan H. et al. also proposed this technique as a faster way to evaluate the photocatalytic activity of self-cleaning materials compared to conventional dye methods.[84] They used the 7-hydroxycoumarin as probe which is generated by illumination of coumarin and well

correlated to the results obtained by dye method (see figure 1.17). The photocatalytic activity of self-cleaning materials was able to be simply probed using the fluorescence and requires only 40 min, which is much less than 250 min required for a dye method (see figure 1.18).

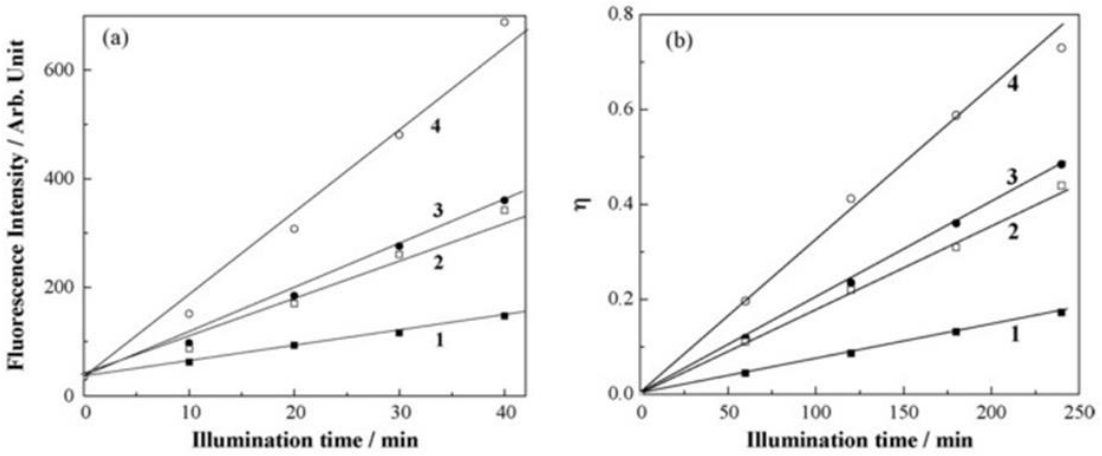

Figure 1.18 *Performance evaluation of self-cleaning materials coated with (1) TiO_2, (2) TiO_2-500, (3) P25, and (4) TiO_2/SiO_2 films, by using (a) fluorescent probe method and (b) methyl orange method.* [84]

1.3.2.3 Gas chromatography and mass spectroscopy

Gas Chromatography and Mass Spectroscopy (GC-MS) is the combination of GC and MS. In this experiment the media must be gas. The GC-MS is composed of two major building blocks as shown by Figure 1.19: the gas chromatograph and the mass spectrometer. The gas chromatograph utilizes a capillary column with characteristics (length, diameter, stationary phase properties…) that varies depending on its specificity for selectivity. The difference in the chemical properties between different molecules in a mixture and their relative affinity for the stationary phase of the column will promote separation of the molecules as the sample travels the length of the column. The molecules are retained by the column and then elute (come off) from the column at different times (called the retention time), and this allows the mass spectrometer downstream to capture, ionize, accelerate, deflect, and detect the ionized molecules separately. The mass spectrometer does this by breaking each molecule into ionized fragments and detecting these fragments using their mass-to-charge ratio.

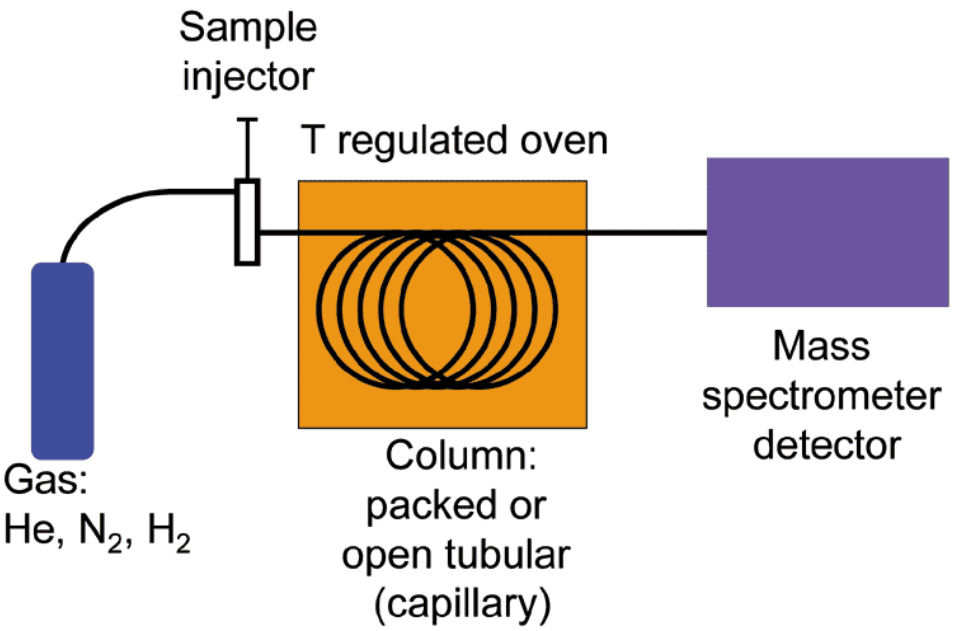

Figure 1.19 GC-MS Schemetic

The GC-MS technique has been widely used for analysis of organic intermediates or the final products of typical photocatalytic reactions.[97-99] The photocatalytic activity was just deduced by detecting the photocatalytic decomposition products of the pollutants. The products are either in solution or gas. The product was collected by evaporation (solution) or by a gas collection setup. By detecting the product components and the concentration, it is possible to analyze the photocatalytic activity. Taking a study as an example, in figure 1.20, the TiO_2 photocatalytic oxidation of benzene was tested by GC-MS. The evolutions of Benzene conversion with time under different water vapour conditions were got by detecting the concentration of benzene by GC-MS. The result indicated that water vapour presence is necessary for continued high benzene conversion, which represented photocatalytic activity. The study extracted the byproducts of the elimination and identified them by GC-MS method, which illustrated an attractive capability of the pretrated TiO_2/H_2O or TiO_2/HCl material for air purify.[97]

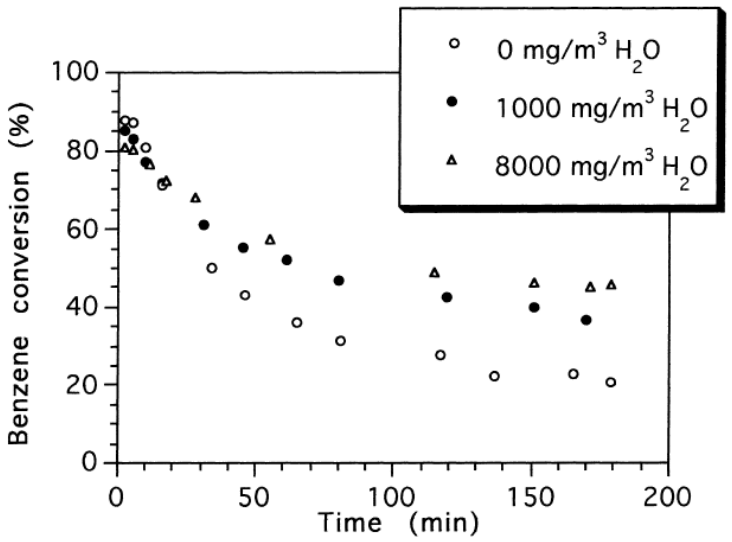

Figure 1.20 *Benzene conversion over untreated TiO_2 vs. time. $[Benzene]_0$ = 50 ± 2 mg m^{-3} (15.7 ppmv), flow rate = 1 cm^3 s^{-1}.*[97]

1.3.2.4 Fourier-Transform Infrared Spectroscopy

Fourier-transform infrared spectroscopy, shorted by FTIR, is the preferred method of infrared spectroscopy. In infrared spectroscopy, IR radiation is passed through a sample. The resulting spectrum represents the molecular absorption and transmission, creating a molecular fingerprint of the sample. Like a fingerprint no two unique molecular structures produce the same infrared spectrum. This makes infrared spectroscopy useful for several types of analysis.

As the FTIR technology could provide information of the unknown materials, the quality or consistency of a sample and also the amount of components in a mixture, the investigation of photocatalytic activity by it was carried out by detecting the changing of intensity of one or some certain collaboration bands of the organic probes. The technique has been used to study the photocatalytic decomposition of stearic acid and of Pluronic (F127) at different temperatures.[100] The analysis of the FTIR spectra adsorption band variation of Pluronic F127 upon irradiation time is shown in Figure 1.21 (C-H region (a) and the C-O-C region (b)). The decrease of the band with time reveals the degradation rate. The photocatalytic activity of the mesoporous thin films has been also tested using FTIR by following the degradation of stearic acid (2975-2845 cm^{-1} range: $–CH_3$, and $–CH_2$ stretching) as a function of UV exposure time.[101]

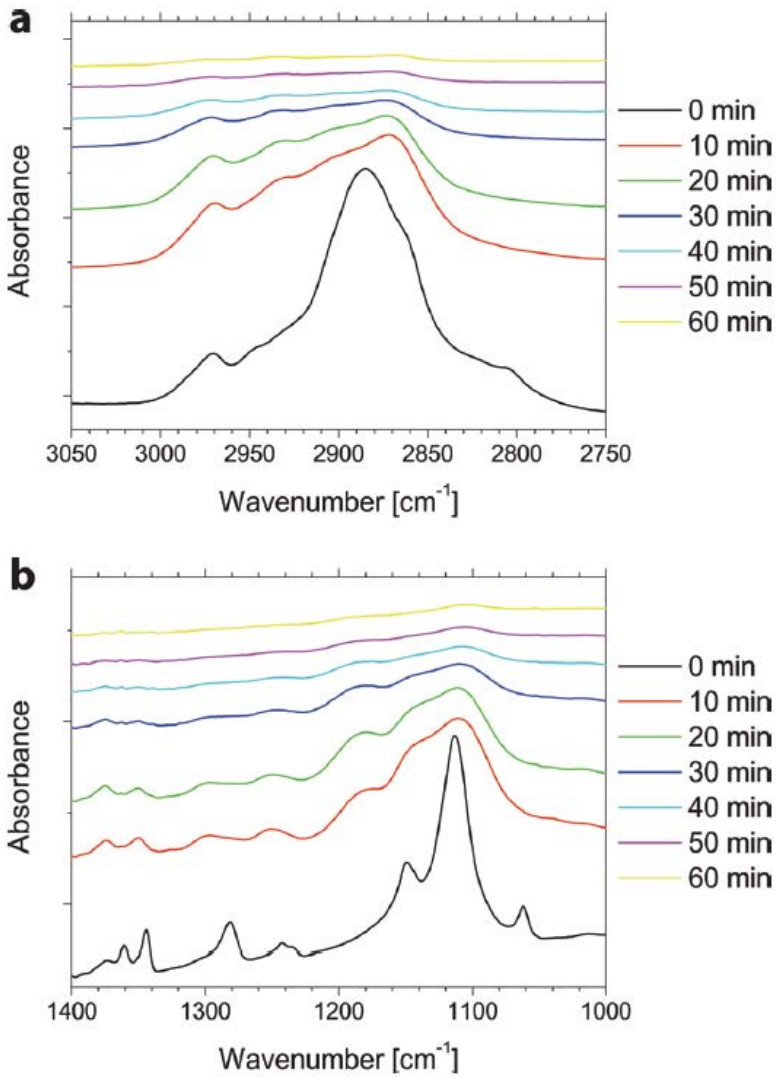

Figure 1.21 *FTIR spectra of Pluronic F127 deposited on TiO_2 films and UV irradiated at 100°C for different times. The (a) C-H and (b) C-O-C regions are shown.*[100]

1.3.3 Ellipsometry

Ellipsometry is main characterization technique used during this thesis. It has been used as tool to characterize the materials structure and porosity by Environmetal Ellipsometric Porosimetry and the films optical properties. In addition it has been adapted to characterize the photocatalytic properties of the systems in controlled environment and as function of the material structure and composition. In the following section, the general principles of the

ellipsometry technique will be discussed together with its utilisation for porosity and photocatalytis evaluation.

1.3.3.1 Generality on Ellipsometry Porosimetry

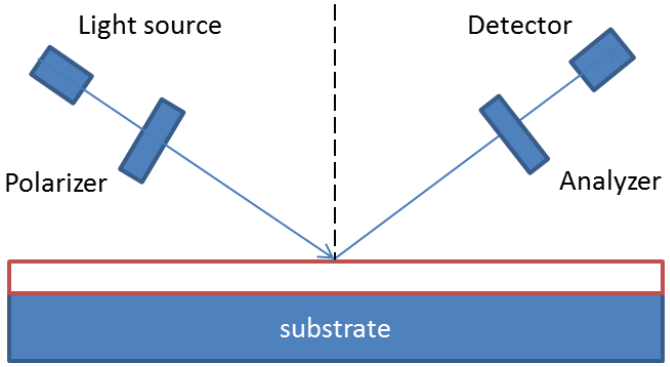

Figure 1.22 *Ellipsometry scheme for measurements of thin films.*

Spectroscopic ellipsometry has first been used for investigating film properties in 1948 by A.B. Winterbottom.[102] Graphical solutions of the precise equations which show the functional relationship between film properties and ellipsometer measurements was presented in 1962.[103] An ellipsometer enables to measure the refractive index and the thickness of semi-transparent thin films. It is a technique that measures the variation of the polarization of light before and after reflection on a surface. From these changes, the optical constants of the surface and the reflection coefficients of the system could be calculated. Figure 1.22 shows the scheme of the measurement. In order to study a film by ellipsometry, the optical properties of the bare substrate must be first measured, the thickness and the reflective index could be computed from the reflection coefficient. The film would be deposited on the substrate then and the reflection coefficient of the combination would be measured. Both the index of refraction and thickness of the film could be calculated from the complex reflection coefficient of the film-substrate combination. Based on spectroscopic ellipsometry measurements, Ellipsometry Porosimetry (EP) was then reported by Baklanov and co-workers as a very powerful technique for pores characterization of supported porous films.[104,105]

In order to carry on the ellipsometry porosimetry measurement, the sample has to be placed in a chamber with controlled relative pressure as in figure 1.23. This analysis consists in plotting an adsorption-desorption isotherm extracted from the changes in refractive index and of the

film thickness upon adsorption of a specific adsorbate (usually water). This variations are used to calculate the quantity of adsorbate present in the film. Pore size distribution of micro- and mesopores of the film can be directly obtained by porosimetry models usually based on the Kelvin equation for the determination of mesopores sizes[104] or different models such as the Dubinin Raduchkevich (DR) model for the determination of micropores sizes.[106]

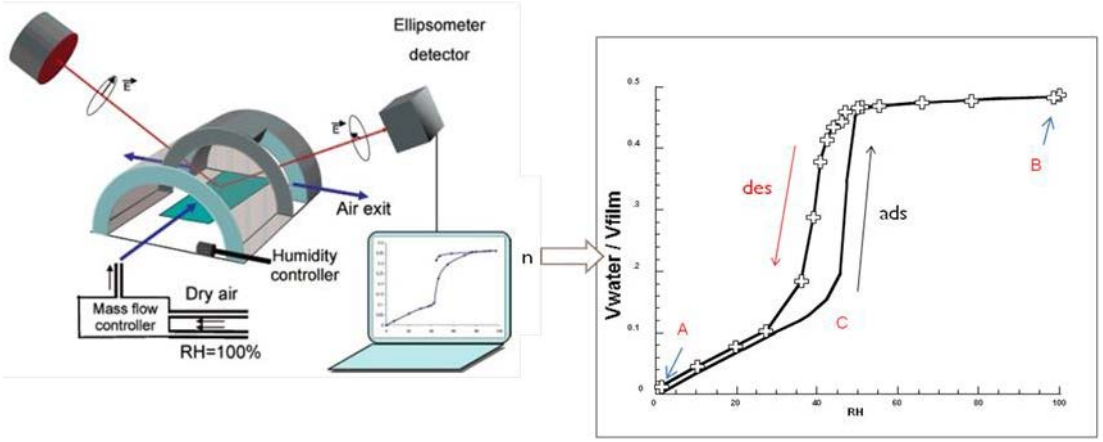

Figure 1.23 *Scheme of experimental ellipsoporometer.*[107]

The porous films parameters: porosity, pore anisotropy, pore size distribution and surface area can be calculated by Ellipsometry porosimetry measurements. Effective medium theories provide approximate expressions for the effective refractive index of a porous medium. If the bulk of the material A has dielectric constant ε_A, the pores are filled with a material B of dielectric constant ε_B and the measured material with a dielectric constant ε, the lorenz-lorenz relation yields the effective refractive index as a solution of

$$F(\varepsilon) = f_B F(\varepsilon_B) + f_A F(\varepsilon_A) \quad (16)$$

$$f_A + f_B = 1 \quad (17)$$

where $F(\varepsilon) = (\varepsilon-1)/(\varepsilon+2)$, where f_A and f_B are the fraction of the material A and material B, and $\varepsilon=n^2$. Or else we can also use Bruggemann Effective Medium Approximation (BEMA) model (the same meaning for every parameter):

$$f_A \cdot \frac{\varepsilon_A - \varepsilon}{\varepsilon_A + 2\varepsilon} + f_B \cdot \frac{\varepsilon_B - \varepsilon}{\varepsilon_B + 2\varepsilon} = 0 \quad (18)$$

Especially in our work, the use of water as adsorbate in mesopores made the usual macroscopic optical description of water unreliable. It is shown indeed that the density, surface tension and hydrogen bond network of confined water droplets and the cured water interface does differ significantly from the bulk.[108-111]

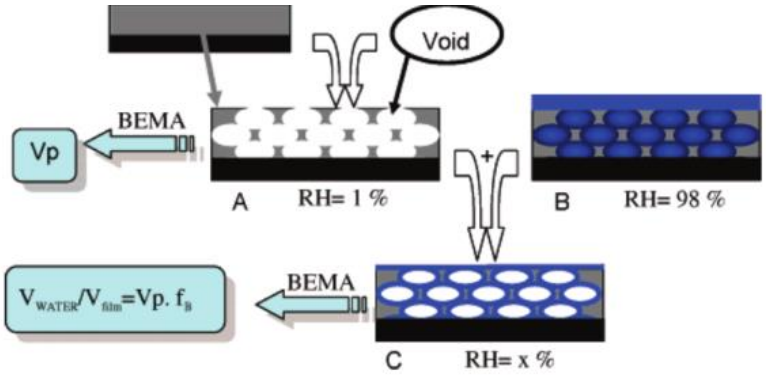

Figure 1.24 *The A film porous volume V_p is determined by fitting with BEMA the volumetric fraction of void and reference film of the dry stabilized mesoporous film. V_{water}/V_{film} adsorbed is determined by fitting with BEMA the volumetric fraction of the dry stabilized mesoporous film, A and the water saturated mesoporous film B.*[107]

The porous volume V_P of the mesoporous layer could be calculated by the BEMA or by the Lorentz-Lorenz (see Figure 1.24). In this method, film A is the mesoporous film full of air (RH=0%), and film B is the mesoporous film full of water (RH=100%). Film C is the film at different relative humidity. The fraction of water present in Film C is determined by mixing a proportion of Films A and B in the BEMA model. The isotherm is thus plotted from n=F(RH), taking f_A and f_B as the fraction of Films A and B from the BEMA or from the Lorentz-Lorenz equation. In this condition, the water density shift due to the confinement of water is included in the global optical constant of Film B. V_{WATER}/V_{FILM} was then assumed to be equal to the porosity and to the fraction of water-full film (see equation (19)). The calculation is then valid for each humidity.

$$V_{WATER}/V_{FILM} = f_B V_p \qquad (19)$$

The pore size distribution (PSD) was determined from the ellipsometry porosimetry isotherm via a modified kelvin equation (20) taking into account the pore anisotropy and the water

layer thickness *t* which is measured by ellipsometry on a flat surface at each RH. The water layer thickness absorbed of mesopores surface was assumed to be equivalent as the water thickness t absorbed onto a flat surface of a reference film.

$$RTln\frac{P}{P_0} = \gamma V_L cos\theta \frac{dS}{dV} \quad (20)$$

The Kelvin equation (20) gives the relation between the relative pressure P/P_0 of an absorbate and the capillary radius describe as $cos\theta \frac{dS}{dV}$. dS is the adsorbate liquid-air interface surface area variation, while the volume V of absorbate varies of dV. [108,112] θ is the solid/liquid wetting angle, $V_L$is the molar volume of the adsorbate after capillary condensation, and γ is the liquid-air surface tension of the curved interface. The relative pressure P/P_0 could be assumed to be equal to the RH because the metal oxide surface adsorbs preferentially water than air molecules.

For ellipsoidal pore shapes (as in most of the mesoporous films), the dS/dV factor of equation (20) could be modified as the ellipsoidal sphere volume V and surface expressions S are given as function of b and p as follow:

$$V = \frac{4}{3}\pi p^2 b^3 \quad (21)$$

$$S = 2p^2 b^2 \pi + (\pi b^2/E) ln\left[\frac{1+E}{1-E}\right] \quad (22)$$

With $$E = \frac{(p^2-1)^{1/2}}{p},$$

Where p equal to the ratio of the ellipse large radius a on small radius b. We obtain the Kelvin equation for ellipsoidal interfaces:

$$RTln\frac{P}{P_0} = -\gamma V_L cos\theta[1 + \frac{C}{2p^2}]/b \quad (23)$$

With $$C = \frac{\ln[\frac{1+E}{1-E}]}{E}$$

$1+C/2p^2=G$ is the geometric coefficient. It showed a significant influence by ellipsoid anisotropy p, especially when p value between 1 and 3, which means that the kelvin radius determination was very sensitive to the anisotropy. This factor is dependeng on the contraction of the mesostructure that could be described as a multiply of the wall contraction

and the pore contraction (anisotropy p). The mesostructured pore lattice contractions of mesoporous films can be quantified with a good accuracy by a simple ellipsometric monitoring of films thicknesses or/and by GI-SAXS pattern analysis.[109] The wall contraction is assumed to be equal to the uniaxial contraction of the reference film at the power 1/3. So the anisotropy induced by calcination could be expressed by equation (24)

$$p = \frac{d_{\mathrm{FILM\ 25}}}{d_{\mathrm{FILM\ T}}}\left(\frac{d_{\mathrm{REF\ T}}}{d_{\mathrm{REF\ 25}}}\right)^{1/3} \quad (24)$$

In which d_{FILM} and d_{REF} are the thickness of the mesoporous film and dense reference films which are obtained by ellipsometry at temperature T.

In the same way, the Kelvin equation can be modified to describe ordered mesopores with 2D cylindrical pores (usually organized parallelly to the substrate). The contraction normally happens to the c axis. The following equation (25) was obtained, in which b represents the small radius of the ellipsoidal section of a flatten cylinder:

$$RTln\frac{P}{P_0} = -\gamma V_L cos\theta\left[\frac{1}{2}\left(1+\frac{1}{p}\right)\right]/b \quad (25)$$

1.3.3.2 Ellipsometry measurement for photocatalytic activity

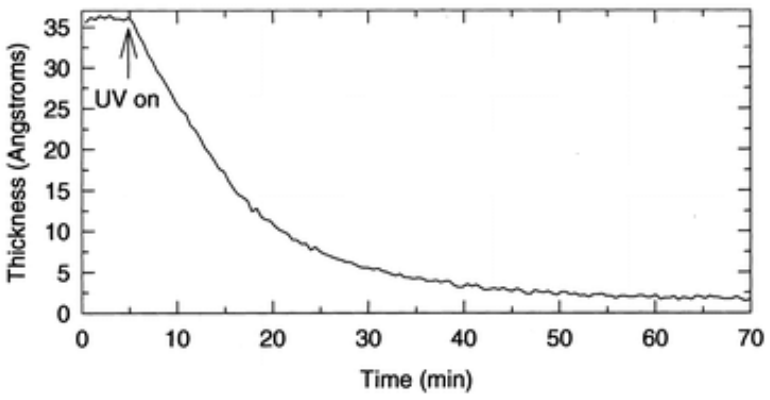

Figure 1.25 *Evolution of thickness decrease of a stearic acid layer deposited on top of a dense TiO_2 film and under UV irradiation.* [114]

As mentioned there are several methods to measure the photocatalytic activity efficiency. As we use thin films, ellipsometry is more suitable and convenient for film measurement study.

Ellipsometer was successfully applied on photodegredation measurement combined with a UV LED lamp.[113] It takes short time (usually in seconds) and also it allows in-situ measurement with different environments. Spectroscopic ellipsometry for photocatalysis studies was first used to monitor the thickness decrease of a stearic acid layer deposited on top of a dense TiO_2 film and under UV irradiation as shown in Figure 1.25.[114]

Another approach consists in measuring the refractive index variation of a porous film infiltrated by an organic pollutant in order to get the degradation information within the film.[113-117] The method was first proposed to study the photocatalytic efficiency of Eu^{3+}-doped mesoporous TiO_2 films.[118] Fig 1.26 shows the evolution of refractive index of the film as a function of irradiation time under illumination. The refractive index of the film is the result of the addition of the polarisability of the titania walls and the molecules present within the pores, lauric acid in this case.

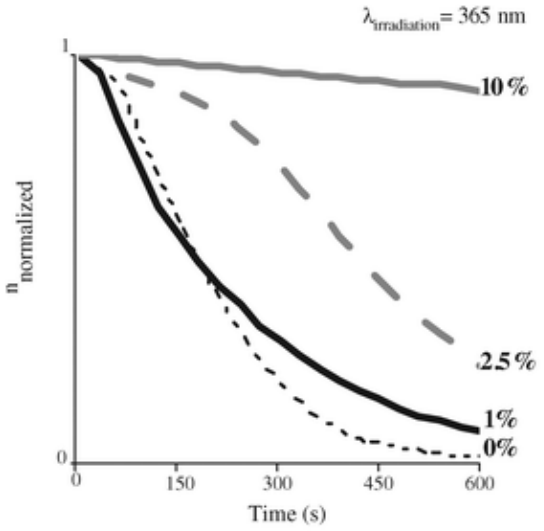

Fig 1.26 *Photocatalytic activity of Eu^{3+} doped (1–10%) and undoped mesoporous thin films deduced from the kinetics of lauric acid degradation under UV irradiation: Normalized evolution of refractive index with time.*[118]

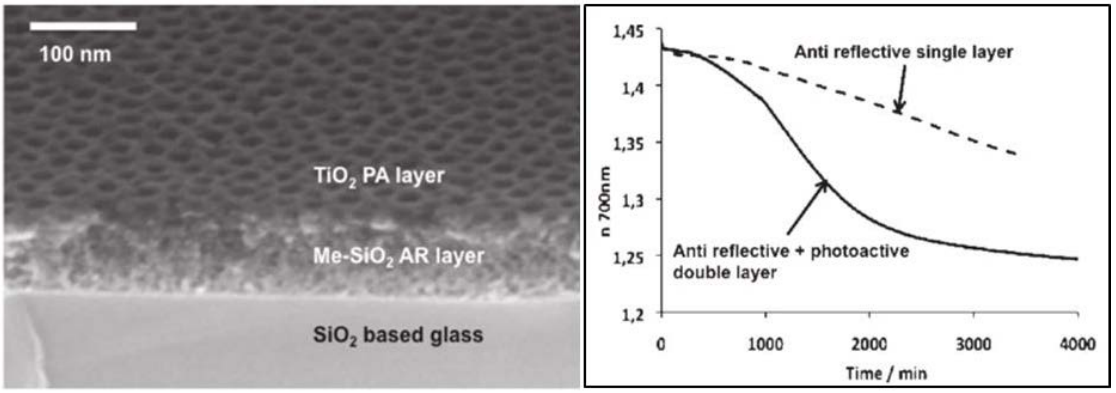

Figure 1.27 *Left: SEM image of a bilayer system composed of the thick AR underneath layer covered by the nanoperforated ultrathin PA layer (scale bar = 100 nm); Right: Evolution of refractive index with UV irradiation time for both single AR layer and AR+PA sample systems contaminated with Lauric acid.*[87]

The concept was further exploited to investigate multilayers systems such as in the case of anti-reflective, self-cleaning coatings. The bilayer was composed by an anti-reflective porous methyl-functionalized silica coating and a nanoperforated TiO_2 photoactive top-coating as shown in Figure 1.27. Ellipsometry was used to monitor the refractive index evolution of two layers of a bilayer stack infiltrated with lauric acid.[87] The ellipsometric investigation showed that adding a top photoactive layer allows progressive total decomposition of the infiltrated pollutants even in the inert underneath silica layer. This result suggested the idea that the decomposition not only happened in the interface but also happened inside the pores of the bilayer.

Another investigation of the radicals/pollutant migration was carried on.[86] The ellipsometric setup for photocatalytic activity investigation is shown in Figure 1.28. In this case, stacked layers composed of TiO_2, mesoporous SiO_2, and mixed mesoporous SiO_2/TiO_2 nanocomposites with controlled thickness and porosity were used as model materials. Lauric acid molecules and poly(vinyl chloride)(PVC) layers were used as model mobile and immobile pollutants, respectively. The local photocatalytic activity was deduced by monitoring the variation of both thickness and refractive index of each independent layer by ellipsometer. It was showed that if the pollutant is "mobile" (lauric acid), it can be photocatalytically decomposed, after diffusion of the pollutant at the vicinity of the TiO_2 nanoparticles.[86] In the case of "immobile" pollutant (PVC), the mesoporous silica layer was

proved to be a good barrier for photo-generated radicals for a distance > 10 nm.

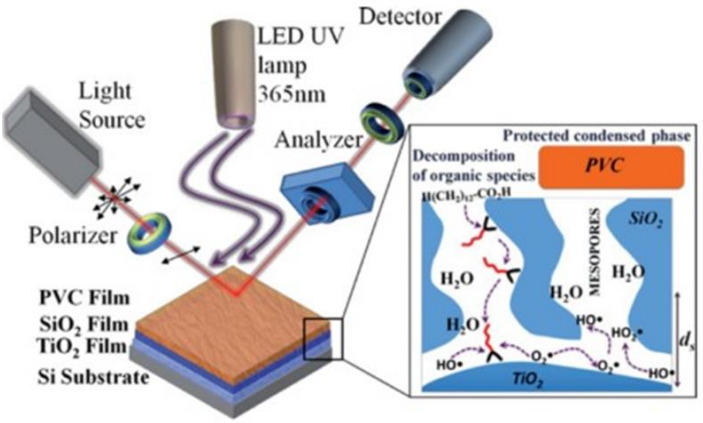

Figure 1.28 *Experimental scheme of the ellipsometric setup designed to monitor in real-time n and h of each individual layer of a stacked TiO_2/mesoporous SiO_2/PVC system during irradiation with a UV LED source.*[86]

As a conclusion for this part, compared to other techniques, ellipsometry has the advantage of being more appropriated to films. Since our films of interest are to be used in air conditions, in the following chapters we will use ellispometry to study the influence of the environmental conditions (temperature, humidity, O_2 content) on the efficiency of photocatalysis. Then the TiO_2 porous films will be modified by addition of SiO_2 in the matrix with the aim of determining the possibility to tune the optical properties and build-up transparent photocatalytic coating into a single layer. In this case, ellispometry will be used to determine the structure and the photocatalytic efficiency of the coatings.

References

1. Hagfeldt A, Graetzel M. Light-induced redox reactions in nanocrystalline systems[J]. Chemical Reviews, 1995, 95(1): 49-68.
2. Linsebigler A L, Lu G, Yates Jr J T. Photocatalysis on TiO_2 surfaces: principles, mechanisms, and selected results[J]. Chemical reviews, 1995, 95(3): 735-758.
3. Kavan L, Grätzel M, Gilbert S E, et al. Electrochemical and photoelectrochemical investigation of single-crystal anatase[J]. Journal of the American Chemical Society, 1996, 118(28): 6716-6723.
4. Diebold U. The surface science of titanium dioxide[J]. Surface science reports, 2003, 48(5): 53-229.
5. Fujishima A. Electrochemical photolysis of water at a semiconductor electrode[J]. nature, 1972, 238: 37-38.
6. Fox M A, Dulay M T. Heterogeneous photocatalysis[J]. Chemical reviews, 1993, 93(1): 341-357.
7. Fresno F, Portela R, Suárez S, et al. Photocatalytic materials: recent achievements and near future trends[J]. Journal of Materials Chemistry A, 2014, 2(9): 2863-2884.
8. Sakthivel S, Kisch H. Daylight photocatalysis by carbon-modified titanium dioxide[J]. Angewandte Chemie International Edition, 2003, 42(40): 4908-4911.
9. Asahi R, Morikawa T, Ohwaki T, et al. Visible-light photocatalysis in nitrogen-doped titanium oxides[J]. science, 2001, 293(5528): 269-271.
10. Jimmy C. Synthesis of hierarchical nanoporous F-doped TiO_2 spheres with visible light photocatalytic activity[J]. Chemical Communications, 2006 (10): 1115-1117.
11. Ohno T, Mitsui T, Matsumura M. Photocatalytic Activity of S-doped TiO_2 Photocatalyst under Visible Light[J]. Chemistry Letters, 2003, 32(4): 364-365.
12. Kubacka A, Fernández-García M, Colón G. Advanced nanoarchitectures for solar photocatalytic applications[J]. Chemical Reviews, 2011, 112(3): 1555-1614.
13. Saison T, Gras P, Chemin N, et al. New insights into Bi_2WO_6 properties as a visible-light photocatalyst[J]. The Journal of Physical Chemistry C, 2013, 117(44): 22656-22666.
14. Saison T, Chemin N, Chaneac C, et al. New Insights Into BiVO4 Properties as Visible Light Photocatalyst[J]. The Journal of Physical Chemistry C, 2015, 119(23): 12967-12977.

15. Saison T, Chemin N, Chanéac C, et al. Bi2O3, BiVO4, and Bi2WO6: impact of surface properties on photocatalytic activity under visible light[J]. The Journal of Physical Chemistry C, 2011, 115(13): 5657-5666.
16. Kavan L, Grätzel M, Gilbert S E, et al. Electrochemical and photoelectrochemical investigation of single-crystal anatase[J]. Journal of the American Chemical Society, 1996, 118(28): 6716-6723.
17. Ollis D F, Al-Ekabi H. Photocatalytic purification and treatment of water and air: proceedings of the 1st International Conference on TiO_2 Photocatalytic Purification and Treatment of Water and Air, London, Ontario, Canada, 8-13 November, 1992[M]. Elsevier Science Ltd, 1993.
18. He D, Lin F. Preparation and photocatalytic activity of anatase TiO_2 nanocrystallites with high thermal stability[J]. Materials Letters, 2007, 61(16): 3385-3387.
19. Furube A, Asahi T, Masuhara H, et al. Charge carrier dynamics of standard TiO_2 catalysts revealed by femtosecond diffuse reflectance spectroscopy[J]. The Journal of Physical Chemistry B, 1999, 103(16): 3120-3127.
20. Banfield J F, Bischoff B L, Anderson M A. TiO_2 accessory minerals: coarsening, and transformation kinetics in pure and doped synthetic nanocrystalline materials[J]. Chemical Geology, 1993, 110(1): 211-231.
21. Kudo A, Miseki Y. Heterogeneous photocatalyst materials for water splitting[J]. Chemical Society Reviews, 2009, 38(1): 253-278.
22. Simonsen M E, Li Z, Søgaard E G. Influence of the OH groups on the photocatalytic activity and photoinduced hydrophilicity of microwave assisted sol–gel TiO_2 film[J]. Applied Surface Science, 2009, 255(18): 8054-8062.
23. Carp O, Huisman C L, Reller A. Photoinduced reactivity of titanium dioxide[J]. Progress in solid state chemistry, 2004, 32(1): 33-177.
24. Costacurta S, Maso G D, Gallo R, et al. Influence of Temperature on the Photocatalytic Activity of Sol− Gel TiO_2 Films[J]. ACS applied materials & interfaces, 2010, 2(5): 1294-1298.
25. Wang R, Hashimoto K, Fujishima A, et al. Light-induced amphiphilic surfaces[J]. Nature, 1997, 388: 431-432.
26. Fujishima A, Rao T N, Tryk D A. Titanium dioxide photocatalysis[J]. Journal of Photochemistry and Photobiology C: Photochemistry Reviews, 2000, 1(1): 1-21.
27. Wang R, Hashimoto K, Fujishima A, et al. Photogeneration of highly amphiphilic TiO_2 surfaces[J]. Advanced Materials, 1998, 10(2): 135-138.

28. Sakai N, Wang R, Fujishima A, et al. Effect of ultrasonic treatment on highly hydrophilic TiO_2 surfaces[J]. Langmuir, 1998, 14(20): 5918-5920.
29. Wang R, Sakai N, Fujishima A, et al. Studies of surface wettability conversion on TiO_2 single-crystal surfaces[J]. The Journal of Physical Chemistry B, 1999, 103(12): 2188-2194.
30. Carp O, Huisman C L, Reller A. Photoinduced reactivity of titanium dioxide[J]. Progress in solid state chemistry, 2004, 32(1): 33-177.
31. Yu J, Zhao X, Zhao Q. Photocatalytic activity of nanometer TiO_2 thin films prepared by the sol–gel method[J]. Materials Chemistry and Physics, 2001, 69(1): 25-29.
32. Yu J G, Yu H G, Cheng B, et al. The effect of calcination temperature on the surface microstructure and photocatalytic activity of TiO_2 thin films prepared by liquid phase deposition[J]. The Journal of Physical Chemistry B, 2003, 107(50): 13871-13879.
33. Yu J C, Yu J, Ho W, et al. Effects of F-doping on the photocatalytic activity and microstructures of nanocrystalline TiO_2 powders[J]. Chemistry of materials, 2002, 14(9): 3808-3816.
34. Yu J C, Ho W, Yu J, et al. Efficient visible-light-induced photocatalytic disinfection on sulfur-doped nanocrystalline titania[J]. Environmental science & technology, 2005, 39(4): 1175-1179.
35. Sanchez C, Boissiere C, Grosso D, et al. Design, synthesis, and properties of inorganic and hybrid thin films having periodically organized nanoporosity†[J]. Chemistry of materials, 2008, 20(3): 682-737.
36. Vivero-Escoto J L, Huxford-Phillips R C, Lin W. Silica-based nanoprobes for biomedical imaging and theranostic applications[J]. Chemical Society Reviews, 2012, 41(7): 2673-2685.
37. Yamauchi Y, Suzuki N, Radhakrishnan L, et al. Breakthrough and future: nanoscale controls of compositions, morphologies, and mesochannel orientations toward advanced mesoporous materials[J]. The Chemical Record, 2009, 9(6): 321-339.
38. Kimura T, Kuroda K. Ordered mesoporous silica derived from layered silicates[J]. Advanced Functional Materials, 2009, 19(4): 511-527.
39. Ariga K. Silica-supported biomimetic membranes[J]. The Chemical Record, 2004, 3(6): 297-307.
40. Sanchez C, Soler-Illia G J A A, Ribot F, et al. Designed hybrid organic-inorganic nanocomposites from functional nanobuilding blocks[J]. Chemistry of Materials, 2001, 13(10): 3061-3083.
41. Livage J, Henry M, Sanchez C. Sol-gel chemistry of transition metal oxides[J]. Progress in solid state chemistry, 1988, 18(4): 259-341.

42. Brinker C J, Hurd A J, Schunk P R, et al. Review of sol-gel thin film formation[J]. Journal of Non-Crystalline Solids, 1992, 147: 424-436.
43. Mann S, Burkett S L, Davis S A, et al. Sol-gel synthesis of organized matter[J]. Chemistry of Materials, 1997, 9(11): 2300-2310.
44. Sanchez C, Boissiere C, Grosso D, et al. Design, synthesis, and properties of inorganic and hybrid thin films having periodically organized nanoporosity†[J]. Chemistry of materials, 2008, 20(3): 682-737.
45. Burkett S L, Mann S. Spatial organization and patterning of gold nanoparticles on self-assembled biolipid tubular templates [J]. Chem. Commun., 1996 (3): 321-322.
46. Grosso D, de AA Soler‐Illia G J, Babonneau F, et al. Highly Organized Mesoporous Titania Thin Films Showing Mono‐Oriented 2D Hexagonal Channels[J]. Advanced Materials, 2001, 13(14): 1085-1090.
47. Yun H S, Miyazawa K, Zhou H S, et al. Synthesis of mesoporous thin TiO_2 films with hexagonal pore structures using triblock copolymer templates[J]. Advanced Materials, 2001, 13(18): 1377-1380.
48. Jaroniec M, Schüth F. Preface to the special issue: Templated materials[J]. Chemistry of Materials, 2008, 20(3): 599-600.
49. Kresge C T, Leonowicz M E, Roth W J, et al. Ordered mesoporous molecular sieves synthesized by a liquid-crystal template mechanism[J]. nature, 1992, 359(6397): 710-712.
50. Bagshaw S A, Prouzet E, Pinnavaia T J. Templating of mesoporous molecular sieves by nonionic polyethylene oxide surfactants[J]. Science, 1995, 269(5228): 1242-1244.
51. Yang H, Coombs N, Sokolov I, et al. Free-standing and oriented mesoporous silica films grown at the air–water interface[J]. 1996.
52. Attard G S, Glyde J C, Göltner C G. Liquid-crystalline phases as templates for the synthesis of mesoporous silica[J]. Nature, 1995, 378(6555): 366-368.
53. Schüth F. Non-siliceous mesostructured and mesoporous materials[J]. Chemistry of Materials, 2001, 13(10): 3184-3195.
54. Yu C, Tian B, Zhao D. Recent advances in the synthesis of non-siliceous mesoporous materials[J]. Current Opinion in Solid State and Materials Science, 2003, 7(3): 191-197.
55. Antonelli D M, Ying J Y. Synthesis of hexagonally packed mesoporous TiO_2 by a modified sol–gel method[J]. Angewandte Chemie International Edition in English, 1995, 34(18): 2014-2017.

56. Putnam R L, Nakagawa N, McGrath K M, et al. Titanium dioxide-surfactant mesophases and Ti-TMS1[J]. Chemistry of materials, 1997, 9(12): 2690-2693.
57. On D T. A simple route for the synthesis of mesostructured lamellar and hexagonal phosphorus-free titania (TiO_2)[J]. Langmuir, 1999, 15(25): 8561-8564.
58. Cabrera S, El Haskouri J, Guillem C, et al. Generalised syntheses of ordered mesoporous oxides: the atrane route[J]. Solid State Sciences, 2000, 2(4): 405-420.
59. Ulagappan N, Rao C N R. Mesoporous phases based on SnO_2 and TiO_2[J]. Chem. Commun., 1996 (14): 1685-1686.
60. Antonelli D M. Synthesis of phosphorus-free mesoporous titania via templating with amine surfactants[J]. Microporous and Mesoporous Materials, 1999, 30(2): 315-319.
61. Yang P, Zhao D, Margolese D I, et al. Generalized syntheses of large-pore mesoporous metal oxides with semicrystalline frameworks[J]. Nature, 1998, 396(6707): 152-155.
62. Yang P, Zhao D, Margolese D I, et al. Block copolymer templating syntheses of mesoporous metal oxides with large ordering lengths and semicrystalline framework[J]. Chemistry of Materials, 1999, 11(10): 2813-2826.
63. Soler-Illia G J A A, Angelomé P C, Fuertes M C, et al. Critical aspects in the production of periodically ordered mesoporous titania thin films[J]. Nanoscale, 2012, 4(8): 2549-2566.
64. Day V W, Eberspacher T A, Chen Y, et al. Low-nuclearity titanium oxoalkoxides: the trititanates $[Ti_3O](OPr^i)_{10}$ and $[Ti_3O](OPr^i)_9(OMe)$[J]. Inorganica chimica acta, 1995, 229(1): 391-405.
65. Blanchard J, Ribot F, Sanchez C, et al. Structural characterization of titanium-oxo-polymers synthesized in the presence of protons or complexing ligands as inhibitors[J]. Journal of non-crystalline solids, 2000, 265(1): 83-97.
66. L.D. Landau. and V. G. Levich, Dragging of a liquid by a moving plate, Acta Physicochim.USSR1942, 17, 42-54.
67. Lee H, Dellatore S M, Miller W M, et al. Mussel-inspired surface chemistry for multifunctional coatings[J]. science, 2007, 318(5849): 426-430.
68. Schunk P.R.; Hurd A.J.; Brinker, C.J. Liquid Film Coating, Chapman & Hall, London 1997, 673-708.
69. Krins N, Faustini M, Louis B, et al. Thick and crack-free nanocrystalline mesoporous TiO_2 films obtained by capillary coating from aqueous solutions[J]. Chemistry of Materials, 2010, 22(23): 6218-6220.
70. Ogawa M. A simple sol–gel route for the preparation of silica–surfactant mesostructured materials[J]. Chemical Communications, 1996 (10): 1149-1150.

71. Yang H, Coombs N, Ozin G A. Morphogenesis of shapes and surface patterns in mesoporous silica[J]. Nature, 1997, 386(6626): 692-695.
72. Brinker C J, Lu Y, Sellinger A, et al. Evaporation-induced self-assembly: nanostructures made easy[J]. Advanced materials, 1999, 11(7): 579-585.
73. Grosso D, Cagnol F, Soler‐Illia G J A A, et al. Fundamentals of mesostructuring through evaporation‐induced self‐assembly[J]. Advanced Functional Materials, 2004, 14(4): 309-322.
74. Crepaldi E L, Soler-Illia G J A A, Grosso D, et al. Controlled formation of highly organized mesoporous titania thin films: from mesostructured hybrids to mesoporous nanoanatase TiO_2 [J]. Journal of the American Chemical Society, 2003, 125(32): 9770-9786.
75. Carp O, Huisman C L, Reller A. Photoinduced reactivity of titanium dioxide[J]. Progress in solid state chemistry, 2004, 32(1): 33-177.
76. Henderson M J, Gibaud A, Bardeau J F, et al. An X-ray reflectivity study of evaporation-induced self-assembled titania-based films[J]. Journal of Materials Chemistry, 2006, 16(25): 2478-2484.
77. Krins N, Faustini M, Louis B, et al. Thick and crack-free nanocrystalline mesoporous TiO_2 films obtained by capillary coating from aqueous solutions[J]. Chemistry of Materials, 2010, 22(23): 6218-6220.
78. Grosso D, Soler-Illia G J A A, Crepaldi E L, et al. Highly porous TiO_2 anatase optical thin films with cubic mesostructure stabilized at 700°C[J]. Chemistry of Materials, 2003, 15(24): 4562-4570.
79. Bass J D, Grosso D, Boissiere C, et al. Stability of mesoporous oxide and mixed metal oxide materials under biologically relevant conditions[J]. Chemistry of materials, 2007, 19(17): 4349-4356.
80. Sakatani Y, Grosso D, Nicole L, et al. Optimised photocatalytic activity of grid-like mesoporous TiO_2 films: effect of crystallinity, pore size distribution, and pore accessibility[J]. Journal of Materials Chemistry, 2006, 16(1): 77-82.
81. Choi S Y, Mamak M, Speakman S, et al. Evolution of nanocrystallinity in periodic mesoporous anatase thin films[J]. Small, 2005, 1(2): 226-232.
82. Angelomé P C, Andrini L, Calvo M E, et al. Mesoporous anatase TiO_2 films: use of Ti K XANES for the quantification of the nanocrystalline character and substrate effects in the photocatalysis behavior[J]. The Journal of Physical Chemistry C, 2007, 111(29): 10886-10893.

83. Yan, Xiaoli, et al. "Is methylene blue an appropriate substrate for a photocatalytic activity test? A study with visible-light responsive titania." Chemical Physics Letters 429.4 (2006): 606-610.
84. (a) Guan, Huimin, et al. "Rapid probing of photocatalytic activity on titania-based self-cleaning materials using 7-hydroxycoumarin fluorescent probe." Analytica chimica acta 608.1 (2008): 73-78. (b) Ishibashi K I, Fujishima A, Watanabe T, et al. Detection of active oxidative species in TiO_2 photocatalysis using the fluorescence technique[J]. Electrochemistry Communications, 2000, 2(3): 207-210.
85. Guillard C, Pichat P, Huber G, et al. The GC-MS Analysis of Organic Intermediates from the TiO~ 2 Photocatalytic Treatment of Water Contaminated by Lindane (1, 2, 3, 4, 5, 6 - hexachlorocyclohexane)^+[J]. Journal of Advanced Oxidation Technologies, 1996, 1: 53-60.
86. Carretero-Genevrier A, Boissiere C, Nicole L, et al. Distance dependence of the photocatalytic efficiency of TiO_2 revealed by in situ ellipsometry[J]. Journal of the American Chemical Society, 2012, 134(26): 10761-10764.
87. Faustini M, Nicole L, Boissiere C, et al. Hydrophobic, antireflective, self-cleaning, and antifogging sol− gel coatings: an example of multifunctional nanostructured materials for photovoltaic cells[J]. Chemistry of Materials, 2010, 22(15): 4406-4413.
88. Manley D W, McBurney R T, Miller P, et al. Unconventional titania photocatalysis: Direct deployment of carboxylic acids in alkylations and annulations[J]. Journal of the American Chemical Society, 2012, 134(33): 13580-13583.
89. Kraeutler B, Bard A J. Heterogeneous photocatalytic synthesis of methane from acetic acid-new Kolbe reaction pathway[J]. Journal of the American Chemical Society, 1978, 100(7): 2239-2240.
90. Kraeutler B, Jaeger C D, Bard A J. Direct observation of radical intermediates in the photo-Kolbe reaction-heterogeneous photocatalytic radical formation by electron spin resonance[J]. Journal of the American Chemical Society, 1978, 100(15): 4903-4905.
91. Janzen E G, Evans C A, Nishi Y. Kinetic study of radical production in the thermal decomposition of benzoyl peroxide by electron spin resonance spin trapping (spin counting). Rate (and substituent effect on the rate) of spin trapping by competitive scavenging of benzoyloxy radicals with galvinoxyl[J]. Journal of the American Chemical Society, 1972, 94(23): 8236-8238.
92. Chateauneuf J, Lusztyk J, Ingold K U. Spectroscopic and kinetic characteristics of aroyloxyl radicals. 1. The 4-methoxybenzoyloxyl radical[J]. Journal of the American Chemical Society, 1988, 110(9): 2877-2885.

93. Chateauneuf J, Lusztyk J, Ingold K U. Spectroscopic and kinetic characteristics of aroyloxyl radicals. 2. Benzoyloxyl and ring-substituted aroyloxyl radicals[J]. Journal of the American Chemical Society, 1988, 110(9): 2886-2893.
94. Fraind A, Turncliff R, Fox T, et al. Exceptionally high decarboxylation rate of a primary aliphatic acyloxy radical determined by radical product yield analysis and quantitative 1H-CIDNP spectroscopy[J]. Journal of Physical Organic Chemistry, 2011, 24(9): 809-820.
95. Houas A, Lachheb H, Ksibi M, et al. Photocatalytic degradation pathway of methylene blue in water[J]. Applied Catalysis B: Environmental, 2001, 31(2): 145-157.
96. Ishibashi K I, Fujishima A, Watanabe T, et al. Detection of active oxidative species in TiO_2 photocatalysis using the fluorescence technique[J]. Electrochemistry Communications, 2000, 2(3): 207-210.
97. d'Hennezel O, Pichat P, Ollis D F. Benzene and toluene gas-phase photocatalytic degradation over H_2O and HCL pretreated TiO_2: by-products and mechanisms[J]. Journal of Photochemistry and Photobiology A: Chemistry, 1998, 118(3): 197-204.
98. Agüera A, Almansa E, Malato S, et al. Evaluation of photocatalytic degradation of imidacloprid in industrial water by GC-MS and LC-MS[J]. Analusis, 1998, 26(7): 245-250.
99. Theurich J, Bahnemann D W, Vogel R, et al. Photocatalytic degradation of naphthalene and anthracene: GC-MS analysis of the degradation pathway[J]. Research on chemical intermediates, 1997, 23(3): 247-274.
100. Costacurta S, Maso G D, Gallo R, et al. Influence of Temperature on the Photocatalytic Activity of Sol− Gel TiO2 Films[J]. ACS applied materials & interfaces, 2010, 2(5): 1294-1298.
101. Carboni D, Marongiu D, Rassu P, et al. Enhanced Photocatalytic Activity in Low-Temperature Processed Titania Mesoporous Films[J]. The Journal of Physical Chemistry C, 2014, 118(22): 12000-12009.
102. Winterbottom A B. Optical Determination of Thin Films on Reflecting Bases in Transparent Environments[J]. JOSA, 1948, 38(12): 1074-1082.
103. Archer R J. Determination of the Properties of Films on Silicon by the Method of Ellipsometry[J]. JOSA, 1962, 52(9): 970-977.
104. Baklanov M R, Mogilnikov K P, Polovinkin V G, et al. Determination of pore size distribution in thin films by ellipsometric porosimetry[J]. Journal of Vacuum Science & Technology B, 2000, 18(3): 1385-1391.

105.Baklanov M R, Mogilnikov K P, Polovinkin V G, et al. Determination of pore size distribution in thin films by ellipsometric porosimetry[J]. Journal of Vacuum Science & Technology B, 2000, 18(3): 1385-1391.

106.Dultsev F N. Investigation of the microporous structure of porous layers using ellipsometric adsorption porometry[J]. Thin solid films, 2004, 458(1): 137-142.

107.Boissiere C, Grosso D, Lepoutre S, et al. Porosity and mechanical properties of mesoporous thin films assessed by environmental ellipsometric porosimetry[J]. Langmuir, 2005, 21(26): 12362-12371.

108.Gregg, S. J.; Sing, K. S. W. Adsorption, surface area and Porosity; Academic Press, London, 1982, P52.

109.Boissiere C, Brubach J B, Mermet A, et al. Water confined in lamellar structures of aot surfactants: an infrared investigation[J]. The Journal of Physical Chemistry B, 2002, 106(5): 1032-1035.

110.Smirnov P, Yamaguchi T, Kittaka S, et al. X-ray diffraction study of water confined in mesoporous MCM-41 materials over a temperature range of 223-298 K[J]. The Journal of Physical Chemistry B, 2000, 104(23): 5498-5504.

111.Tolman R C. The effect of droplet size on surface tension[J]. The journal of chemical physics, 1949, 17(3): 333-337.

112.Galarneau A, Desplantier D, Dutartre R, et al. Micelle-templated silicates as a test bed for methods of mesopore size evaluation[J]. Microporous and Mesoporous Materials, 1999, 27(2): 297-308.

113.Boissiere C, Grosso D, Lepoutre S, et al. Porosity and mechanical properties of mesoporous thin films assessed by environmental ellipsometric porosimetry[J]. Langmuir, 2005, 21(26): 12362-12371.

114.Remillard J T, McBride J R, Nietering K E, et al. Real time in situ spectroscopic ellipsometry studies of the photocatalytic oxidation of stearic acid on titania films[J]. The Journal of Physical Chemistry B, 2000, 104(18): 4440-4447.

115.Soler-Illia G J A A, Angelomé P C, Fuertes M C, et al. Critical aspects in the production of periodically ordered mesoporous titania thin films[J]. Nanoscale, 2012, 4(8): 2549-2566.

116.Grosso D, Cagnol F, Soler Illia G J A A, et al. Fundamentals of mesostructuring through evaporation induced self assembly[J]. Advanced Functional Materials, 2004, 14(4): 309-322.

117.Fujishima A. Electrochemical photolysis of water at a semiconductor electrode[J]. nature, 1972, 238: 37-38.

118.Leroy C M, Wang H F, Fargues A, et al. Emission-photoactivity cross-processing of mesoporous interfacial charge transfer in Eu^{3+} doped titania[J]. Physical Chemistry Chemical Physics, 2011, 13(25): 11878-11884.

CHAPTER 2

Oxygen and Humidity effect on the photocatalytic activity of porous TiO_2 films

As mentioned in the previous chapter, mesoporous titania films can find application as self-cleaning, photoactive coatings for air depollution. In this chapter, we exploit spectroscopic ellipsometry to follow *in situ* the photodegradation of organic species at TiO_2 interfaces during UV irradiation in air in real-operating conditions. In real systems for instance, outdoor humidity varies constantly and porosity can be alternatively full of liquid water or empty and more or less accessible to volatile organic compounds. Mesoporous crystalline TiO_2 thin films were used as photoactive catalysers, while lauric acid (or methylene bleu) was used as model pollutant. After infiltration of lauric acid in the TiO_2 film, the local photocatalytic activity was deduced by monitoring the variation of refractive index, which is directly related to the total organic content (TOC) elimination, during irradiation at 364 nm within different atmosphere compositions in O_2 and H_2O vapour. We also investigate here the influence of the organic probe by using methylene blue as pollutant and discussing its efficacy to monitor photocatalysis.

2.1 Introduction

As has been discussed in previous chapter, it is well-demonstrated that mesoporous TiO_2 film is an ideal material for photocatalytic decomposition of organic compounds. TiO_2 has become a photocatalyst in environmental decontamination for a large variety of organics, viruses, bacteria, fungi, algae, and cancer cells, which can be totally degraded and mineralized to CO_2, H_2O, and harmless inorganic anions. Many works reported the effects of the structure, including crystallinity, porosity and surface area et al on the conversion efficiency using various modals organic pollutants (stearic, oxalic, lauric acids, methylene blue, etc.) mostly in liquid phases and in model conditions.[1,2] Similarly Costacurta et. al. demonstrated that FTIR could be used to investigate the dependence of the temperature on photocatalytic activity of TiO_2 thin films in air.[3,4]

The mechanism of electron/hole pairs transfer, involving scavenging by adsorbed oxygen and water, initiating the chain of reactions that oxidize the organic species, has been well-established.[5] As explained in previous chapter, the existence of scavengers HO• and O_2• gives more opportunity for decomposition reaction to take place as shown in Figure 2.1.

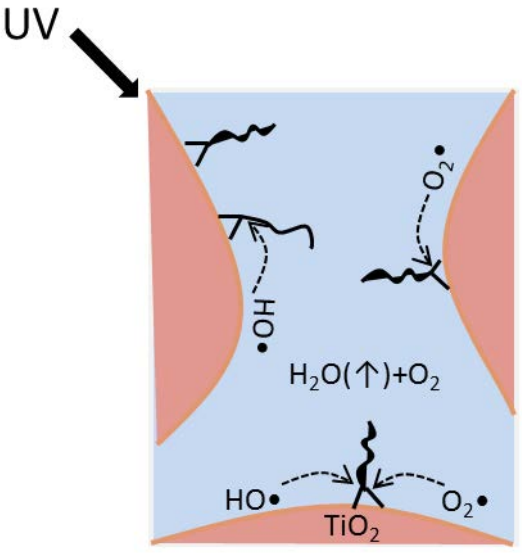

Figure 2.1 *Reaction within TiO_2 porous thin film during irradiation under a UV LED source.*

When the coatings are mesoporous, they expose a much higher surface to the environment which increases the adsorption of pollutants and facilitate a high density of red/ox intermediates. Both effects result in a higher photocatalytic activity than what is obtained

with dense films. On the other hand, because of the high hydrophilicity of titania, water is also readily adsorbed into the mesoporous network and may even exist under liquid state in the porosity at pressures inferior to saturation, a phenomenon known as capillary condensation.[6] Because outdoor humidity varies constantly, porosity is alternatively full of liquid water or empty and accessible to volatile organic compounds, and both states may present different photo-oxidation rates.

Here, we propose to address the latter point by investigating by in situ ellipsometry the photocatalytic oxidation of lauric acid model pollutant infiltrated within a typical mesoporous TiO_2 film when exposed to UV (365 nm) in various air compositions in O_2 and H_2O. Ellipsometry has proven to be an accurate method to access optical layer photocatalytic activity during UV irradiation, in real atmospheric conditions. As discussed in Chapter 1, the technique was previously used to monitor the thickness decrease of a stearic acid layer deposited on top of a dense TiO_2 film[7] or the refractive index decrease associated to the elimination of lauric acid adsorbed into the mesoporous network of complex SiO_2/TiO_2 multilayer systems.[6,8] It has the advantage of allowing the monitoring of the intrinsic loss in optical density, which is a direct indication of the TOC elimination with respect to the volume of photocatalyser in controlled environment. In our investigations, a sol-gel approach was used to prepare mesoporous TiO_2 films. Chemical and processing conditions were adjusted such that the porosity is relatively high and is composed of highly accessible nanopores of 8 nm, as typically obtained with grid-like mesostructured films, after thermal transformation into anatase. Such a structure, combining high accessibility (low tortuosity) and high surface area, has recently been shown to be favourable for the present reaction.[9]

Lauric Acid (LA) was selected because the decomposition of carboxylic acids of the same type at TiO_2 interfaces under UV radiation has been extensively studied[6] and because it's physical-chemical properties make simple its homogeneous infiltration and stabilisation within mesoporous films.[6,8] Loaded and/or unloaded films were characterised using GI-SAXS, SEM-FEG, and Ellipsometry porosimetry.

2.2 Description of the TiO_2 film

2.2.1 Preparation of the film

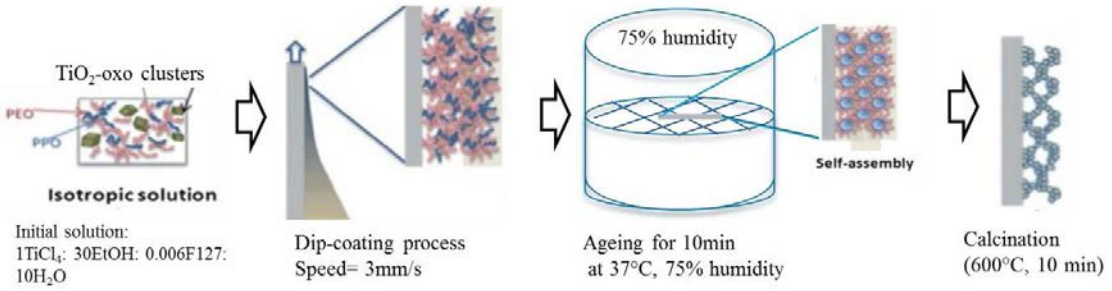

Figure 2.2 *Scheme of the steps involved in deposition of mesoporous titania thin films.*

The model mesoporous TiO_2 thin film was prepared through the sol-gel template method combined with dip-coating deposition evaporation induced self-assemble method as described in previous chapter. The detailed scheme of the steps was shown by Figure 2.2. A hydro-alcoholic solution, containing $TiCl_4$ and F127 as inorganic precursor and micellar template respectively, is deposited onto a silicon wafer by dip-coating in controlled conditions. The solution was composed of $TiCl_4$: F127: H_2O: EtOH with respective molar ratio of 1: 0.006: 10: 30, corresponding to 4.08 g Ti5E, 0.8 g F127, 1.75 g H_2O, 13.36 g EtOH for a total sol solution of 20 g. Ti5E is a mix of 1 molar ratio $TiCl_4$ into 5 molar ratio ethanol. As $TiCl_4$ is too volatile, it's necessary and more precise to dissolve it into ethanol first. Final solution was obtained by dissolving the precursor $TiCl_4$ (Ti5E) in ethanol and water followed by the addition of template F127. The silicon substrates were washed with acetone before dip-coating the solution at a constant withdrawal speed of 3 mm/s at room temperature around 22 °C and at low relative humidity (< 2%) (dry air) using a built in-house dip-coater. The as-prepared film after dip-coating, composed by a hybrid F127/Ti-oxo species, remains flexible because of the solvent content and the low inorganic condensation. An ageing step at 75% RH at 37°C for 10 minutes was immediately performed in order to promote water uptake into the material that helps the rearrangement of the F127 phase and the fast evolution of the hybrid mesophases as discussed in detail in the previous chapter and in a specific review.[10] In addition the combined effect of high humidity and moderated temperature (between 30 and 40°C) promotes HCl formation and evaporation, and leads to a faster condensation of the inorganic network. After ageing, hybrid films were calcined underneath a curing IR lamp at 600°C for 10 minutes. In this configuration, the sample after calcination results in a fully accessible mesoporous network which would be ideal for LA impregnation.

2.2.2 Structural characterization of the model mesoporous TiO_2 film

After calcination at 600°C, the mesoporous TiO_2 film was composed of anatase nanoparticles, as revealed by t

he GI-WAXS pattern in Figure 2.3. Extracting average anatase particle size cannot be done from such data because of the grazing incidence configuration.[7] Using Scherrer-derived methods would underestimate the particle size by a considerably high factor.

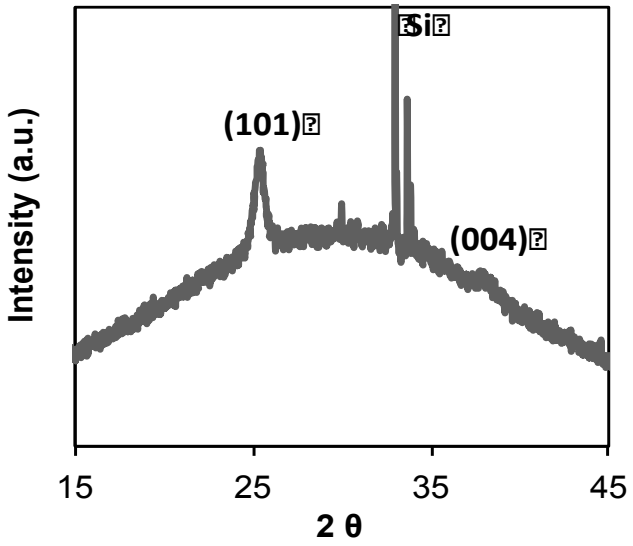

Figure 2.3 *XRD diagram obtained by radial integration of the GI-WAXS pattern.*

GI-SAXS pattern shown in Figure 2.4 reveals a single intense diffraction signal at q = 0.045 nm^{-1}, originating from domains composed of periodical planes oriented perpendicular to the substrate surface and distanced of 14 nm. As already well described in previous reports, this GI-SAXS pattern is typical of a grid-like structure obtained from the transformation of an initial (110)-oriented bcc mesostructure during thermal treatment.[11]

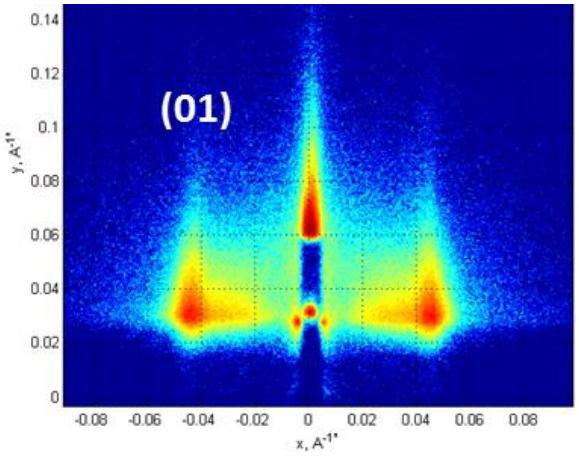

Figure 2.4 *GI-SAXS of the mesoporous titania film.*

The SEM-FEG images Figure 2.5 confirm the presence of the grid-like structure composed of sub-10 nm TiO_2 nanoparticle. The structure is less ordered that what is commonly reported with this method. This is due to the additional 38°C / 75%RH treatment that is likely to promote the discretisation of the fragile inorganic network into particles. However, and as revealed by GI-SAXS, the off-plane meso-periodicity has been retained.

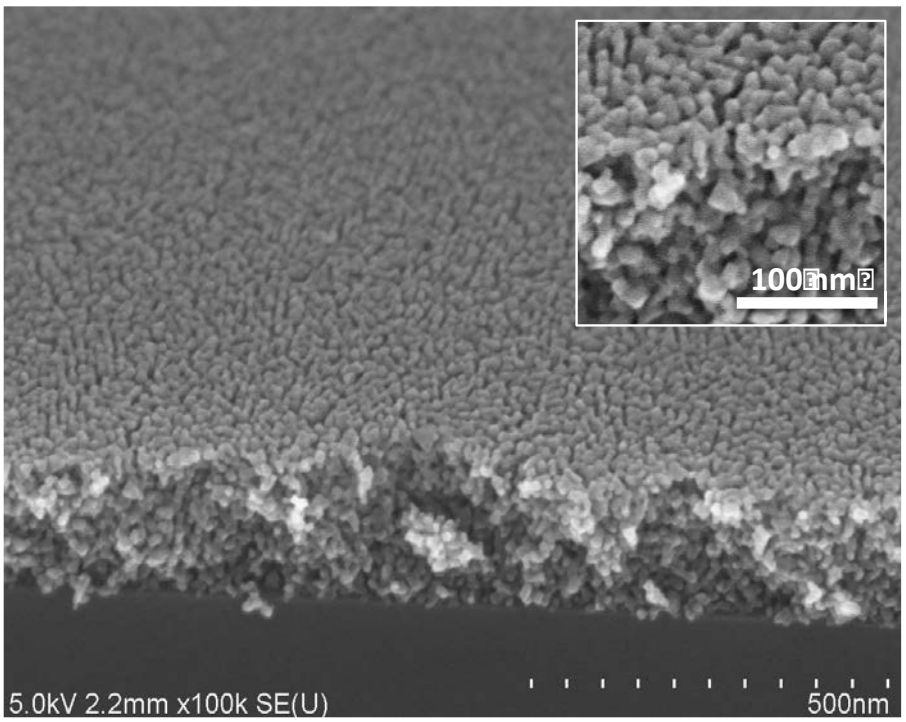

Figure 2.5 *SEM-FEG images of the mesoporous titania film, inserted the high resolution image.*

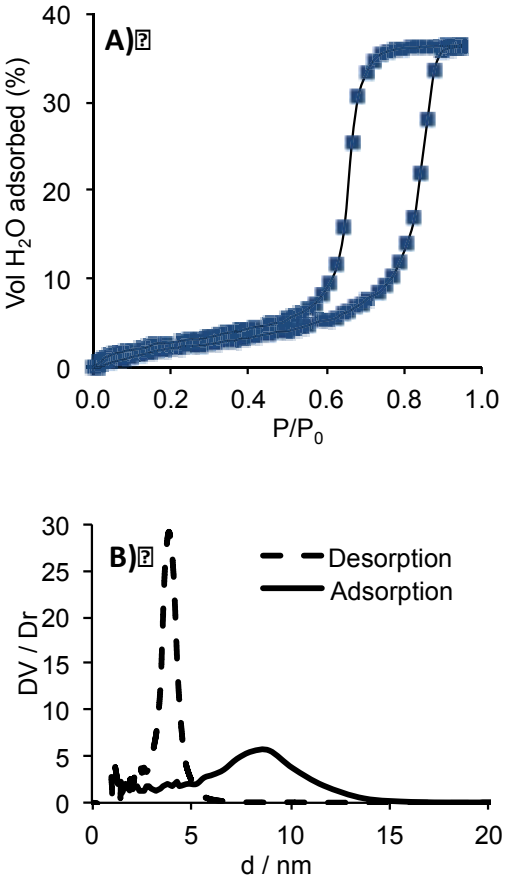

Figure 2.6 *A) Water adsoption/desorption isotherm recorded before and after impregnation with LA; B) Pore size distribution of the initial empty TiO_2 film extracted from the adsorption and desorption branches.*

The porous network morphology is further clearly evidenced by the Environmental Ellipsometry Porosimetry analysis. This technique, as described in previous chapter, consists of plotting a gas adsorption−desorption isotherm from the variations of film refractive index and thickness induced by the change of relative pressure of solvent, water in this case. The porous volume can be evaluated by using the Bruggeman effective medium approximation (BEMA) model, which was thoroughly introduced in previous chapter. It allowed the determination of the relative volumetric fractions f_A and f_B of two materials A and B of known dielectric constants ε_A and ε_B. Air and TiO_2 being not adsorbing light in the considered range of wavelengths (400-1000 nm), the dielectric constants are taken to be the square of refractive index values (real part of the dielectric constants). The determination of layer porous volume was obtained by fitting the volumetric fractions of air and titania following equation 18 of chapter 1. Pore size distribution of micro- and mesopores of the film can also be directly

obtained via porosimetry models usually based on Kelvin equation modified for the case of water. The analysis performed on the mode TiO_2 film is shown in Figure 2.6, where the type-IV isotherm shows sharp increase and decrease of the adsorbed water volume in both adsorption and desorption branches, confirming the presence of a well-defined mesoporosity with an initial pore volume of 37% according with equation 18 of chapter 1 and assuming the refractive indices of TiO_2 and air equal to 2.2 and 1 respectively. Capillary condensation and desorption occur at relative pressures of 0.88 and 0.67 respectively.

The corresponding pore size distribution deduced from the Kelvin equation for cylindrical pores are plotted in Figures 2.6 B) and give average pore and bottleneck dimension of 9±4 and 4±2 nm for both respective.

2.3 Photocatalytic investigations by in situ ellipsometry

As described in previous section, lauric acid was used as the organic probes for photocatalytic activity investigation. Lauric acid ($C_{12}H_{24}O_2$) is composed by alkyl chain and a carboxylic acid. As the carboxylic group is binding TiO_2, lauric acid could contact closely the titania surface. Photoactivity of the systems was investigated by following the refractive index of the layers, contaminated with lauric acid, upon UV irradiation and in controlled environmental conditions. In order to fit the raw ellipsometric data we used the well known Cauchy model for transparent materials:

$$n(\lambda) = A + \frac{B}{\lambda^2} + \frac{C}{\lambda^4}$$

where A and B are used fitting parameters (C contribution is negligible).The quality of the fit by using the Cauchy model was very good since in the optical range of the measurement (400 -1000 nm) the hybrid lauric acid/TiO_2 film is not absorbing.The porosity was filled-up with lauric acid by dip coating from a 0.5 wt% LA solution in ethanol. The amount of LA contaminant was controlled by varying the withdrawal speed from 5 mm/s to 15 mm/s. This is an important aspect because the amount of LA needed to be exactly adjusted in order to be able to compare the experimental results in a reliable way. The LA contamination leads to an increase of the refractive index and a modification of the pores surface chemistry. In order to be able to compare the experimental results, impregnation of the porosity with LA was

performed so that the refractive index of the initial films increases by a value of 0.1 ± 10%, typically from n = 1.7 (empty film) to n = 1.8 (polluted film) as shown in Figure 2.7 A). The adsorption desorption volume of water in the LA-polluted film is reported in Figure 2.7 B) as a comparison with the empty one. The difference in water uptake is related to the reduction of porosity associated to the partial hydrophobisation of the pores.

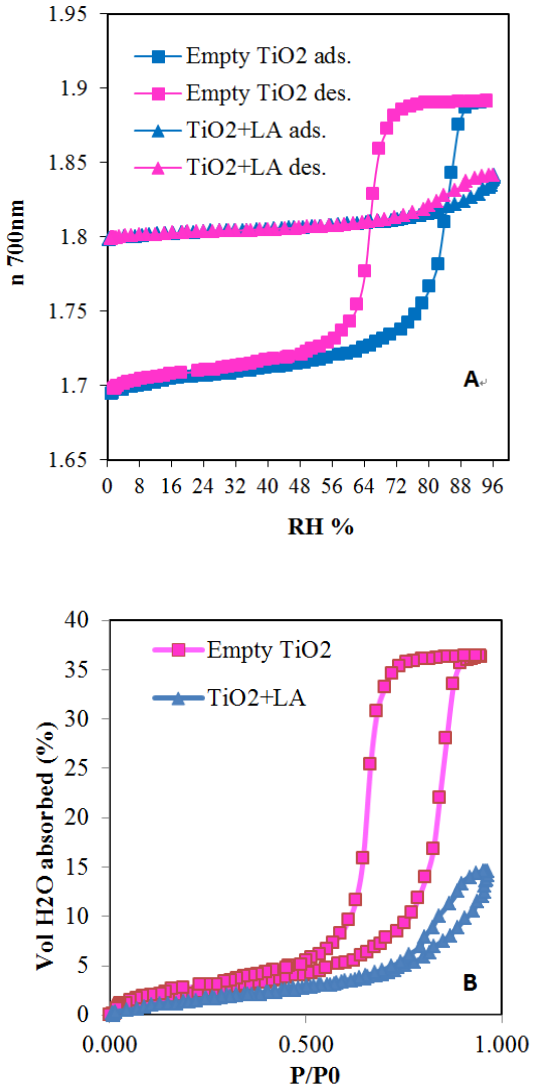

Figure 2.7 *A) EEP refractive index variations during relative humidity cycling from 0-100-0 %RH for the empty and the LA-polluted TiO_2 films. B) water adsorption/desorption isotherm recorded before and after impregnation with LA.*

The filling fraction of LA into the porosity was evaluated by a 3 components Bruggeman Effective Medium approximation as follows:

$$f_{TiO_2}\frac{\tilde{\varepsilon}_{TiO_2}-\tilde{\varepsilon}}{\tilde{\varepsilon}_{TiO_2}+2\tilde{\varepsilon}}+f_{air}\frac{\tilde{\varepsilon}_{air}-\tilde{\varepsilon}}{\tilde{\varepsilon}_{air}+2\tilde{\varepsilon}}+f_{LA}\frac{\tilde{\varepsilon}_{LA}-\tilde{\varepsilon}}{\tilde{\varepsilon}_{LA}+2\tilde{\varepsilon}}=0$$

Here again the 3 phases are not adsorbing in the considered range of the wavelength so that the dielectric constants are the square of the refractive indices. For the polluted films, $f_{air}+f_{LA}$ is equal to the 0.37 (porous volume) while f_{TiO2} is equal to 0.63. Assuming the refractive index values of the TiO_2, LA and air being 2.2, 1.42 and 1 respectively, we calculated LA filling fraction of 43±5% of the porosity (16±2% of the full film volume). In our case, the experimental ellipsometric data of our layers could be fitted with high accuracy using a single layer model, indicating that their optical properties are homogeneous, and, as a consequence, that their chemical composition (thus lauric acid impregnation) is homogeneous.

If one assumes that the porosity is made of cylindrical pores or radius *r*, filling *x*% of the porosity with LA comes to cover the pore interface with a layer of thickness $t = r(1-(1-x\%)^{0.5})$. If pores are 9 nm in diameter, the layer of LA covering the walls would be around 1.1 nm to fill up 43% of the porosity. Since the theoretical length of a molecule of LA is 1.5 nm, the present pollution consists roughly of less than a single layer of LA interacting with the TiO_2 walls through carboxylate complexing bonds.

The polluted samples were then placed into the environmental chamber 4 cm under a UV lamp (365 nm / 41.1 mw / cm^2). The optical density of the films was recorded by in-situ ellipsometry every 20s at controlled humidity.

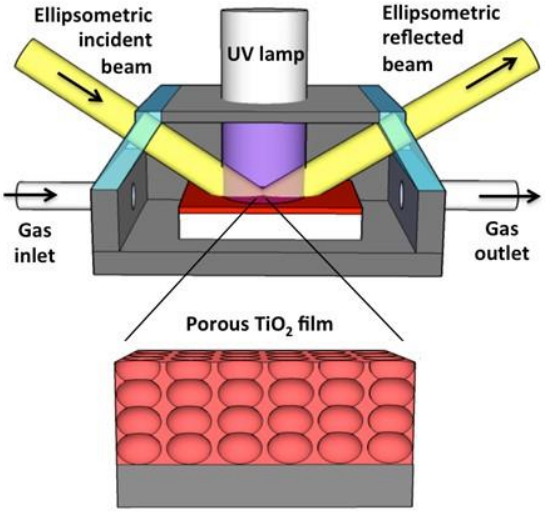

Figure 2.8 *Scheme of the set-up use to study the variation of refractive index during UV irradiation.*

Photocatalytic activities in air were deduced from the evolution of the refractive index of the film produced by the elimination of the lauric acid infiltrated into the porosity recorded with the home-build system shown in Figure 2.8. The ellipsometric set-up gives the opportunity to monitor the evolution of the optical properties of the films under irradiation and with controlled environment composition into the chamber. By introducing pure nitrogen we got the environment of 0 O_2– 0 H_2O. 20 O2 – 0 H_2O was got by introducing pure air into the reaction chamber. While 10 O_2 – 0 H_2O was got by a mix gas of half portion of air and half of nitrogen in the reaction chamber. By giving pure air and a different ratio of H_2O varying from 20% –80%, we investigated the effect of H_2O on TiO_2 photocatalytic activity.

2.3.1 Investigation of the influence of oxygen on photocatalysis

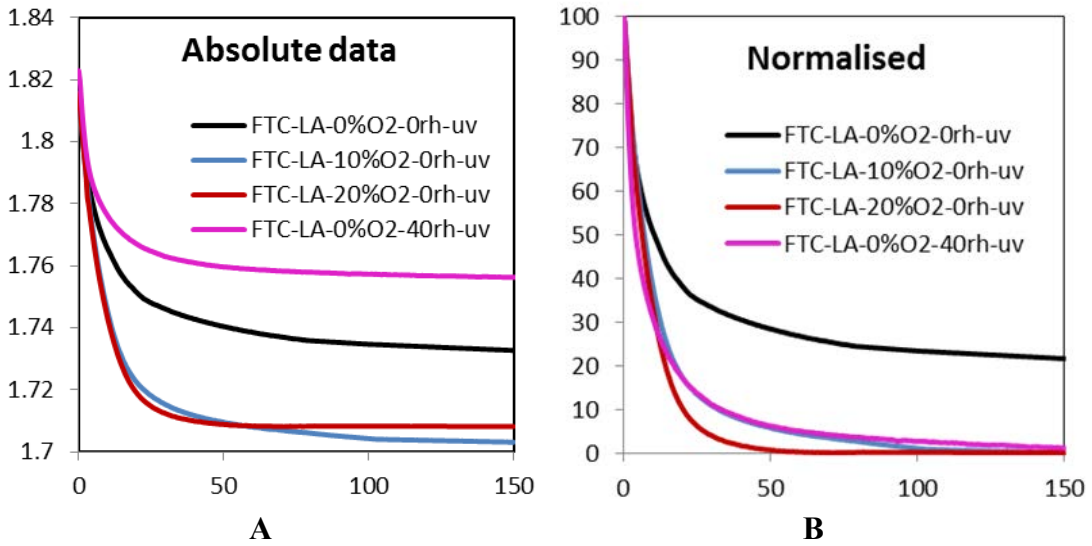

Figure 2.9 *A) The influence of Oxygen on phtocatalytic activity; B) Normalised LA/LA_0 % plotted versus time for each investigation.*

Figure 2.9 shows the influence of oxygen on photocatalytic activity. In Figure 2.9 A) we report the refractive index variation versus UV irradiation time. The normalised consumption of lauric acid LA/LA_0 % is plotted in Figure 2.9 B). The ratio LA/LA_0 was obtained by the following equation: $LA/LA_0 = (n(t)-n_0)/(n_{max}-n_0)$ where n_0 is the initial refractive index of the empty film before lauric acid impregnation, while n_{max} was the refractive index after lauric acid pollution. For the sample FTC-LA-0%O_2-0rh-uv, after 150 min irradiation, the refractive index went down very slightly and the refractive index stayed around 1.74 which was far

away from the initial refractive index. It reveals that the photocatalytic decomposition could not be completed without O_2. When O_2 is present, 10% O_2 and 20% O_2, the decomposition of the organic went fast and was complete. The reason for this is due to its role of hole scavenger when adsorbed on the surface of TiO_2 to form O_2•. Varying O_2 composition (10% or 20%), doesn't lead to a big difference in term of photocatalytic activity. A good photocatalytic efficiency is also observed in absence of oxygen but in presence of water vapor in the atmosphere (0% O_2, 40% rh).

2.3.2 Investigation of the influence of H_2O vapour on photocatalysis

Figure 2.10 shows the refractive index variation caused by lauric acid decomposition under UV irradiation under different humidity conditions. The humidity was controlled by mixing saturated water vapour and dry air fluxes (oxygen is 20% by average). Differently from the case of oxygen, here the system is more complex since also water can be absorbed into the pores causing a modification in optical properties. This is clear looking at the value of refractive index at t = 0 (when the pores are filled with lauric acid) that is not the same for each experiment. This difference depends (in part) on the sample preparation and more importantly it varies with the humidity value because, even if slightly hydrophobic, a certain amount of water is adsorbed into the pores (as shown previously in Figure 2.7 A). Similarly the final refractive index after lauric acid decomposition varies with the humidity.

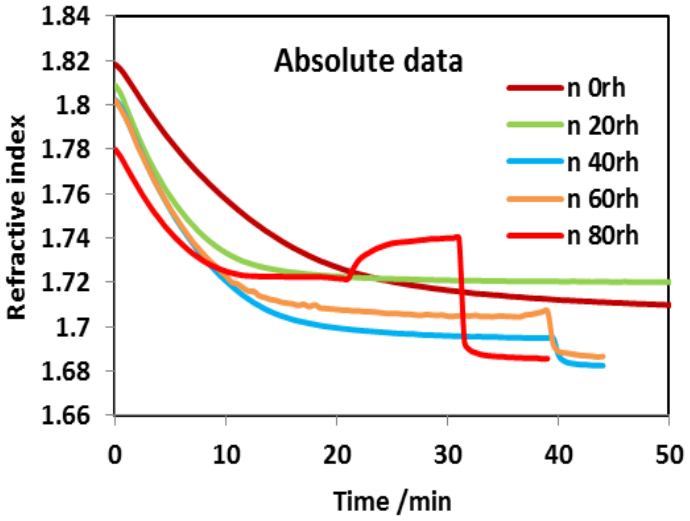

Figure 2.10 *The influence of Water vapour on photocatalytic activity.*

The evolution of the pore content during photocatalysis, was first investigated by comparing the evolution of the absolute refractive index of LA-polluted TiO_2 films upon UV-irradiation in presence of various atmospheric contents in H_2O (and oxygen for comparison) as illustrated in Figure 2.11.

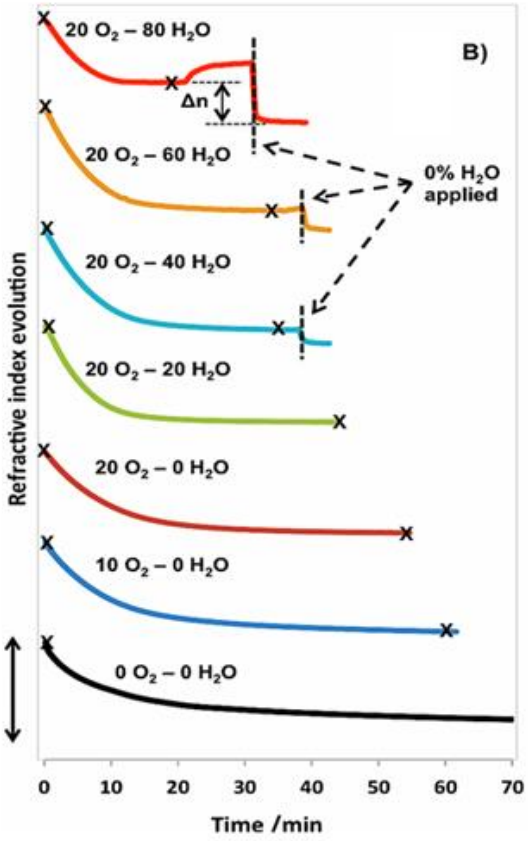

Figure 2.11 *Evolution of the absolute refractive index "n" during UV-irradiation for different compositions in oxygen and in water of the environing air. The numbers preceding O_2 and H_2O stand for total mole fraction of O_2 and relative humidity in %, respectively (ex. 20 O_2 – 40 RH corresponds to the normal fraction of O_2 / N_2 and a relative humidity of 40 %). Crosses give the initial and final stages of the experiments use for normalisation, between which LA was considered to be fully eliminated in term of TOC (the 0 O_2 – 0 H_2O sample (black line) does not have an end cross since the LA could not be fully eliminated in the experimental time frame). Experiments performed at relative humidity above 20% were completed by a RH= 0% applied after the end cross to evaluate the quantity of water present in the porosity after completion of the photocatalytic decomposition.*

In experiments performed above 20% RH, 0% RH was applied after the refractive index was found to have reached a stable value (this situation is marked by a cross on each plot). This

humidity drop is accompanied by a decrease of the refractive index that corresponds to water desorption. The refractive index differences were -0.012, -0.017, and -0.036 for experiment performed at 40, 60 and 80 % humidity, respectively. The final refractive indices correspond to the theoretical values of the empty films, confirming that the LA elimination was total at the end crosses, and that only adsorbed water remains in the pores at the end crosses depending on the conditions. The quantity of adsorbed water was greater for high humidity as expected in view of Figure 2.7 B and because of the equilibrium between vapour H_2O and adsorbed/condensed H_2O. Water is thus present for RH superior to 20% at the initial state but its content may also increase during UV irradiation due to the re-hydrophilisation associated to LA elimination.

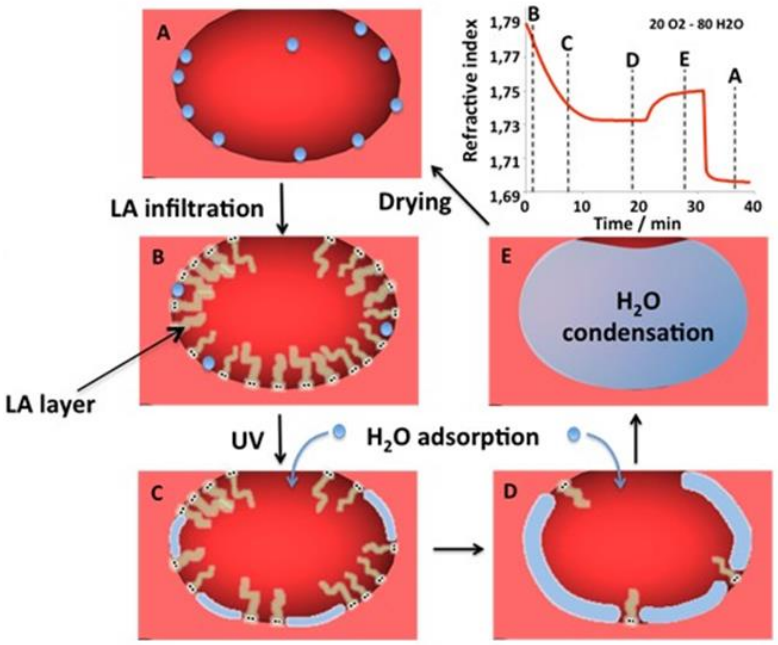

Figure 2.12 *Proposed evolution of the pore content during photocatalysis based on the refractive index evolution recorded for 20 O_2 – 80 H_2O conditions shown on the graph upper-right side (A, B, C, D and E correspond to different times).*

In order to better explain the phenomenon (especially for 80% humidity) a schematic illustration of the mechanism is proposed in Figure 2.12. After infiltration with lauric acid, the pore was almost hydrophobic at the beginning, as shown in Figure 2.12 B. UV irradiation and lauric acid decomposition is accompanied by a decrease of refractive index until stabilisation as excepted. However, looking at the specific feature recorded for *20 O_2 – 80*

H_2O, one can observe a significant n increase occurring after stabilisation (after the end cross). The refractive index increase is due to water adsorption and condensation after LA degradation. Because of the hydrophobicity of the LA hydrocarbon tail, one expects the pore to become more and more hydrophilic upon decomposition of the pollutant. It thus is not surprising to have water adsorbing after depollution as shown in Figure 2.12 C. Finally, the pore surface became completely hydrophilic as lauric acid disappearing as shown in 2.9 D causing water capillary condensation phenomenon as shown in E. Refractive index showed a significant rise at the point.

2.3.3 Discussion about photocatalytic efficiency and kinetics

In order to estimate the photocatalytic efficiency the lauric acid consumption must be evaluated for each experiment. Here the goal is to determine the lauric acid composition variation in the porosity in a system with 4 components (TiO_2, LA, water and air). For simplicity, for the following experiments involving 4 components the global refractive index was taken to be linearly dependent with the volume fraction of components (f_{TiO2}; f_{LA}; f_{H2O}; f_{AIR}), weighted by their own refractive index (n_{TiO2}=2.2; n_{LA}=1.42; n_{H2O}=1.37; n_{AIR}=1) as in equation.

$$n = f_{TiO2}n_{TIO2} + f_{LA}n_{LA} + f_{H2O}n_{H2O} + f_{TiO2AIR}n_{AIR}$$

With:

$$1 = f_{TiO2} + f_{LA} + f_{H2O} + f_{AIR}$$

And knowing that for the polluted films without water, $f_{air} + f_{LA}$ is equal to 0,37 (porous volume) while f_{TiO2} is equal to 0,63. It would have been possible to use laws, such as the Bruggeman Effective Medium approximation, to determine more accurately the fraction of each phase from the refractive index dispersions of each, but it appears that it does not significantly change the extracted tendencies exploited to compare the photocatalytic efficiency.

In Figures 2.13 A) we show the evolution of the LA consumptions for different oxygen and humidity content. One first observes that all experiments show the elimination of LA but with different efficiencies. Except for the 0 O_2 – 0 H_2O, all data were collected up to less than 2%

of the organic pollutant remains in the porosity. The oxygen and water-free atmosphere did not permit the full LA degradation in the analysis time frame, confirming their critical role. It is clearly evidenced in Figure 2.13 A) that the higher are the quantities of O_2 and H_2O in the atmosphere, the faster is the decomposition of the LA pollutant, which confirms that the concentrations of O_2 and H_2O adsorbed into the mesopores are determined by the adsorption/desorption equilibrium with the atmospheric relative pressures. Around 10 min irradiation was sufficient to decompose the full quantity of LA for 20 O_2 – 80 H_2O conditions, which correspond to a LA/TiO_2 volume fraction of 0.16/0.63 (f_{LA} / f_{TiO2}).

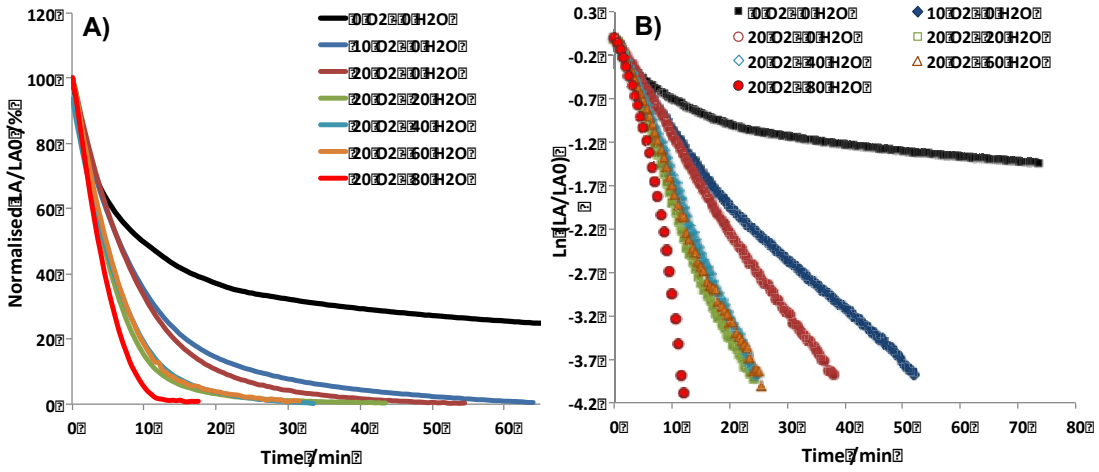

Figure 2.13 *A) Normalised LA/LA_0 plotted versus time for each investigation; B) the corresponding first-order kinetic plots ($ln(LA/LA_0)$ vs t).*

Concerning the reaction kinetics, the corresponding first-order kinetic plots ($ln(LA/LA_0)$ vs t) based on the formula $[LA]_t = [LA]_{t=0} \exp(-kt)$ are reported in Figure 2.13 B). It is often reported in conventional experiments that photocatalytic elimination of organic species in aqueous TiO_2 dispersions follows pseudo first-order kinetics.[11] In such solution dispersions, the pollutant adsorption kinetic (related to the chemical affinity and to the diffusion coefficient) must be taken into account. In our experiment, the pollutant is already in contact with the TiO_2 interface and kinetics may thus just be related to scavenging efficiency due to coexistence with LA of O_2 and OH groups at the TiO_2 surface, as fixed by the equilibrium with the atmospheric relative pressures. Indeed, if concentrations of O_2, OH groups and H_2O at the surface of TiO_2 are constant over the experiment, the rate of photodegradation should be only proportional to the concentration of LA, and more precisely to the fraction of LA

occupying the catalytic sites here, as described by the model of Langmuir-Hinshelwood. Such a situation would lead to a constant degradation rate that is only affected by the pollutant density. The plot $\ln(LA/LA_0)$ vs t in Figure 2.13 B) are not linear, suggesting that this simple situation is not the case and that the evolution of rates is not only due to the progressive consumption of LA but also due to other factors that evolve during the experiment. Figure 2.13 also shows that this evolution could be either an increase of the photocatalytic efficiency as in the case of 20 O_2 – 80 H_2O, or inversely could be a diminution of the photocatalytic efficiency as in the case 0 O_2 – 0 H_2O.

Because of the non-linearity of the first-order kinetic plots in Figure 2.13 B), no kinetic constant (k) could be extracted for the whole curves. The fluctuation of (k) upon advancement of the experiments can be visualised using the corresponding derivatives - $d(\ln(LA/LA_0))/dt$ vs *t* as plotted in Figure 2.14. It is clear that radically different tendencies denote the influences of atmospheric water and oxygen contents. Because the structure and dimension of the TiO_2 matrix is expected to remain stable, we can assume that fluctuations in k with time are mainly governed by evolution of TiO_2 surface densities in scavengers. Because atmospheric O_2 and H_2O relative pressures are fixed by the applied conditions, only the diffusion of the latters within the porosity, throughout the adsorbed LA layer, and towards the titania interface may be responsible for these fluctuations. First in absence of O_2 and H_2O in the atmosphere, the activity starts with a kinetic constant that is 0.1 min^{-1}, slightly less than in presence of water, but which rapidly drops down to 0.007 min^{-1} after 30 min. The initial activity is higher certainly due to the presence of scavengers intrinsically adsorbed during handling and impregnation with LA. Once these were consumed, the remaining low activity is due to photocatalytic activity in real water-free and anaerobic conditions. It was demonstrated that in such anaerobic conditions, an unconventional titania catalysis of carboxylic acids leads to carbon-carbon bond formation between two alkyl chains through a decarboxylation followed by radical dimerization, analogous to the photo-Kolbe reaction.[6,11]

Similar observations can be made on the two following water-free experiments, involving 10% and 20% O_2 in the atmosphere. Activities start with k around 0.1min^{-1}, but the decrease occurs after 12 min and reaches around 0.045 and 0.075 min^{-1} respectively. This situation corresponds to consumption of 70% of the organic pollutant. No Kolbe-type reaction is expected. Since the latter experiments concern only O_2, one concludes that a higher quantity of O_2 adsorbed on the TiO_2 surface for higher content in the gas phase, as expected from

exchange equilibriums, is thus responsible for the higher reactivity.

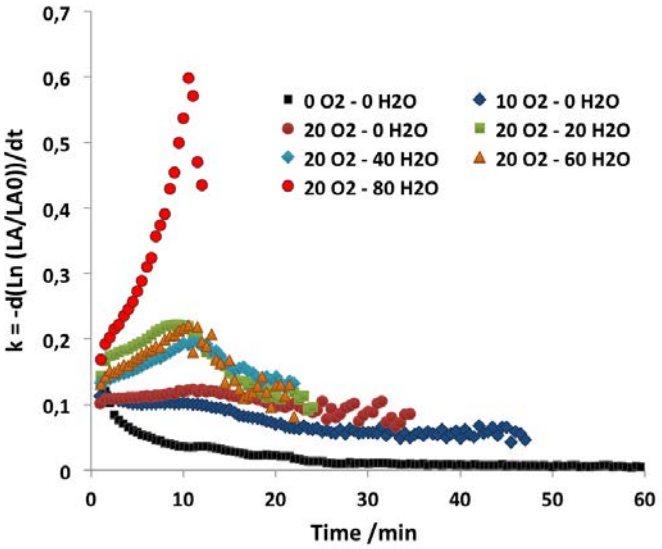

Figure 2.14 *$-D(\ln(LA/LA_0))/dt$ vs t plots, representing the evolution of the kinetic constants k (min^{-1}) along the experiment progression for each conditions.*

Concerning normal O_2 conditions (20% in the atmosphere) and applied relative humidity conditions above 20% RH, all 4 experiments showed first a global higher efficiency than without water, as expected due to the hole-scavenging role of hydroxyl groups originating from water adsorption. Second, the same tendencies, that are increase of k up to 10 min followed by a progressive decrease, are observed. Interestingly, going from 20 to 60% RH has no significant influence since all plots show the same refractive index evolution, and therefore the same activity. Only the 20 O_2 – 80 H_2O shows a significantly higher photocatalytic activity, that even progressively increases with the decomposition advancement. The final decrease of k observed above 10 min corresponds to the end of the 20 O_2 – 80 H_2O experiment, where less than 5% of LA remains in the pores. This final effect is not considered in the following global discussion. Going back to the 20-60%RH experiments, here again the concentration of H_2O adsorbed on the TiO_2 interface, and contributing to the formation of hydroxyl scavengers, must be in equilibrium with the relative humidity. However, the presence of LA at the interface must perturb this equilibrium since LA molecules occupy sites where hydroxyl radicals can potentially form. At the initial stage of the experiment, OH and O_2 scavengers are likely present due to natural adsorption during handling and impregnation. The reactions start thus with the same own "reservoir" than for the anaerobic and/or water-free conditions, this is to say with an initial kinetic constant close

to 0.1 min^{-1}. During the first minutes, LA is decomposed and liberates sites where H_2O and O_2 must adsorb. One recalls that water was present in increasing proportion in the pores at the end of the experiments from 20% to 60% RH conditions (see Figure 2.11). Consequently, the concentration in scavengers progressively increases with reaction time and the reaction becomes thus more efficient as revealed by the value of k that double up to close to 0.2/min in the first 10 min. This period is followed by a slow decrease of the efficiency down back to $k = 0.1\ min^{-1}$. This inversion of the tendency occurring at 10 min corresponds to the elimination of 80% of the LA that were likely replaced by scavengers. These observations suggest that an ideal situation exists for the present system to react that could be related to an optimal repartition of a certain ratio of scavenger/pollutant at the semi-conductor interface. Water diffusion and adsorption is not the limiting factor since the same rates were recorded between 20% and 60% RH while higher content of adsorbed water was recorded for 60% RH. Finally, it is evident that the 20 O_2 – 80 H_2O conditions provide the more efficient photoactivity, that is up to 3 times that of the second best conditions. It was mentioned earlier that these conditions were also the only ones to allow for a much higher amount of water to be adsorbed into the porosity (see Figure 2.7). The water adsorption/desorption isotherm in Figure 2.7 B) shows that 80% RH is the relative pressure at which water capillary condensation starts, suggesting that water does exist under liquid form into the nanoporosity. The much higher photocatalytic activity recorded for 80% RH can thus be linked to the presence of liquid water in the porosity. Such a liquid state must be beneficial to generate and concentrate all activated oxygen intermediate species issued from cascade oxydoreduction reaction from both scavengers. Liquid water allows also for the partial desorption (dissolution) of LA, increasing the number of adsorption sites for scavengers. Both effects promote higher LA decomposition efficiency. Finally, the final progressive increase in k value may also be explained by the progressive uptake of liquid water during the reaction, as permitted by the associated hydrophilisation of the pores, as already explained earlier. High humidity conditions are thus beneficial for heterogeneous photocatalysis in nanoporous TiO_2.

2.4 Influence of the probe: the case of Methylene Blue

As explained in Chapter 1, Methylene blue (MB) is a thiazine type dye that is widely used to probe the photocatalytic activity of several materials including mesoporous TiO_2 films in solution and in air.[12] The experiments consist in measuring the evolution of absorption with time. The dye concentration can be evaluated giving information about the photocatalytic kinetics. However the optical properties of MB are complex and very much depending on the environmental conditions.

MB exhibits interesting reversible redox properties that involve the equilibrium between the reduced (leuco) and the oxidized forms of this compound. The oxidized form of MB is blue while the reduced form is colourless. Because of that reversible equilibrium between the reduced and oxidized forms, MB is a compound useful as redox indicator. Its main uses are related with the determination of glucose, O_2 and or ascorbic acid among others. The equilibrium between the oxidized and reduced form of MB can be written as follows :

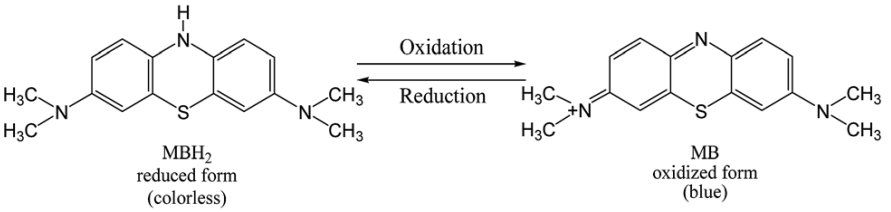

One the main uses of MB is related with the determination of glucose, O_2 and or ascorbic acid in the environment. Methylene blue is also characterized by a dimerization equilibrium that can be expressed (in acid solutions) as :

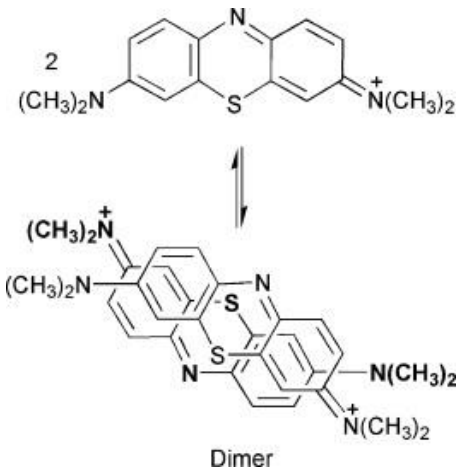

The monomer and dimer form of MB absorb light but at different wavelength. The specifics

of absorption depend on a number of factors, including protonation, adsorption to other materials, concentration and the environmental conditions.[13] For example, like many thiazine dyes, MB has a tendency to dimerize in liquid aqueous solution or when adsorbed on TiO_2 surfaces.[14]

In this part, we will use MB (instead of lauric acid) as probe for the photocatalytic experiments, as in the previous experiments, the molecules are impregnated into model mesoporous TiO_2 films and the optical behavior of MB are investigated during UV irradiation in air as function of the atmosphere composition and in particular the O_2 and humidity content. The goal here is to not (only) to determine the effect of the environmental conditions on the photocatalytic activity of porous titania (this aspect was widely discussed for lauric acid). In this part we analyze the evolution and the behavior of the MB dye and we discuss if, and/or when, MB can be "trusted" as probe in these specific experimental conditions.

2.4.1 Experimental details and optical model

In order to address the latter point we used in-situ ellipsometry with the same experimental set-up shown in Figure 2.8. Here, MB is used as model pollutant and infiltrated within the same mesoporous TiO_2 film used for the previous experiments. The infiltration was performed by dip-coating as for lauric acid. The system is then exposed to UV (365 nm) in various air compositions in O_2 and H_2O.

As seen before, ellipsometry has proven to be an accurate method to access the refractive index and thickness of layer during UV irradiation and in real atmospheric conditions. In the previous study, the real part of refractive index of the layer was directly correlated to dielectric costant ($\varepsilon = n^2$); the Lauric acid concentration could be calculated by BEMA model. This was possible since lauric acid is "transparent" (not adsorbing) over the studied wavelength range. As mentioned above MB is colored and absorbs light at wavelengths in the range 500-700 nm (depending on the configuration of the molecule). For this reason the Cauchy model alone (used for transparent materials) can't be used to describe the optical behavior of a porous film impregnated with MB. The description of the optical properties of the layer must take into account the complex refractive index written as follows: $\tilde{n}(\lambda) = n(\lambda) + ik(\lambda)$ in which n is real part of the refractive index and k is the extinction coefficient.

Alternatively we can express it, with the complex dielectric function $\varepsilon(\lambda) = \varepsilon_1(\lambda) + i\varepsilon_2(\lambda)$.

The ellipsometric fit can thus be made by using a model for absorbing materials such as the Lorentz oscillator model:

$$\tilde{\varepsilon} = \varepsilon_{1,\text{offset}} + \frac{AE_c}{E_c^2 - E^2 - iBE}$$

where $\varepsilon_1(\lambda)$ represents the real part of the dielectric function. The energy, E, is related to the frequency of a wave. The other parameters can be explained by observing a typical plot of dielectric constant of absorbing material that is shown in Figure 2.15 with a typical absorption peak. The oscillator model has 3 typical parameters: A (or Amp) that is the peak amplitude or "strength", B (or Br) that is broadening or "width" and E_c that is the center energy or "peak position".

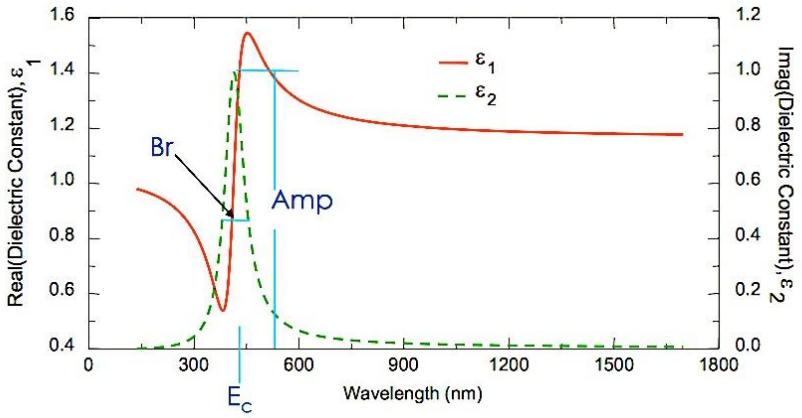

Figure 2.15 *Typical plot of dielectric constant for an absorbing material (courtesy Woolam tutorial)*

When the ellipsometric fit is correct the dielectric constant can be converted in refractive index and extinction coefficient by using the following relationships:

$$\varepsilon = \varepsilon_1 + i\varepsilon_2 = (n + ik)^2$$

$$\varepsilon_1 = n^2 - k^2 \qquad \varepsilon_2 = 2nk$$

$$n = \sqrt{\frac{[\varepsilon_1 + \sqrt{(\varepsilon_1^2 + \varepsilon_2^2)}]}{2}} \qquad k = \sqrt{\frac{[-\varepsilon_1 + \sqrt{(\varepsilon_1^2 + \varepsilon_2^2)}]}{2}}$$

This calculation is made automatically by the ellipsometric software.

According to the literature of MB, two oscillators were used in order to describe the dimer and monomer form of MB that absorb at different wavelengths. In following experiments the position of the absorption of the dimer and monomer forms are found at 530 and 600 nm (± 20 nm) respectively. Even if in the literature one can find a very wide number of different absorption wavelengths (depending on the system), our values are lower than those reported usually for liquid solution (around 600 and 650 nm). This strong shift can be due to several effects: MB in the pore is solid instead of in solution, utilization of ethanol (not in water) to dissolve MB and impregnate it into the film, confinement of MB into nanopores. This aspect will not be further discussed here; other investigations are needed to clarify this point.[13,14]

2.4.2 Effect of O_2 : photodegradation vs photoreduction

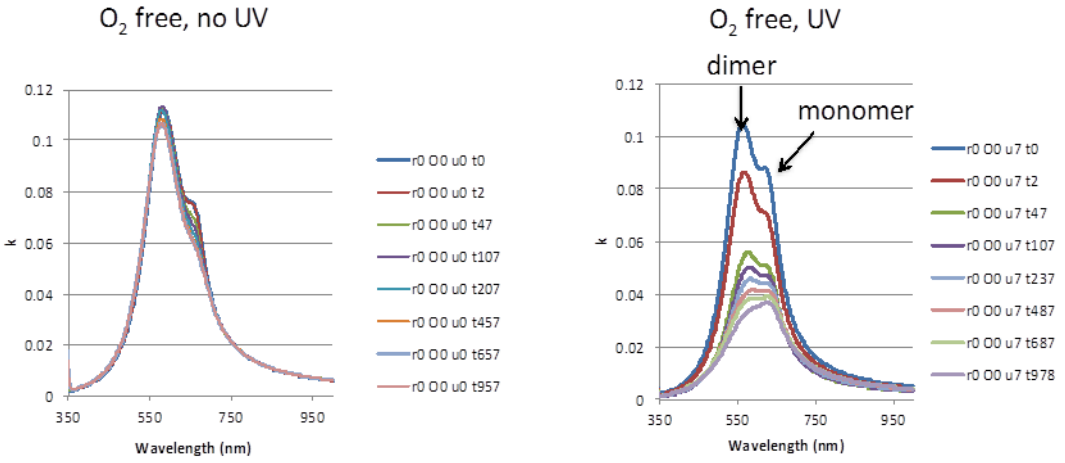

Figure 2.16 *Plots of the evolution of extinction coefficient vs wavelength for different times (the samples are named as r0 O0 u0 t x where x stand for time in minutes): (left) reference system; (right) oxygen-free and under UV irradiation.*

In the first set of experiments the MB-impregnated TiO_2 film was placed in the ellipsometric chamber under an oxygen-free atmosphere at RH% =0. This environment was obtained by fluxing nitrogen into the chamber. The optical evolution was then recorder by ellipsometry. Figure 2.16 shows the plots of the evolution of extinction coefficient vs wavelength for

different times. Two contributions can be identified in the large absorption band; they are attributed to the dimer and monomer form of MB. The dimer form absorption is majority. This is probably due to the fact that when confined in nanopores, MB molecules tend to aggregate each other as illustrated in the dimer form as illustrated above. In the first reference experiment shown in Figure 2.16 (left) no oxygen and no UV irradiation are applied. One can see that no significant decreases in absorption are occurring except that for a slight decrease for monomer peak contribution. In the second experiment, UV light is applied in anaerobic environment. Here, a decrease of the global extinction coefficient band is observed with time. This decoloration process can be due to photodegradation of MB or to photoreduction (or both).

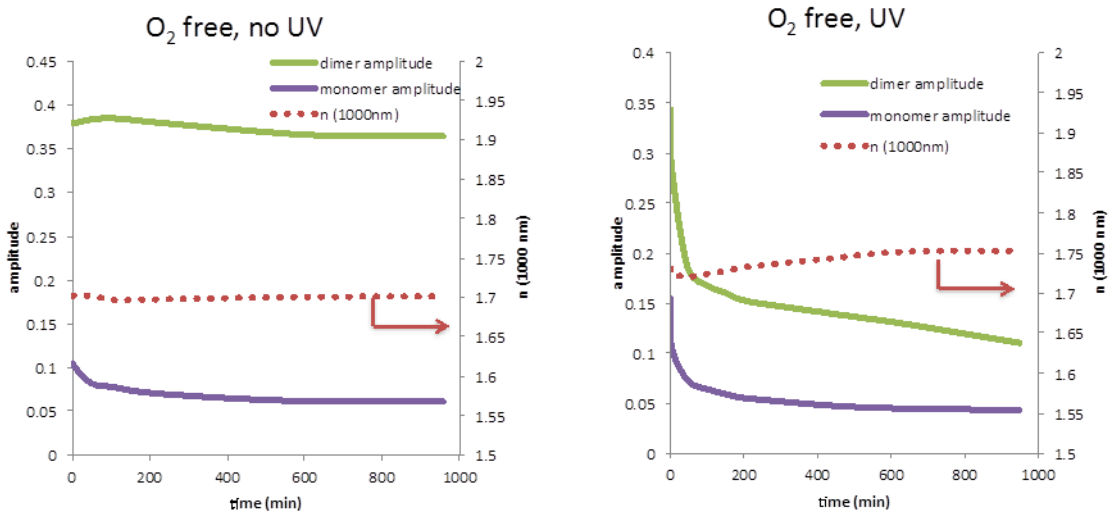

Figure 2.17 *Plots of evolution of refractive index (at 1000nm), the dimer and monomer amplitudes with time for the (left) reference system; (right) oxygen-free and under UV irradiation.*

In order to clarify the process, Figure 2.17 shows the evolution of amplitude A of the Lorentz oscillator for the dimer and monomer forms as function on the time. In the same plots we show also the evolution of the refractive index n measured at 1000 nm. This wavelength was chosen because the exception coefficient of the dye is very low meaning that material behave as transparent at λ=1000 nm. The n (1000 nm) gives an indication of effective quantity of MB present into the pore as in the case of lauric acid. In Figure 2.17 (right), the decoloration of MB is confirmed by the fact that both dimer and monomer amplitudes decreases with time.

However n (1000 nm) remains almost constant during the experiment, suggesting that no photodecomposition (towards volatile products) of MB is occurring. The decrease in absorption is thus attributed to the photoreduction of MB that leads to the colorless, reduced leuco form MB. This conclusion was supported by the fact that the molecules reversibly went back to the blue form when the sample was put in contact with oxygen.[14]

2.4.3 Effect of humidity on the photo-degradation process of MB

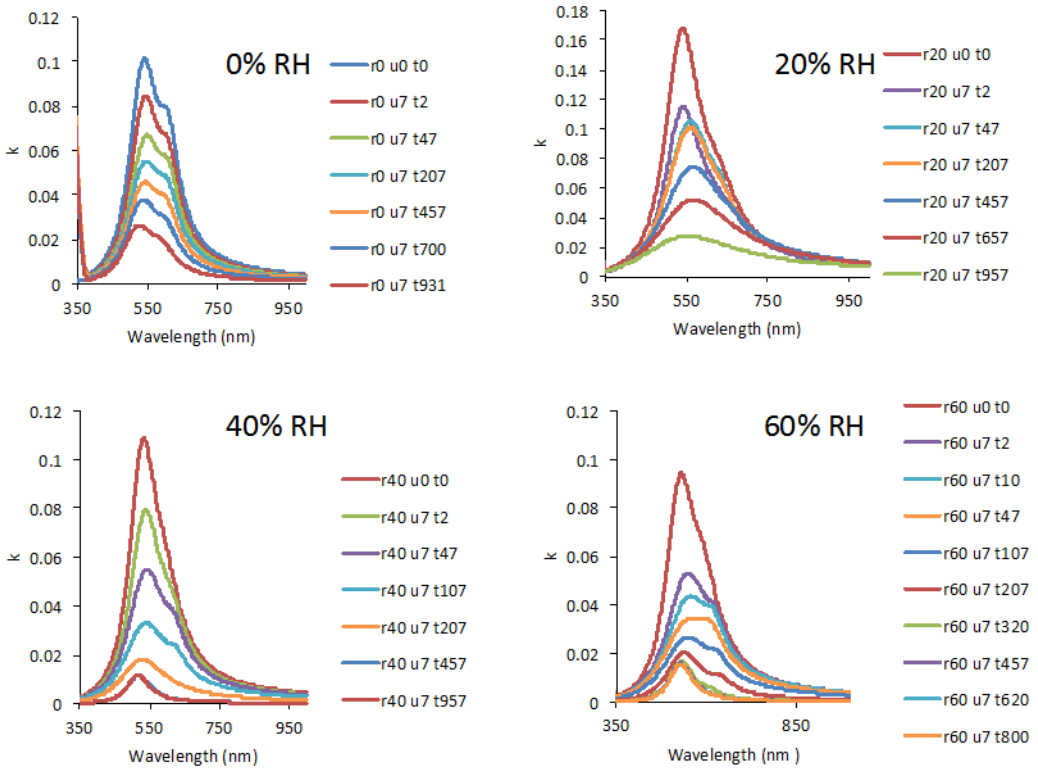

Figure 2.18 *Plots of the evolution of extinction coefficient vs wavelength for different UV irradiation times (the samples are named as rx O0 u7 ty where x stands for the humidity value and y stands for time in minutes) at 0, 20, 40, 60% RH .*

The second set of experiments was conducted under controlled humid atmosphere for RH values of 0, 20, 40 and 60%. Figure 2.18 shows the plots of the evolution of extinction coefficient vs wavelength for different times and at different relative humidity. A decrease of the global extinction coefficient band is observed with time for all RH%. Now, we can expect this decoloration process be effectively due to photodecomposition of MB since in presence of oxygen no photoreduction is expected. Plots of evolution of the total, dimer and monomer

amplitudes of the oscillators with time at different RH% are shown in Figure 2.19. Total amplitude is the sum between the dimer and monomer contribution. Here again the dimer form contribution to the absorption is majority.

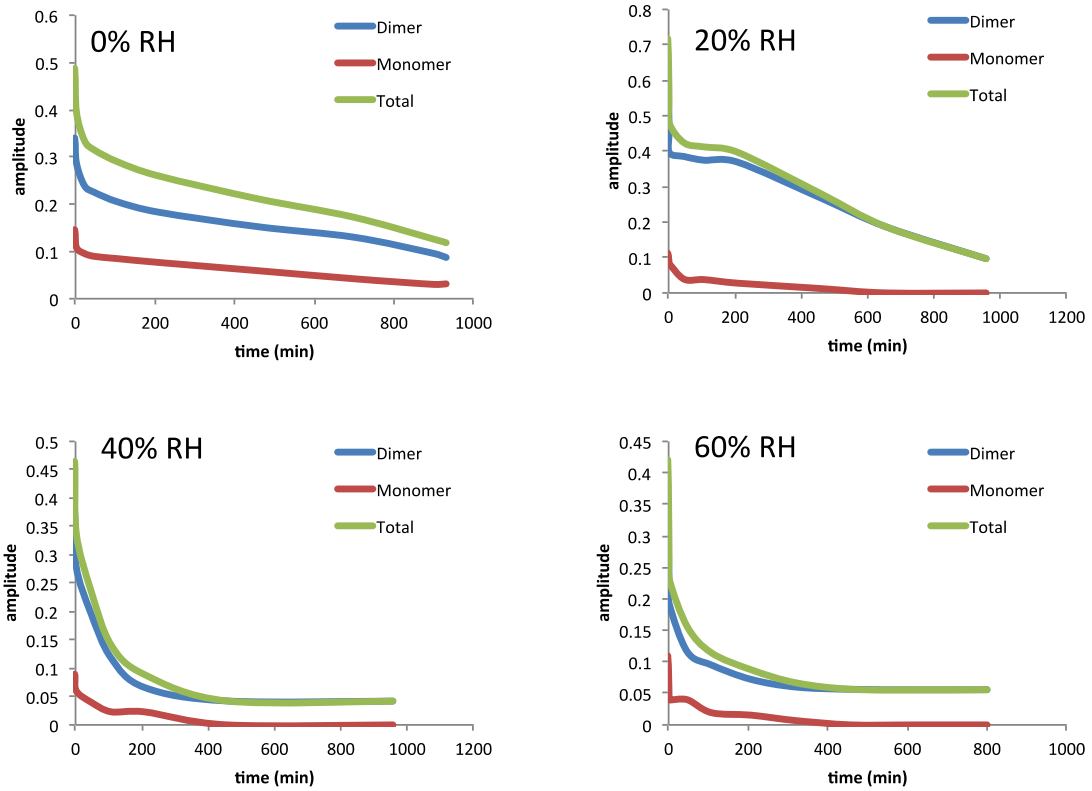

Figure 2.19 *Plots of evolution of the total, dimer and monomer amplitudes with time at different RH%.*

In order to compare the photocatalysis rate the evolution of the normalized total amplitude and refractive index at 1000 nm is plotted in Figure 2.20. For tests at 0 and 20% the process is not completed even after several hours of experiment. In all the experiments a residual amplitude is observed. The normalized total amplitude was calculated as = $(A(t)–0)/(A_0–0)\%$ where A_0 stands for initial total amplitude. The normalized N (1000nm) was calculated as = $(N(t) – N_{final}) / (N_0 - N_{final})$ where N_0 stands for the initial refractive index and N_{final} stands for refractive index of the empty TiO_2 film at the specific RH% (see EEP in Fig.2.7A).

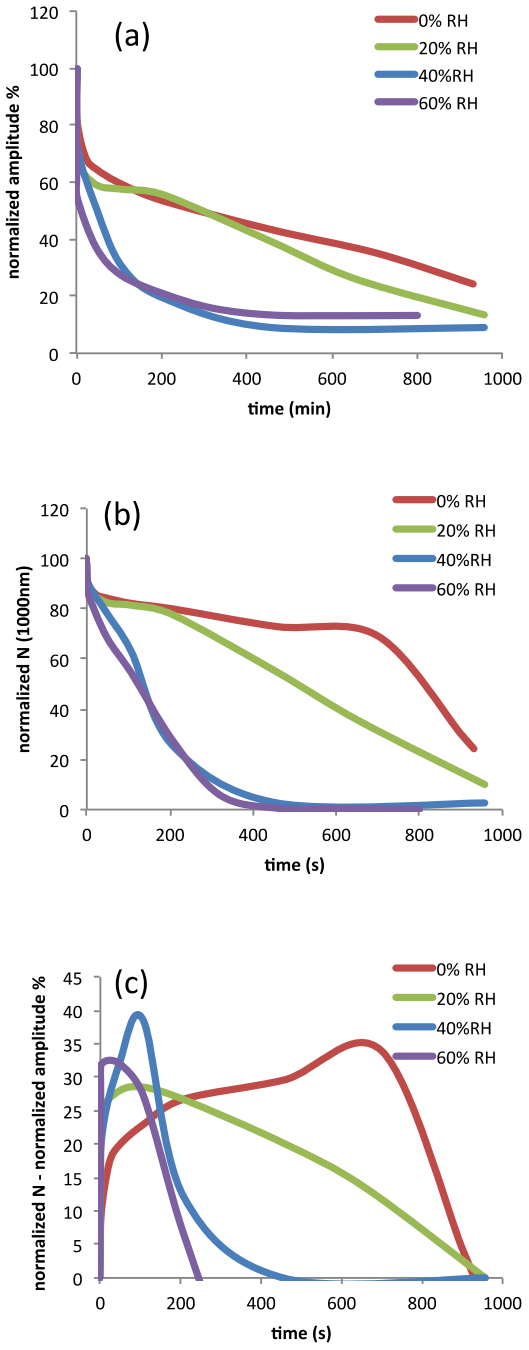

Figure 2.20 *Plots of evolution of the normalized (a) total amplitudes, (b) refractive index at 1000 nm and (c) the difference between normalized refractive index and amplitude at different RH%.*

The photodegradation proceeds with higher efficiency increasing the RH%. This global tendency is in agreement with the previous results on lauric acid. However difference in normalized amplitude and refractive index fluctuations are observed; the decrease in normalized amplitude is generally faster than the one in normalized refractive index. This

difference can be better visualized in Figure 2.20 (c) in which the difference between the normalize n (100nm) and amplitude are plotted as function of time. We can observe that this difference is always positive meaning that the degradation rate determined by n (1000 nm) is lower than the one determined by normalized amplitude. In other words, we can say that the photo-induced decoloration (expressed as a variation of extinction coefficient k) is faster than the effective loss of MB into the porosity (expressed as a variation of refractive index value).

2.4.4 Discussion on the utilization of MB as probe

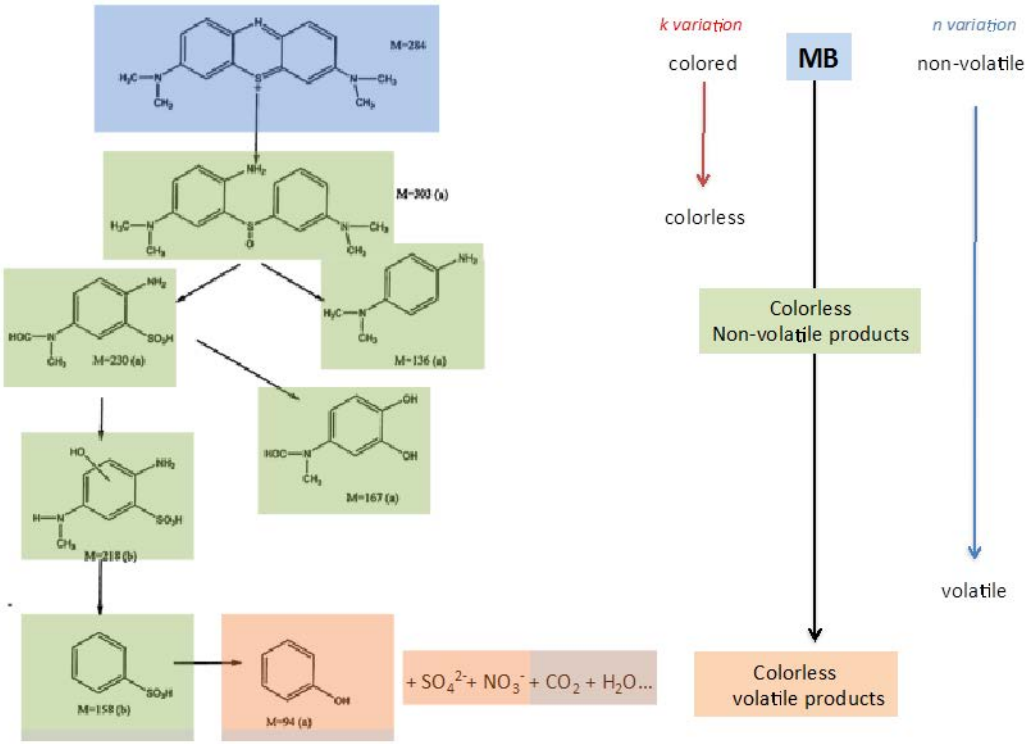

Figure 2.21 *Scheme of the photocatalytic degradation pathway of MB on TiO_2 in water forming intermediate products (adapted from reference 13)*

The difference in photodegradation rate between n and k can be explained with the different nature of the photodegradation intermediate products that are likely to be formed into the porosity. As an example we report in Figure 2.21 the photocatalytic degradation pathway of MB molecules on TiO_2 in water reported by Houas et al.[13] The photodegradation of MB doesn't lead directly and only to the complete mineralization (CO_2, H_2O, SO_3^{2-}, NO_3^-) but intermediate products are formed. If we consider the scheme proposed by Houas et al., we

can see that the first step of photodegradation of MB, it is likely to provoke a loss in color that it measured as k variation; however no variation in refractive index (at 1000 nm) is expected since the photodegradation product after the first step remains into the pores (non-volatile at room temperature according to the literature). A significant drop in refractive index could be expected in the last step of the photodegradation process when the non-volatile phenylsulphonic acid (solid at room temperature) is converted to volatile phenol molecules that are readily desorbed from the layer.

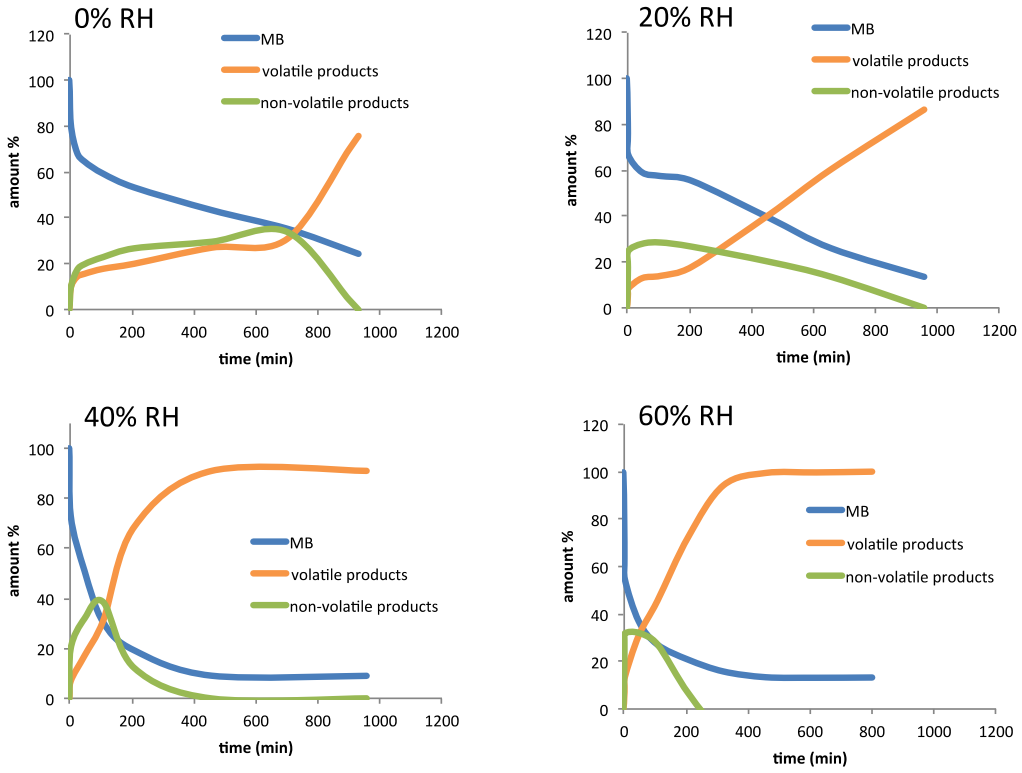

Figure 2.22 *Evolution of the amount of MB and photodegradation products as function of time and for different RH.*

While this aspect would need complementary analysis, at this preliminary stage some conclusions can be drawn: taken with care, results on photodegradation rate suggests that MB can be used as probe for ellipsometric investigations in order to obtain information on the photodegration stage. In a single measurement, one can imagine to probe the advancement of the photodegradation process at the early stages by monitoring k and at advanced stages by monitoring n (1000 nm). In this regard, the amount % of each compound can be thus be evaluated as following: %A = %MB; (%N-%A) = % non-volatile product; (100 - %MB -

%non-volatile products) = % volatile products. The evolutions as function of the time and the humidity are plotted in Figure 2.22. In all the cases, the %MB is decreasing with time while the % of volatile product is increasing). Looking back to the results in Figure 2.20 (c), the difference between the normalize n (1000 nm) and amplitude can be seen as the concentration of non-volatile, intermediate products of the photodegradation into the pores. For all the RH%, the concentration of non-volatile, intermediate products is increasing at the beginning as product of the first steps of the decomposition process. The concentration is then dropping down due to the further photodecomposition (and consumption) of the non-volatile, intermediate products towards volatile products. Increasing the water content (RH%) leads to a fastening of these two processes as expected.

2.5 Conclusions

In this chapter we showed that ellipsometry is a useful technique to follow photocatalytic efficiencies of porous thin films by following the refractive index diminution associated to the decomposition of impregnated organic pollutants. It offers here a simple, alternative and complementary method to evaluate the roles of the atmospheric composition in O_2 and H_2O on the reactivity. We demonstrated that cleaning a porous semi-conductor films from its impregnated pollutant does not follow a strict-first order kinetic due to the fluctuation in O_2 and H_2O content in the pores as dictated by exchange equilibriums and accessibility of sites for scavenger stabilisation. It is proposed that higher efficiencies was obtained for an optimal ratio and repartition of scavenger/pollutant in the “moderate-dry” conditions, and when pores content liquid water from capillary condensation at high RH. In addition, this study proves that the evaluation of the photocatalytic activity of a given material performed in presence of liquid water is significantly different from that measured in atmosphere, especially for nanoporous photocatalysts. Thus, usual results of literature obtained from decomposition tests performed in solution should be taken with care whenever atmospheric photocatalysis application is targeted. For this reason, the ellipsometric analysis tool presented here is a very powerful analytical strategy allowing the measurement of the reactivity gap in between both catalytic tests conditions. We also investigate here the influence of the organic probe by using Methylene blue as pollutant and discussing its efficacy to monitor photocatalysis. An optical model was developed to describe the optical response of the dye and its monomeric or

dimeric forms. We highlight that photoreduction occurs when MB is used in O_2 free environments. Experiments in controlled humid atmosphere were conducted. By monitoring independently the real and the imaginary part of refractive index, the results on photodegradation rate suggested that MB can be used as probe for ellipsometric investigations in order to obtain information on the photodegration advancement.

References

1. Tong H, Ouyang S, Bi Y, et al. Nano-photocatalytic materials: possibilities and challenges[J]. Advanced Materials, 2012, 24(2): 229-251.
2. Gaya U I, Abdullah A H. Heterogeneous photocatalytic degradation of organic contaminants over titanium dioxide: a review of fundamentals, progress and problems[J]. Journal of Photochemistry and Photobiology C: Photochemistry Reviews, 2008, 9(1): 1-12.
3. Costacurta S, Maso G D, Gallo R, et al. Influence of Temperature on the Photocatalytic Activity of Sol-Gel TiO_2 Films[J]. ACS applied materials & interfaces, 2010, 2(5): 1294-1298.
4. Obee T N, Brown R T. TiO_2 photocatalysis for indoor air applications: effects of humidity and trace contaminant levels on the oxidation rates of formaldehyde, toluene, and 1, 3-butadiene[J]. Environmental Science & Technology, 1995, 29(5): 1223-1231.
5. Henderson M a. A surface science perspective on TiO_2 photocatalysis. Surf Sci Rep. 2011, 66(6-7):185-297.
6. Carretero-Genevrier A, Boissiere C, Nicole L, et al. Distance dependence of the photocatalytic efficiency of TiO_2 revealed by in situ ellipsometry[J]. Journal of the American Chemical Society, 2012, 134(26): 10761-10764.
7. Remillard J T, McBride J R, Nietering K E, et al. Real time in situ spectroscopic ellipsometry studies of the photocatalytic oxidation of stearic acid on titania films[J]. The Journal of Physical Chemistry B, 2000, 104(18): 4440-4447.
8. Faustini M, Nicole L, Boissiere C, et al. Hydrophobic, antireflective, self-cleaning, and antifogging sol− gel coatings: an example of multifunctional nanostructured materials for photovoltaic cells[J]. Chemistry of Materials, 2010, 22(15): 4406-4413.
9. Roncaroli F, Martínez E D, Soler-Illia G J A A, et al. Mesoporous Thin Films of TiO_2 on Attenuated Total Reflection Crystals. An In Situ Fourier-Transform Infrared Study of the Kinetics and Equilibrium of Adsorption and Photocatalysis of Carboxylic Acids[J]. The Journal of Physical Chemistry C, 2013, 117(29): 15026-15034.
10. Soler-Illia G J A A, Angelomé P C, Fuertes M C, et al. Critical aspects in the production of periodically ordered mesoporous titania thin films[J]. Nanoscale, 2012, 4(8): 2549-2566.
11. Obee T N, Brown R T. TiO_2 photocatalysis for indoor air applications: effects of humidity and trace contaminant levels on the oxidation rates of formaldehyde, toluene, and 1, 3-butadiene[J]. Environmental Science & Technology, 1995, 29(5): 1223-1231.

12. Sakatani Y, Grosso D, Nicole L, et al. Optimised photocatalytic activity of grid-like mesoporous TiO_2 films: effect of crystallinity, pore size distribution, and pore accessibility[J]. Journal of Materials Chemistry, 2006, 16(1): 77-82.
13. Houas A, Lachheb H, Ksibi M, et al. Photocatalytic degradation pathway of methylene blue in water[J]. Applied Catalysis B: Environmental, 2001, 31(2): 145-157.
14. Mills A, Wang J. Photobleaching of methylene blue sensitised by TiO_2: an ambiguous system?[J]. Journal of Photochemistry and Photobiology A: Chemistry, 1999, 127(1): 123-134.

CHAPTER 3

Formation and photocatalytic activity of mesoporous TiO_2/SiO_2 composite films

As discussed in Chapter 2, in-situ ellipsometry can be used to investigate the influence of the environmental conditions (humidity, oxygen content) on the photocatalytic activity of a model mesoporous TiO_2 film. In this chapter we will focus on the composition and morphology of the porous photocatalytic coatings. Mesoporous TiO_2/SiO_2 composite films are synthetized and their porous structure and composition are characterized. The photocatalytic performances are evaluated by in-situ ellipsometry. This composition was chosen since this mixed system theoretically allows tuning the optical properties and reducing the porous network collapse upon thermal treatment. From the application point of view, the fabrication of photocatalytic coatings with well-controlled optical properties (such as transparency on glass) is of great interest for their application in functional optical systems.

3.1 Introduction

As mentioned in Chapter 1, TiO_2 thin films are widely used for many applications varying from photodecomposition, self-cleaning[1,2], environmental sensing[3,4], super hydrophilic layers[5-7], photovoltaic energy[8] and so on. The properties of the material could be tuned by adding other elements such as doping with carbon, nitrogen, fluorine, sulfur, or novel metal particles: Pt(IV), Ir(IV) and Au(III).[9-13] In this chapter we focus on the role of SiO_2 on the structural, optical and chemical properties of TiO_2 based thin films.

Photocatalytic TiO_2 mesoporous films (like the ones described in Chapter 2) are extremely attractive since they can be applied on glass (transparent windows) and act as superhydrophilic, photoactive, self-cleaning layers for air-depollution. These coatings are transparent in the visible range, however, in most of the previous reports, the minimal refractive index was barely obtained below 1.6-1.7. This relative high value is due to the fact that pure crystalline TiO_2 presents a very high refractive index, $n \approx 2.4$ in the visible range. In this configuration, a mesoporous titania film ($n > 1.6$) applied on a glass substrate ($n \approx 1.45$) will also act as a reflective coating, lowering the amount of transmitted light through the glass substrate. In this context, being able to tune the refractive index toward lower values of such photocatalytic layers would be beneficial for their application as functional glasses. One way to lower the refractive index is to increase the total porous volume. On the other hand, highly porous TiO_2 layers are difficult to obtain because of the collapse of the inorganic network due to diffusive sintering during thermal treatment. From the optical point of view, adding SiO_2 to the matrix slightly reduces the refractive index of the inorganic phase, due to its low refractive index compare to that of TiO_2. In addition it has been observed in a previous paper of our group for dense films that in presence of a small amount of silica, the growth of TiO_2 anatase nanoparticles by diffusive sintering is totally hindered even at 800°C.[14] This effect is expected to have a strong influence on final structure of the mesoporous films and on the crystal size, stabilizing the porous network during the thermal treatment. Concerning the photocatalytic properties, the addition of "inert" silica to an active TiO_2 matrix should decrease the photocatalytic efficiency compare to pure titania. However it has been demonstrated that silica could also have beneficial effect to the photocatalytic process due to an increase of the adsorption of the pollutants.[15]

The chemistry and the formation of mixed TiO_2/SiO_2 systems have been extensively studied

in the last decades.[16-18] More recently, it has been reported that photocatalytic reactivity of TiO_2/SiO_2 nanocomposite powders is highly dependent on the Ti/Si ratios. The mechanical stability was reported to be improved by the addition of SiO_2.[19-27] It is well known that the photocatalytic activity of titania is strongly dependent on the synthesized crystal size.[28] In particular, it was reported that the crystal size of titania decreases with the increase of silica ratio in the case of dense composite TiO_2/SiO_2 films.[29,14] Despite a very rich literature on these mixed systems, the structural, optical and photocatalytic properties of TiO_2/SiO_2 composite mesoporous films were barely investigated so far.

In the following section we will report an investigation of the photocatalytic activity of mesoporous TiO_2/SiO_2 composites films with variable Ti/Si ratios (0%-100%) based on an ethanolic EISA synthesis process by using $TiCl_4$ and tetraethyl orthosilicate (TEOS) as precursors and triblock copolymer F127 as template. All the films were thermal treated at 600°C. The evolution of porous, crystalline structure, optical properties and the photocatalytic activity of the TiO_2/SiO_2 composite films of different SiO_2 ratios were studied.

3.2 Preparation of mesoporous composite TiO_2/SiO_2 films

The composite films were prepared by EISA method. Exactly the same procedure as the one use to prepare the mesoporous pure titania thin film d in Chapter 2 was applied. Titanium tetrachloride ($TiCl_4$) and Tetraethyl orthosilicate ($Si(OC_2H_5)_4$) were used as precursors of TiO_2 and SiO_2 respectively and Pluronic triblock copolymer F127 was used as a structuring agent. A total of 11 compositions were used in this investigation: 100% TiO_2/0% SiO_2, 98% TiO_2/2% SiO_2, 90% TiO_2/10% SiO_2, 80% TiO_2/20% SiO_2, 70% TiO_2/30% SiO_2, 60% TiO_2/40% SiO_2, 50% TiO_2/50% SiO_2, 40% TiO_2/60% SiO_2, 30% TiO_2/70% SiO_2, 20% TiO_2/80% SiO_2, 0% TiO_2/100% SiO_2. The initial solution compositions (in grams) are listed in Table 1. The pure mesoporous titania thin film (100% TiO_2/0% SiO_2) was exactly the same as the one described in Chapter 2. The solution was composed of $TiCl_4$: F127: H_2O: EtOH with respective molar ratio of 1: 0.006: 10: 30, corresponding to 4.08g Ti5E, 0.8g F127, 1.75g H_2O, 13.36g EtOH. For comparison purpose, the pure amorphous silica mesoporous film (0% TiO_2/100% SiO_2) was synthesised following the same procedure as the pure titania film, taking TEOS instead of Ti5E as precursor, and adding 0.005 molar ratio hydrochloride (2M) for the initial solution preparation. The solutions were prepared under vigorous stirring

before deposition.

As described in previous chapter, the silicon substrate was dipped into the as prepared sol solution with a speed at 3 mm/s at room temperature of around 22℃, under dry air atmosphere (RH < 2%). The as made films were then aged for 10 minutes at 75% relative humidity and 37℃, and were then calcined at 600℃ during 10 minutes. In the case of pure silica porous films, the calcination temperature was set at 500℃.

Table 1 Compositions investigated in mol% and initial solution ingredients in gram.

TiO_2 (mol%)	SiO_2 (mol%)	Ti5E (g)	TEOS (g)	F127 (g)	EtOH (g)	HCl (g)	H_2O (g)
100	0	4.08	0.00	0.80	13.36	0	1.75
98	2	4.01	0.04	0.80	13.39	0	1.75
90	10	3.71	0.20	0.81	13.50	0	1.77
80	20	3.33	0.41	0.82	13.64	0	1.79
70	30	2.95	0.63	0.83	13.79	0	1.80
60	40	2.55	0.84	0.83	13.94	0	1.82
50	50	2.15	1.07	0.84	14.09	0	1.84
40	60	1.74	1.29	0.85	14.24	0	1.86
30	70	1.32	1.52	0.86	14.40	0	1.88
20	80	0.89	1.76	0.87	14.56	0	1.91
0	100	0.00	1.94	0.26	17.5	0.023	0.81

3.3 Porosity Characterization

The structure of the porous network of composite TiO_2/SiO_2 films was accessed by EEP, GI-SAXS and SEM. Figure 3.1 shows the water adsorption-desorption isotherms of mesoporous composite TiO_2/SiO_2 films with various Ti/Si ratios measured by ellipsometry porosimetry. The shapes of the adsorption-desorption hysteresis curves clearly evolve with the composition of the inorganic network.

The reference TiO_2 mesoporous film (0%TEOS) is characterized by a narrow adsorption–desorption hysteresis suggesting that the mesopores are highly interconnected through large pore windows as already observed in the previous chapter. Adding SiO_2 to the inorganic network lead to a progressive broadening of the hysteresis loops. The broad adsorption–desorption hysteresis observed for the 100% silica is characteristic for mesoporous materials with cage-like porosity, i.e. larger pores connected through smaller pore windows. Above 50%SiO_2, a slight increase in adsorbed H_2O at lower P/P_0 (<10%) can be attributed to the presence of micropores as typically observed for SiO_2 mesoporous materials templated by PEO-based structuring agents.

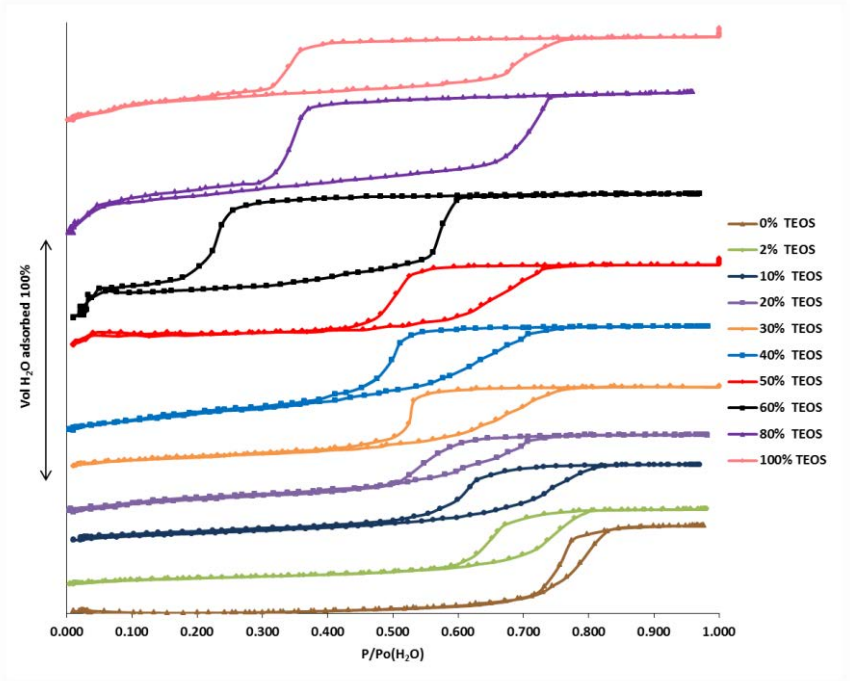

Figure 3.1 *Adsorption-desorption isotherms plotted for mesoporous films composited with x%SiO_2(TEOS)/(1-x%)TiO_2 by Ellipsometry porosimetry.*

The evolution of the porous structure can be further described in terms of Pore Size Distribution (PSD), extracted from the adsorption and desorption branches data of isotherm curves using the modified Kelvin equation. Pore size distribution are shown in Figure 3.2 A), B) for four representative samples with different compositions (*e.g.* 100%TiO_2/0%SiO_2, 60%TiO_2/40% SiO_2, 20% TiO_2/80% SiO_2, 0% TiO_2/100% SiO_2).

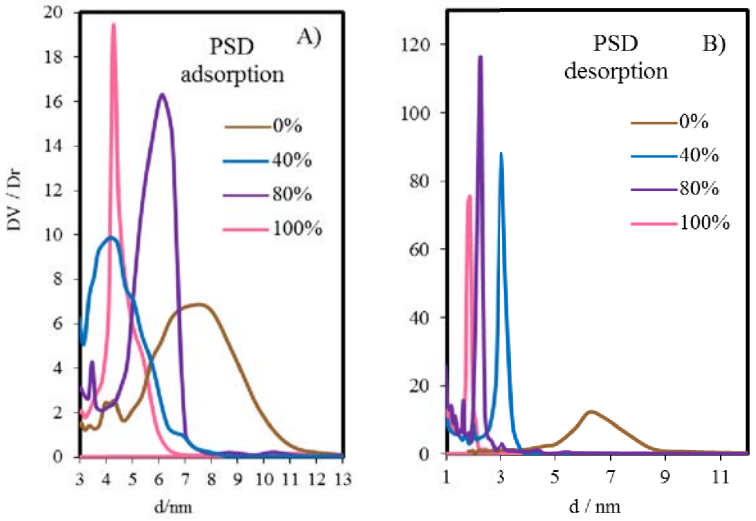

Figure 3.2 *Pore size distributions extracted from the adsorption (A) and desorption (B) branches of isotherms of 0%, 40%, 80%, 100% TEOS given in Fig. 3.1.*

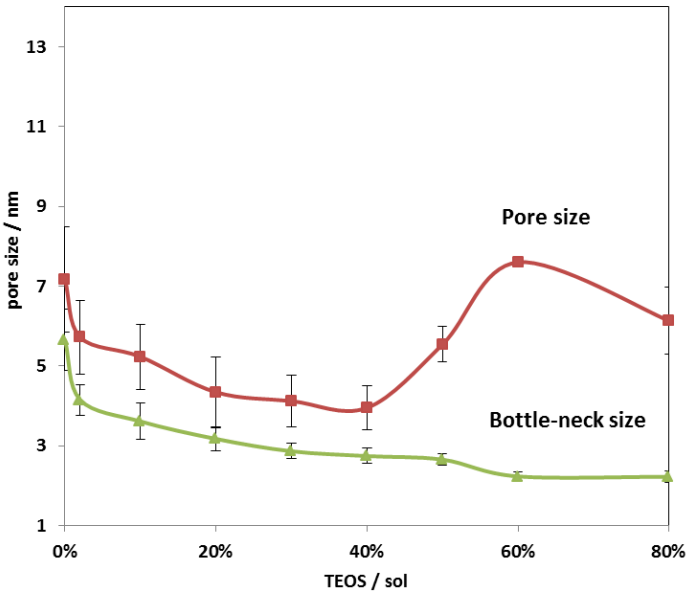

Figure 3.3 *Pore size distribution and bottle neck size distribution evolutions with increasing ratio of SiO_2.*

Figure 3.2 and Figure 3.3 show the evolution of average pore and bottle-neck depending on the composition in SiO_2. The average pore and bottle-neck sizes vary from 7.8 to 4.4 and

from 6.4 to 1.9, respectively. In general, the bottle-neck size decrease with the increase of SiO_2. The average pore size decreases with the increase of SiO_2 content until a composition of 40%SiO_2/60%TiO_2, where it increases back for higher SiO_2 content. This can be attributed to a modification of the pore network morphology as will be discussed later.

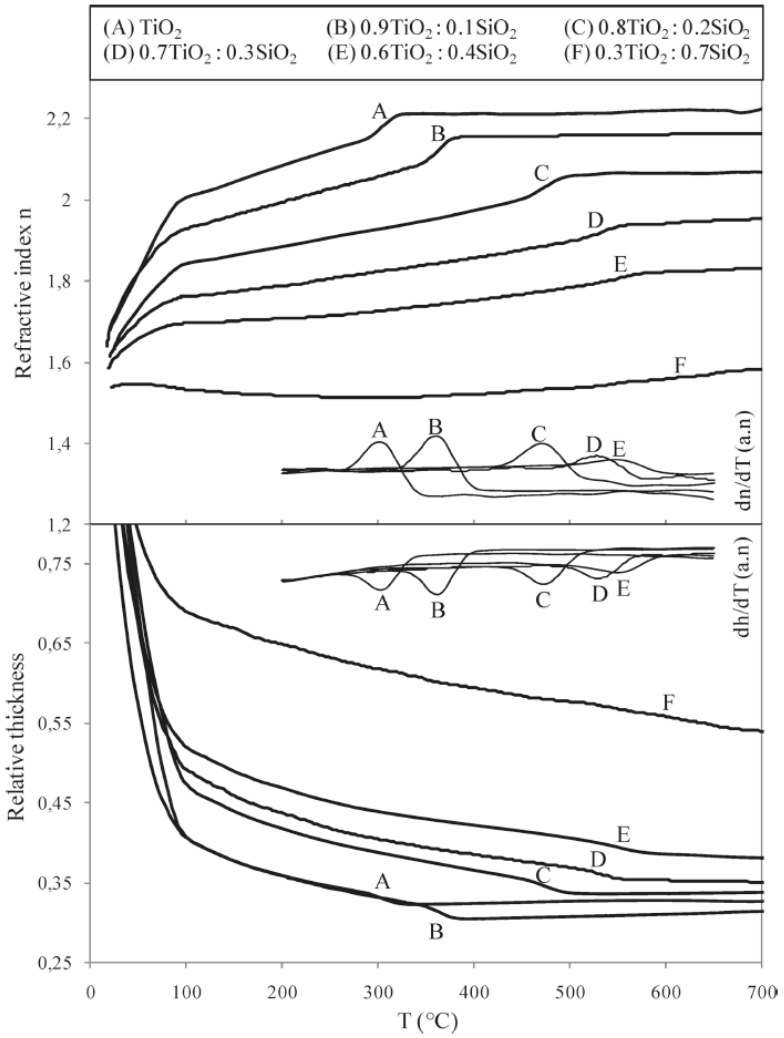

Figure 3.4 *Evolutions of the refractive index n (up) and the thickness h (down) of dense films with the temperature for different $xTiO_2$:(1-x)SiO_2 compositions, (A, x = 1; B, x = 0.9; C, x = 0.8; D, x = 0.7; E, x = 0.6; F, x = 0.3). Corresponding derivative curves are also plotted, inset.*[14]

The porous volume can be evaluated by using the Bruggemann Effective Medium Approximation (BEMA) model as follows:

$$f_A \frac{\tilde{\varepsilon}_A - \tilde{\varepsilon}}{\tilde{\varepsilon}_A + 2\tilde{\varepsilon}} + f_B \frac{\tilde{\varepsilon}_B - \tilde{\varepsilon}}{\tilde{\varepsilon}_A + 2\tilde{\varepsilon}} = 0$$

It allowed the determination of the relative volumetric fractions f_A and f_B of two materials A and B of known dielectric constants ε_A and ε_B within a volume unit of measured dielectric constant ε. Since air, SiO_2 and TiO_2 do not adsorb light in the considered range of wavelengths (400−1000 nm), the dielectric constants are taken to be the square of the refractive index values (real part of the dielectric constants). The determination of layer porous volume was obtained by fitting the volumetric fractions of air and silica/titania. In our case the component A is air (n=1) while the component B is the silica/titania matrix. The values of refractive index of the silica/titania dense materials treated at 600°C were obtained from a previous publication as shown in Figure 3.4.

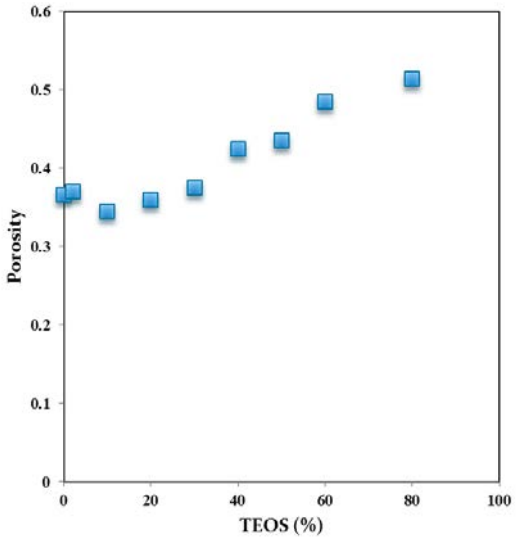

Figure 3.5 *Porosity evolution with increasing ratio of SiO_2.*

The evolution of the porous volume fraction is shown in Figure 3.5. For low silica content (< 30%) the percentage of pore volume is constant around 35%. It then increases up to a maximum value of 50% for 20% TiO_2/80% SiO_2. This evolution of the porosity is mainly related to the variation in contraction and morphology of the porous network due to the addition of silica. For pure TiO_2, high temperature crystallisation and diffusive sintering usually induce a partial collapse of the network followed by densification and partial loss of the porosity. Because the silica stays amorphous in the film, it avoids the collapse of the film and decrease shrinkage under calcination. This effect has been already demonstrated for silica/titania dense films as shown in Figure 3.4 in which the shrinkage can be estimated by the values of relative thickness at 600°C.

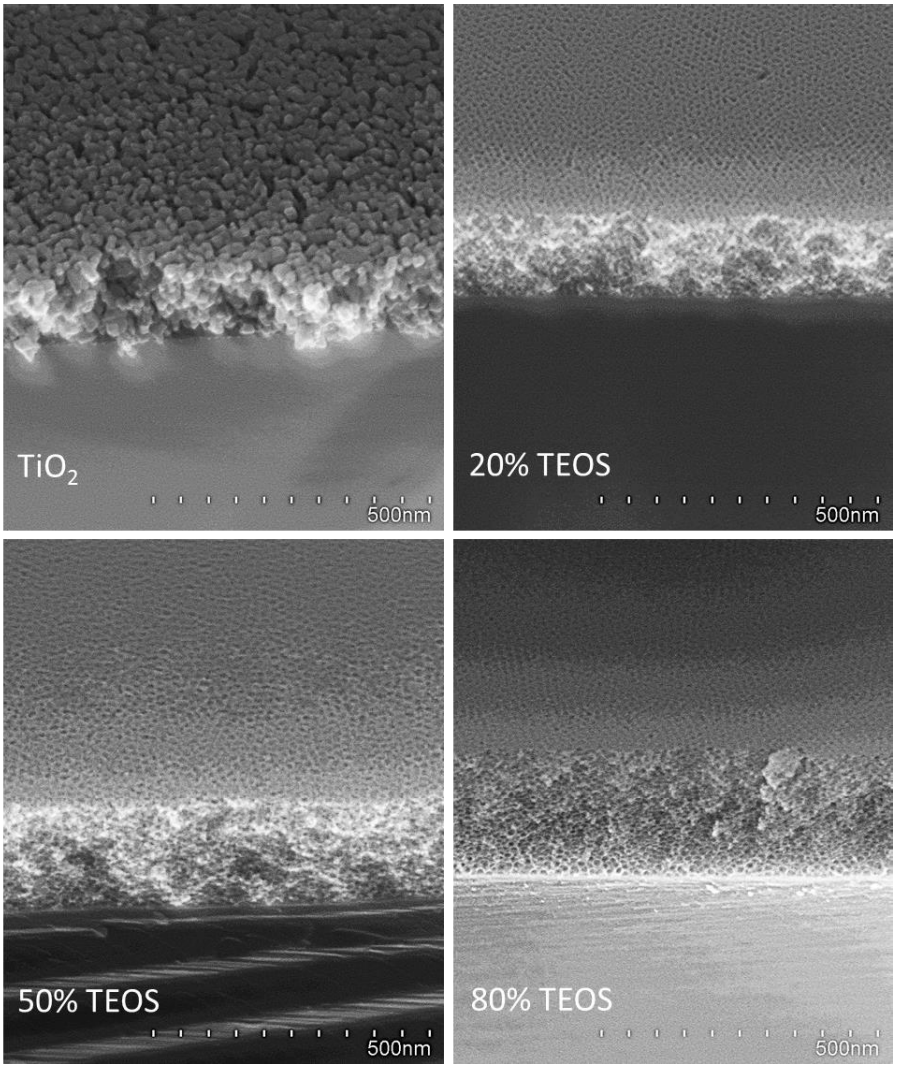

Figure 3.6 *SEM morphology of samples with composition of 100% TiO_2/0% SiO_2, 80% TiO_2/20% SiO_2, 50% TiO_2/50% SiO_2 and 20% TiO_2/80% SiO_2.*

The morphology of the porous network was accessed by SEM and GI-SAXS investigations. The SEM micrographs of four representative films with composition of 100% TiO_2/0% SiO_2, 80% TiO_2/20% SiO_2, 50% TiO_2/50% SiO_2 and 20% TiO_2/80% SiO_2 are shown in figure 3.6. The porous network can be easily distinguished for all samples. As seen in Chapter 2, pure mesoprous TiO_2 is characterized by an open, "grid-like" structure. In the other cases, where SiO_2 was added, the network of spherical/elliptical pores can be identified with a short-range organization, characteristic of a so-called "worm-like" morphology. The values of pore sizes and periodicity, observed by SEM are consistent with EEP evaluation. An open and highly accessible network is observed for pure mesoporous TiO_2 films as explained in Chapter 2.

The GI-SAXS patterns of the mesoporous composite TiO_2/SiO_2 films with different SiO_2 content 2%, 5%, 20%, 30%, 40%, 50%, 60%, 80%, 100% are shown in Figure 3.7. The GI-SAXS results reveal characteristic diffraction patterns that indicates that the pore network morphology evolves gradually from grid-like to worm-like structure with the increase of the SiO_2 content.

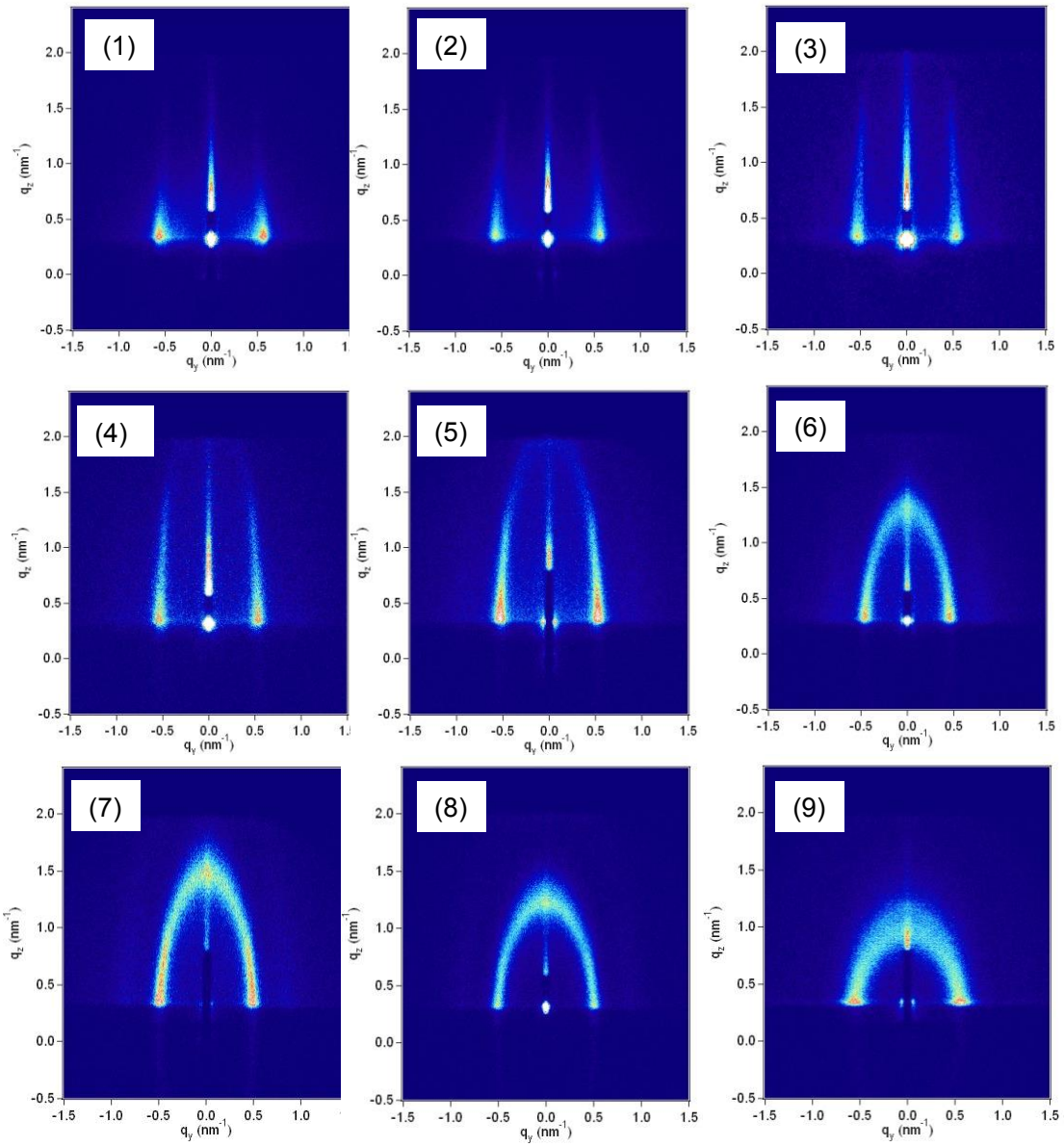

Figure 3.7 *GI-SAXS patterns of the mesoporous composite TiO2/SiO2 films with different SiO_2 content (1) 2%; (2) 5%; (3) 20%; (4) 30%, (5) 40%, (6) 50%, (7) 60%, (8) 80%, and (9) 100%.*

The plot of the diffraction intensity versus q_y obtained by the GI-SAXS patterns for the composite layers is shown in Figure 3.8. The position of the intensity peak in the q_y direction allows estimating the in-plain pore periodicities by the relation $d = 2\ \pi/q_y$. The periodicity distance is calculated to be 11-12 nm for all the samples with the exception of 50%SiO_2/TiO_2 samples that exhibits a slightly larger periodicity value of 13.5 nm. The reason for such difference is yet not clear, however all relative values are in agreement with the previous literature concerning F127-templated mesoporous films where periodicities are usually comprise between 11 and 14 nm.

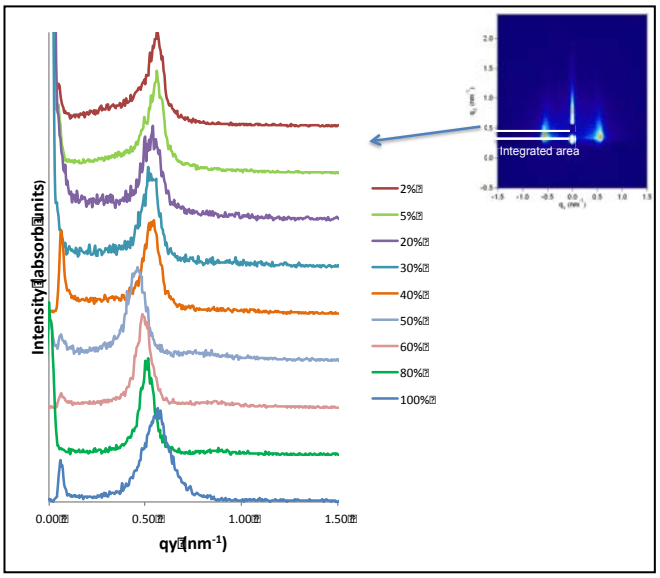

Figure 3.8 *Diagram of the intensity profiles in the y direction integrated on the dashed white line of a typical GISAXS pattern (in the inset)*

From the previous characterisation results a morphological evolution of the porosity as function of the TiO_2/SiO_2 composition can be proposed in Figure 3.9. For TiO_2 rich films a grid-like morphology of the porosity can be pictured. The single intense diffraction signal corresponds to periodical planes oriented perpendicular to the substrate surface. This structure is characterized by a highly open and accessible porous network, as confirmed by the narrow EEP hysteresis characteristic of a small difference between pore and bottleneck sizes. The progressive substitution of part of TiO_2 by SiO_2, makes the porous network evolves gradually from an "open" grid-like to a worm-like structure. The GI-SAXS patterns and the large EEP hysteresis of SiO_2-rich layers indicate that the network is composed of spherical/elliptical pores with smaller bottlenecks. For the worm-like morphology, the anisotropy of the elliptical pores increases with the TiO_2 content due to the larger contraction and densification of the

films. The larger pore anisotropy can be observed in the GI-SAXS image for highly contracted pores, in which the diffraction pattern is elongated to higher values in the z direction of the reciprocal space. This analysis does not take into accont the structure of the composite crytallite/amorphous material localized into the walls. This aspect is discussed further.

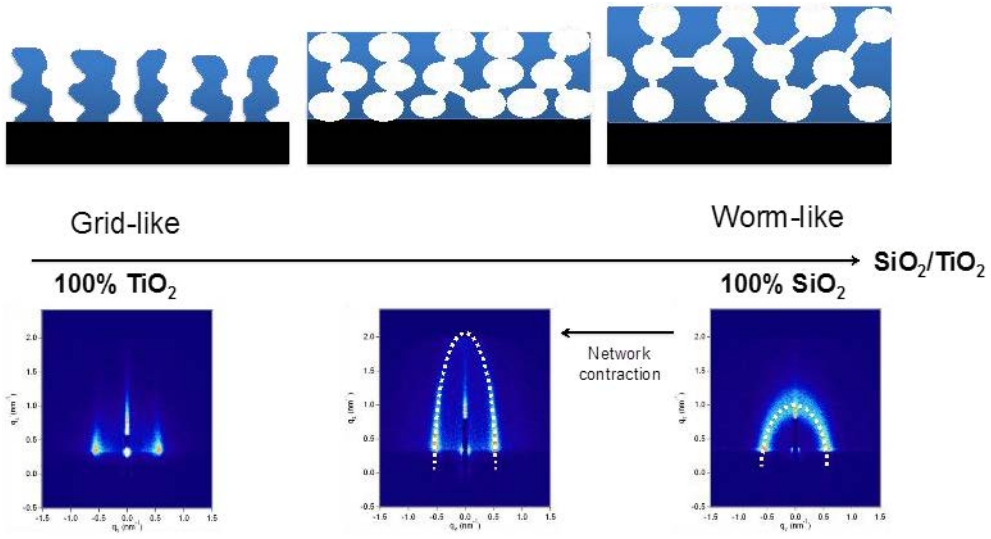

Figure 3.9 *Porosity morphology evolution following with GI-SAXS patterns.*

3.3 Characterization of the Crystalline Network

The Anatase crystals characterization was carried out by Grazing Incidence Wide angle X-Ray Scattering (GI-WAXS) and by High resolution Transmission Electron Microscopy (HR-TEM). Attempts have been performed in using the X-Ray diffraction analysis in the conventional Bragg-Brentano configurations. However, due to the low amount of crystalline matter and the small size of the crystallites in the films, diffraction signals remain in the background especially for SiO_2-rich samples. For this reason GI-WAXS was chosen as the main analytical tool.Figure 3.10 shows the GI-WAXS plots of mesoporous composite films for various SiO_2/TiO_2 ratios. In particular, the intensity (in logarithmic scale) is plotted as function of 2θ. The GI-WAXS plots show four broad diffraction peaks characteristic of anatase phase[30-32], suggesting the formation of TiO_2 nanocrystallites. The major peak at 2θ=25.4° corresponds to the (101) reflection of the anatase phase, which is present in most of the mesoporous TiO_2/SiO_2 composite films except for the pure SiO_2 and the

80%SiO_2/20%TiO_2 samples. The other peaks in GI-WAXS patterns are respectively related to the (200), (112), and (105) planes of the anatase phase. The peak relative intensity decreases with the increasing composition in SiO_2 (from 2% to 100%), suggesting a decrease in crystallinity in the films.

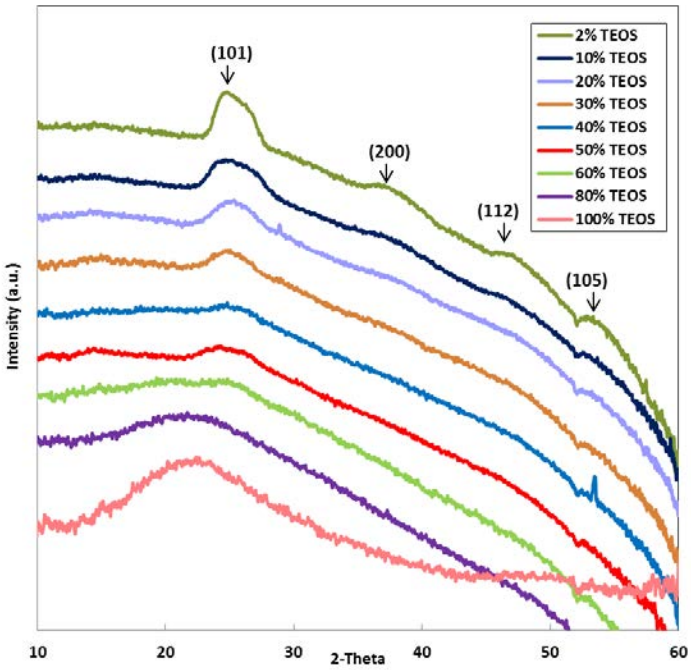

Figure 3.10 *GI-WAXS patterns of mesoporous films with increasing components of x%TEOS((1-x)%TiO_2/x%SiO_2) in logarithm of intensity.*

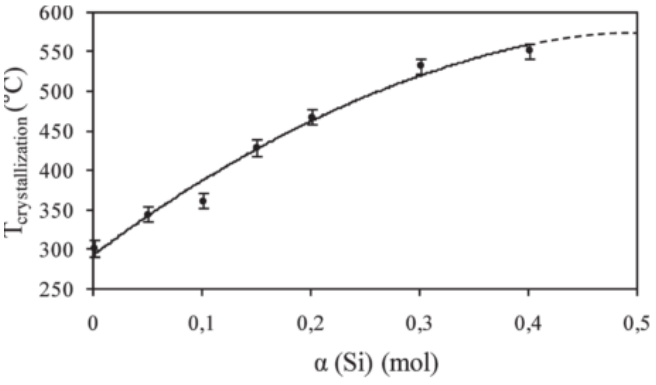

Figure 3.11 *Influence of the SiO_2 content (R) on the crystallization temperature of TiO_2 in mixed $xTiO_2$:(1-x)SiO_2 films (α = 1-x).*[14]

A similar trend was observed in a previous study for dense films.[14] As shown in Figure 3.11, it was demonstrated that the crystallization temperature increases with the Silica content in the TiO_2 matrix due to fact that the silica network, if intimately mixed with titanium oxo species, and acts as barriers to their diffusion which tends to inhibit the nucleation-growth of TiO_2 crystallites.

Crystallite size evaluation, using the Scherrer method, could not be done with the present XRD diagram because the grazing incidence geometry used for the analysis induces the diffracted beam broadening that is directly dependent on the sample size. High-resolution transmission electron microscopy (HRTEM) images are displayed in Figure 3.12. The TEM micrographs evidence the presence of the nanoporous network. The average pore size estimated by HR-TEM images is in the range of between 5 and 8 nm, that is consistent with the previous EEP characterization. In addition nearly spherical TiO_2 anatase nanocrystals can be distinguished (dark spots). For samples with higher SiO_2 content, the TiO_2 crystals are embedded into a SiO_2 (and TiO_2) amorphous matrix as in the case of 50% TEOS sample. No particles were observed for 80% TEOS sample that is in consistent with the GI-WAXS results.

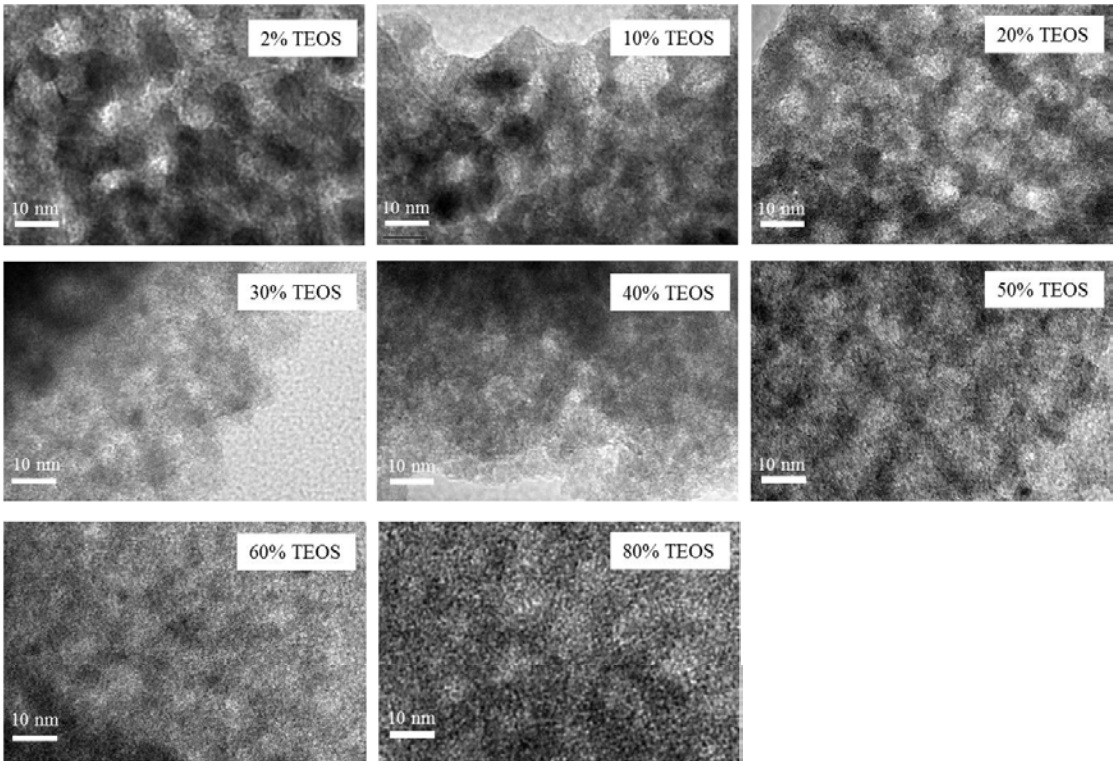

Figure 3.12 *HRTEM micrograph of TiO_2 nanoparticles of mesoporous TiO_2/SiO_2 composite films.*

The average particle structure and size was determined by image analysis from the several HR-TEM micrographs with the support of software Image J. For example considering the inserted HRTEM picture of 2%TEOS, a single crystal is highlighted in which the plain distance of 3.5Å corresponds to (101) plain of Anatase crystal in agreement with GI-WAXS results. In order to determine the average particle size, image analysis was performed by averaging the dimension value of at least 20 particles. For instance in the case of the 2% TEOS sample in Figure 3.13, where the nanocrystals are highlighted by a red circles, the calculated mean size is ~8.4nm. The evolution of the average particle size as function of the SiO_2/TiO_2 molar ratio is shown in Figure 3.14. It can be seen that the crystal size decreases with the SiO_2 content from 8 nm down to 3.5 nm.

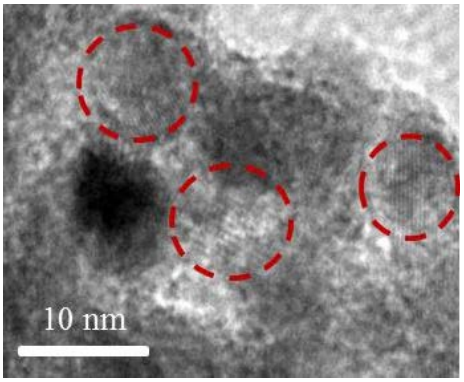

Figure 3.13 *HR-TEM micrograph of 2% TEOS sample. The anatase nanocrystals are highlighted by a red circles.*

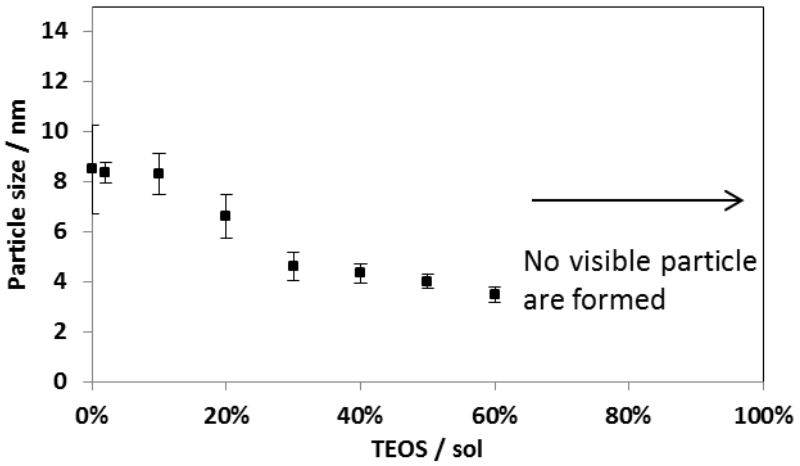

Figure 3.14 *Particle size evolution calculated by HR-TEM micrograph of TiO_2 nanoparticles.*

3.4 Formation and evolution of the mesostructure

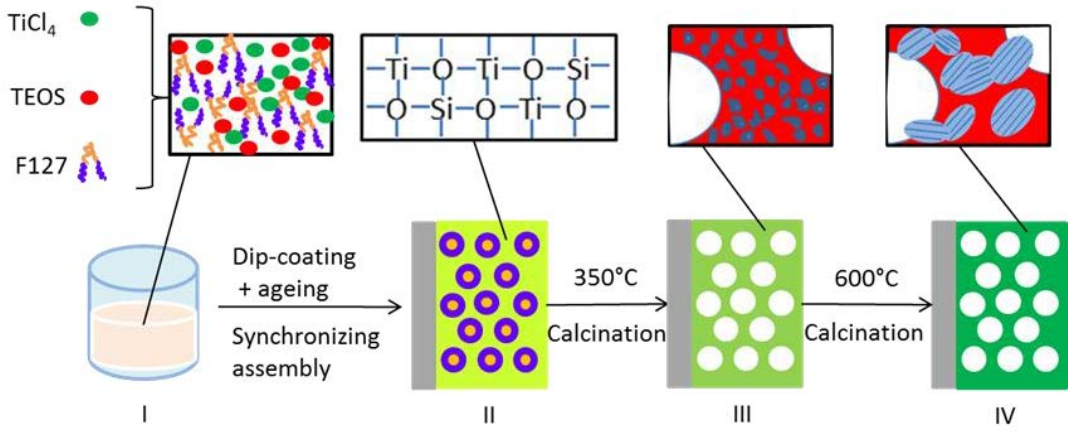

Figure 3.15 *Scheme for the TiO_2/ SiO_2 composite mesoporous film formation.*

A proposition of film formation is illustrated in Figure 3.15. The formation of mesostructured TiO_2/SiO_2 nanocomposite film involves an evaporation induced self-assembly process of amphiphilic triblock copolymer F127 together with titanate and silicate oligomers. In large excess of HCl, such as in our conditions, it has been demonstrated previously that the final nanocomposites have a uniform and homogeneous framework with well dispersed silicates, in which both silicate and titanate oligomers can cross-link together and contribute the mesostructured frameworks without phase separation.[28] After deposition and self-assembly, the template F127 starts to decompose at 350°C and the mesopores are liberated. Simultaneously, the titanate species are aggregated and the homogeneous amorphous frameworks start to crystallize because of the thermodynamic metastability of titania during the heat treatment.[32] The crystallisation occurs above 300°C depending on the composition in silica as shown in Figure 3.11. The nuclei and nanocrystals of TiO_2 are formed around the pore walls. At this moment, the phase separation occurs and anatase TiO_2 nanocrystals are randomly embedded in the matrixes of amorphous TiO_2 and SiO_2. The phase separation continues to progress through TiO_2 nanocrystals further grow by prolonging the heat treatment time. During this stage, the silica matrix located around the Anatase crystallites further cross links, stiffening at the same time the whole structure. Further growth of TiO_2 crystallites through Ostwald ripening (diffusive sintering) is then quenched due to the presence of the silica matrix that inhibits the diffusion of titania-oxo species. The amorphous silica framework also prevents the framework from collapsing.

3.5 Optical properties of the composite films

Fitting the ellispometric results by a Cauchy model allows determination of the dispersion of the refractive index in the visible range (from 450nm to 1000 nm) as shown in Figure 3.16. The curves show the optical properties of the layers as function of the composition; in addition the dispersion curve of a bare glass substrate is shown too. From these results we can roughly evaluate the optical behaviour of the SiO_2/TiO_2 layers if applied on glass substrates. Samples having dispersion of refractive indices higher than that of the glass will behave as reflective coatings (SiO_2 content > 40%). Layers with lower refractive index will behave as (poor) anti-reflective coatings. In both cases a structural colour will appear (depending on the thickness of the coatings). Interestingly the coating having composition of 40%SiO_2 exhibits similar refractive index dispersion as the bare glass substrate. In this case the coating will behave as inactive optical system on glass regardless of its thickness.

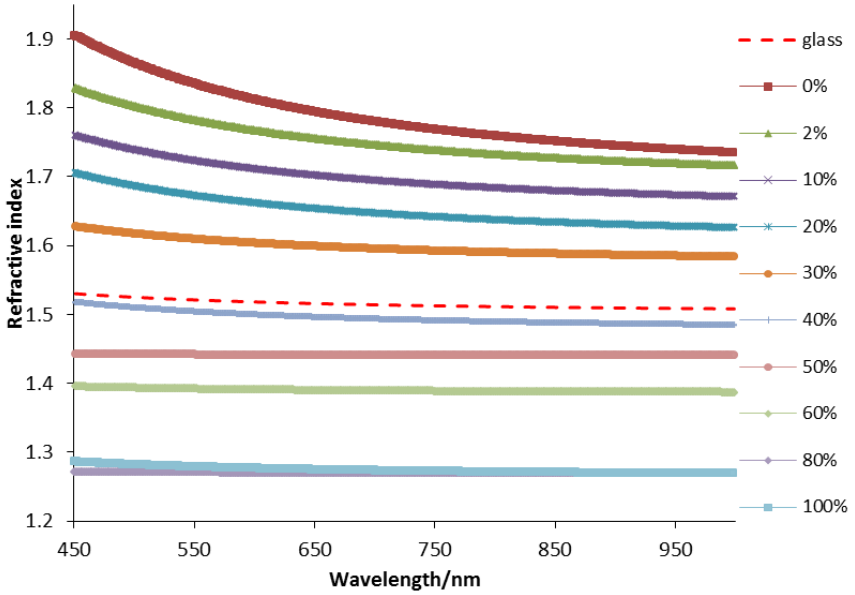

Figure 3.16 *Evolution of the dispersion of refractive index for the nanocomposite films for different silica content and for bare glass.*

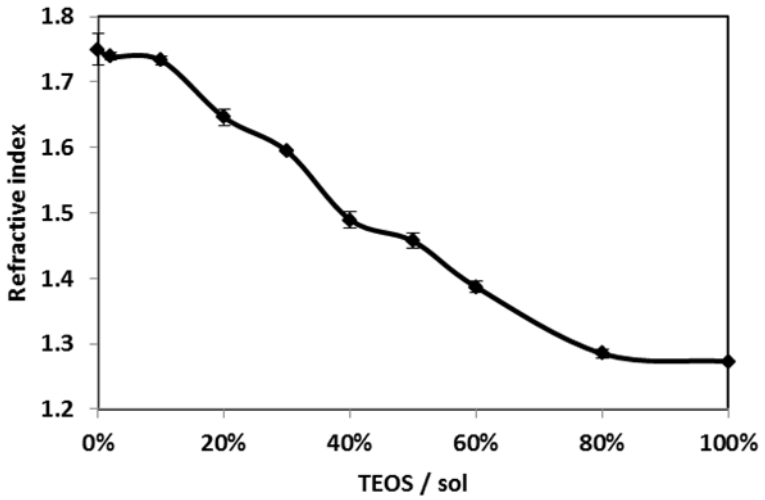

Figure 3.17 *Evolution of the refractive index at wavelength 700 nm for different SiO_2 content.*

Figure 3.17 shows the evolution of the refractive index (at 700 nm) of the mesoporous SiO_2/TiO_2 nanocomposite films investigated by ellipsometry. As explained previously, adding SiO_2 to the matrix should reduce the refractive index of the inorganic phase, due to its lower refractive index (n_{SiO2} =1.45) compare to that of TiO_2 (n_{TiO2} =2.3) . From the experimental results it is clear that a progressive decrease in refractive index evolution varying from 1.74 to 1.27 (at wavelength 700nm) is obtained with the increasing Si/Ti ratio.

3.6 Photocatalysis activity of the composite films

The photocatalytic activity of the films was investigated by in-situ ellipsometry. In order to study the photocatalysis activity of the composited TiO_2/SiO_2 mesoporous films, lauric acid was infiltrated into the porosity by dip-coating at a speed of 15mm/s from an ethanolic solution of concentration 0.5 wt%. The irradiation was operated in a closed chamber with controlled atmosphere maintained at 40% humidity as detailed in Chapter 2. The humidity atmosphere was chosen at 40% because, as indicated from the study of Chapter 2, the photocatalytic degradation of lauric acid is more or less similar at humidity varying from 20% to 60%, while at 80% humidity water condensation takes place.[33] The photocatalytic activities were deduced from the evolution of the refractive index of the film by the photo-induced decomposition of the infiltrated lauric acid under UV-lamp irradiation.

Speed of LA decomposition were compared for each Ti/Si ratio, by plotting the evolution of the normalised LA/LA_0 with respect to irradiation time in Figure 3.18. LA is the

concentration of lauric acid at the irradiation time t and LA_0 is the initial concentration. The concentration of LA(t) was deduced by the refractive index values applying the BEMA model.

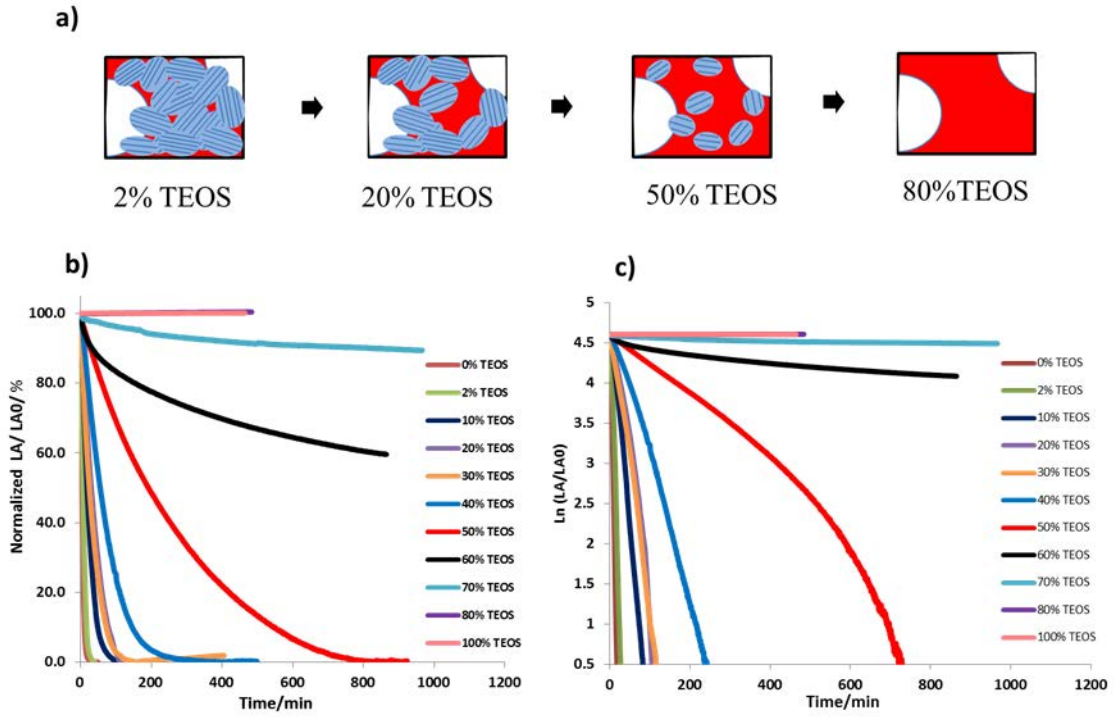

Figure 3.18 *a) Composite TiO_2/SiO_2 film structure evolution in which the blue particles represent the TiO_2 crystals and the red part represent silica (and titania) amorphous material; b) Plots of normalized LA/LA_0 vs time of UV irradiation; c) the corresponding first-order kinetic plots (ln(LA/LA0) vs t).*

It is observed that the elimination of lauric acid takes place for all the samples except the ones containing 80 and 100 % of SiO_2 for which the LA content doesn't change with time. The photocatalytic activity is observed only for the films containing anatase nanocrystals, as observed previously by GI-WAXS and HR-TEM. The efficiency of photocatalysis decreases with SiO_2 content, as expected. The scheme of the structure evolution is illustrated by Figure 3.18 a) where the blue particles represent the titania nanocrystals and the red parts for amorphous silica or titania matrix. For low SiO_2/TiO_2 ratio, the fraction of the TiO_2 nanocrystals, and their accessibility, are higher leading to a higher global photoactivity. Inversely, for higher silica content, a lower photocatalytic activity can be explained by the lower global TiO_2 content and to the fact that the nanocrystals are probably embedded in the amorphous silica network (and thus less accessible by the LA molecules). Other critical factors are likely to play a role in this global observation: (i) the crystals size decreases with

SiO_2 content; the constriction present in the porosity are more pronounced with SiO_2 content, affecting probably the molecular dynamics of LA, photoactive species and products of the reaction into the structure. In conclusion, the situation is quite complex. There are several reasons that contribute to the photocatalytic efficiency: 1) the amount of titania crystals; 2) the titania crystal size; 3) the porosity; 4) the accessibility to the porosity and the crystal surface where lay the scavengers.

The corresponding first-order kinetic plots (*ln(LA/LA0) vs t*) were shown in Figure 3.18 c). We can observe that, globally, the evolutions follow a pseudo- first-order kinetics, at least in the case of the active samples (%TEOS <50%). However, the first order kinetic behaviours (*ln(LA/LA0) vs t*) of the composite mesoporous TiO_2/SiO_2 films are not always linear (see Figure 3.19), suggesting that evolution rates is not only due to the progressive consumption of LA at the pore surface but also to other factors that evolve during the experiment, such as the water absorption on the pore surface as explained in chapter 2.

As seen by Figure 3.19 for the active samples, the fluctuation of (k) upon advancement of the experiments can be visualized using the corresponding derivatives $-d(\ln(LA/LA_0))/dt$ vs *t*. It is clear that different k(t) absolute values and tendencies results from different composition of the films. As the environmental conditions (40%RH, 20%O_2, and room temperature) and the concentration of impregnated lauric acid are all controlled to be similar, differences in k(t) are mainly governed by the films structure and composition. In general (and as expected) TiO_2-rich samples provide higher absolute values of k(t). Other considerations can be made. Firstly, differently from the case in Chapter 2, the initial activity, k at t=0 is not constant but it decrease from 0.1 min^{-1} for the pure TiO_2 film to 0.01 min^{-1} for the film containing 40% of SiO_2. We attributed the initial activity to the presence of OH and O_2 scavengers intrinsically adsorbed during handling and impregnation with LA. As shown in the scheme in Figure 3.20 for the samples 2% and 40% of SiO_2 at t=0, only the scavengers that are in contact with the active anatase surface will contribute at the initial activity of the process. Increasing SiO_2 content is accompanied by a decrease in active surface into the pores explaining the lower initial k value.

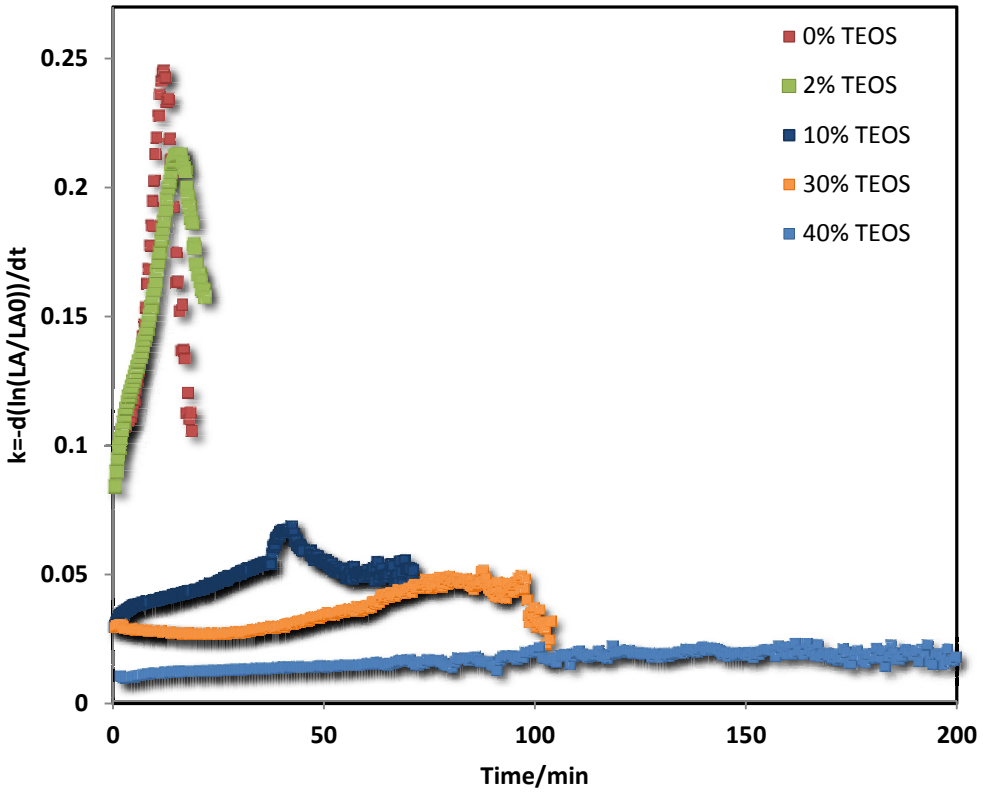

Figure 3.19 *-d(ln(LA/LA$_0$))/dt vs t plots in logarithm, representing the evolution of the kinetic constants k (min^{-1}) along the experiment progression for each component; inserted the route (i) and (ii) for decomposition of lauric acid.*

Secondly, similar tendencies were observed for samples from 0% TEOS to 30% TEOS. In the beginning, the kinetic constant goes up progressively since LA is decomposed at the anatase suface and liberates sites where H_2O and O_2 are adsorbed. Consequently, the concentration in scavengers increases with time, causing an acceleration of the reaction rate by, at least, a factor 1.5. After reaching a maximum, k(t) goes down progressively due to the fact that lauric acid was almost completely decomposed, which is the same tendency observed and explained in Chapter 2. Thirdly, the k (t) maxima (which stand for the nearly end of the decomposition reactions) shift to longer time with the increasing % TEOS; this behavior is obviously due to the fact that less active films require more time to decompose lauric acid. Fourthly, the k value is almost constant for the sample 40% TEOS that is characteristic of nearly perfect first-order kinetics. As proposed in the scheme in Figure 3.20, initially, part of the impregnated lauric acid molecules are in contact with TiO_2 crystal and the another part with the amorphous SiO_2 (or TiO_2) material. The lauric acid which is directly in contact with anatase TiO_2 could be readily decomposed freeing active sites to water to be absorbed. However, no increase in k(t) is observed with the time here. This behavior is due to

the fact that the reaction activity depends on the lauric acid concentration in the vicinity of the active site/species and not much from the radical's formation rate. The reaction is thus probably limited by (i) the lauric acid diffusion rate towards the (few) active sites or/and by (ii) the radicals' migration towards lauric acid molecules.

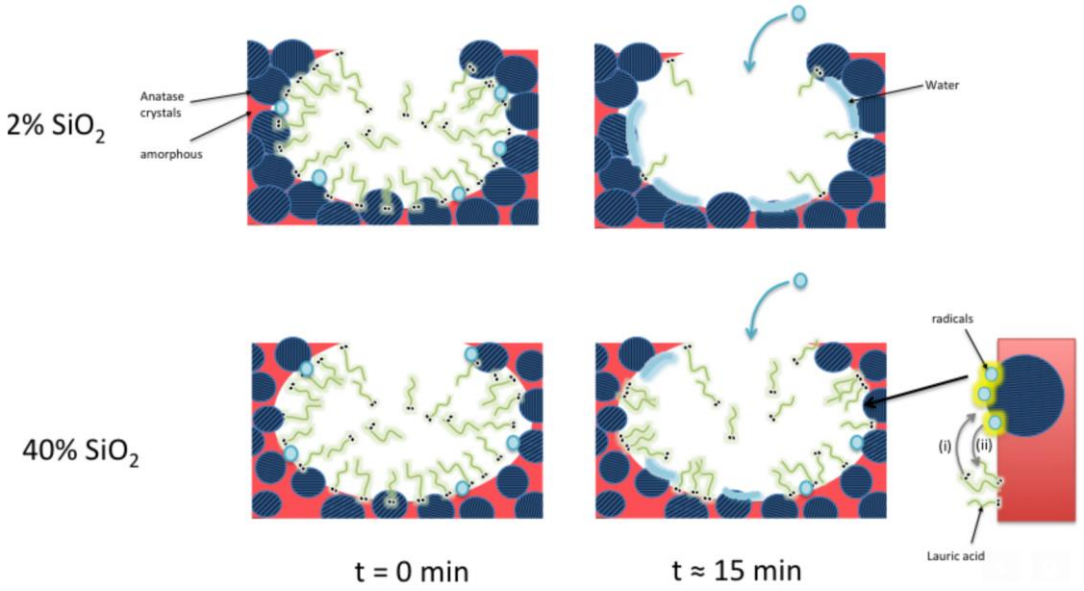

Figure 3.20 *Illustration of a possible mechanism occurring during LA decomposition into mesoporous composite SiO_2/TiO_2 with 2% and 40 % SiO_2 content at two representative times.*

From a practical point of view, the photocatalytic performance can be compared by evaluation the half-life time decomposition of lauric acid with increasing silica composition from 0% to 50%, which were calculated and represented by Figure 3.21. The decomposition reaction gradually gets slower and longer. For pure 100% titania film, it just took around 4.4 minutes to decompose half of the lauric acid content, while for 50% silica film, it took much longer time (around 192 minutes). Even if the decomposition is slower, the elimination efficiency of the 50% SiO_2 sample was still acceptable as compare to 60%TEOS, which decomposes 40% of lauric acid after 900 minutes irradiation. For 70%TEOS simple, less than 10% lauric acid was decomposed after 1000 minutes irradiation.

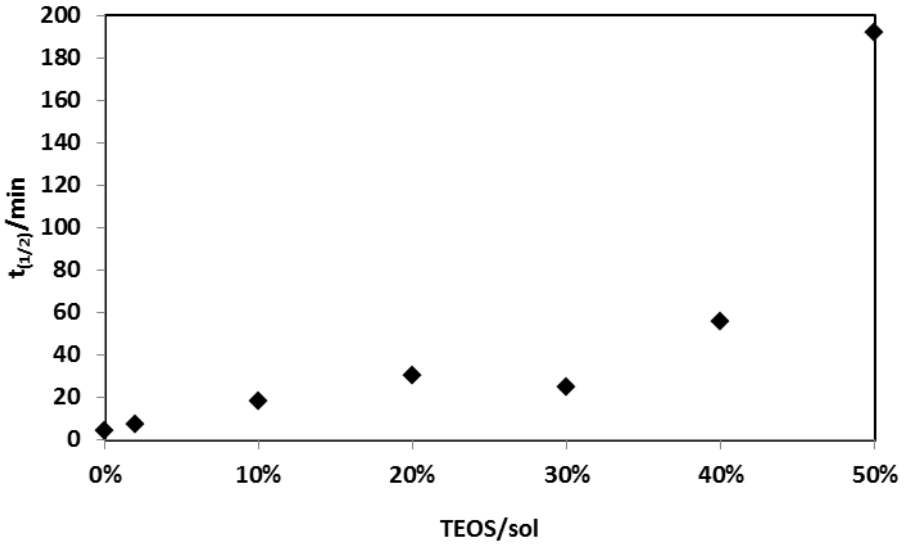

Figure 3.21 *Half life time decomposition with increasing TEOS composition from 0% to 50%.*

From the applicative point of view, it is interesting to highlight that the samples containing 40%SiO_2/60%TiO_2 that behaves as a transparent layer on glass is also performing quite well as photocatalytic coating. This suggests that this layer is a good candidate to be applied as optically transparent and photoactive (self-cleaning) coating. Another interesting point concerns the fact that, even if the photoactivity is not excellent for samples containing between 40 and 70% TEOS, they remain so and are anti-reflective at the same time.

3.7 Conclusion

In this chapter, mesoporous composite TiO_2/SiO_2 films with variable Ti/Si ratios have been synthesized using $TiCl_4$ and TEOS as titania and silica source and pluronic F127 as a template, via EISA associated to dip-coationg. EEP, SEM, GISAXS, GIWAXS, and HRTEM techniques have been used to systematically investigate the pore morphology and the wall structure. The results showed that, varying the porous structure evolves with the Si/Ti ratio. The obtained composited mesoporous titania/silica films showed tunable pore size (4.4-7.8 nm) and porosity (35 to 51%). We showed that the wall structures were finally formed with anatase crystals uniformly embedded in amorphous silica (or titania). The amorphous silica separate the anatase crystals which could prevent the Anatase species from growing. The

optical characterization indicates that the refractive index of the layers could be easily tuned by controlling the inorganic phase composition. This is important to potentially integrate such layers into optical devices (antireflective, Bragg-mirrors, transparent coatings…). Lauric acid was impregnated into the porous network to study the photocatalytic activities by in-situ ellipsometry. The mesoporous composite films with SiO_2 content < 40% exhibit remarkable photocatalytic activities. In particular we demonstrated that the mesoporous film with composition 40%SiO_2 60%TiO_2 is a good candidate to be used as optically transparent, photoactive, self-cleaning coating on glass.

References

1. Chien D M, Viet N N, Van N T K, et al. Characteristics modification of TiO_2 thin films by doping with silica and alumina for self-cleaning application[J]. Journal of Experimental Nanoscience, 2009, 4(3): 221-232.
2. Biju K P, Jain M K. Effect of crystallization on humidity sensing properties of sol–gel derived nanocrystalline TiO_2 thin films[J]. Thin Solid Films, 2008, 516(8): 2175-2180.
3. Yaacob M H, Sadek A Z, Latham K, et al. Optical H_2 sensing performance of anodized nanoporous TiO_2 thin films[J]. Procedia Chemistry, 2009, 1(1): 951-954.
4. Wang R, Hashimoto K, Fujishima A, et al. Light-induced amphiphilic surfaces[J]. Nature, 1997, 388: 431-432.
5. Houmard M, Riassetto D, Roussel F, et al. Enhanced persistence of natural super-hydrophilicity in TiO_2–SiO_2 composite thin films deposited via a sol–gel route[J]. Surface Science, 2008, 602(21): 3364-3374.
6. Maeda M, Yamasaki S. Effect of silica addition on crystallinity and photo-induced hydrophilicity of titania–silica mixed films prepared by sol–gel process[J]. Thin Solid Films, 2005, 483(1): 102-106.
7. Liu Y Y, Qian L Q, Guo C, et al. Natural superhydrophilic TiO_2/SiO_2 composite thin films deposited by radio frequency magnetron sputtering [J]. Journal of Alloys and Compounds, 2009, 479(1): 532-535.
8. Fresno F, Portela R, Suárez S, et al. Photocatalytic materials: recent achievements and near future trends[J]. Journal of Materials Chemistry A, 2014, 2(9): 2863-2884.
9. Sakthivel S, Kisch H. Daylight photocatalysis by carbon−modified titanium dioxide[J]. Angewandte Chemie International Edition, 2003, 42(40): 4908-4911.
10. Asahi R, Morikawa T, Ohwaki T, et al. Visible-light photocatalysis in nitrogen-doped titanium oxides[J]. science, 2001, 293(5528): 269-271.
11. Jimmy C. Synthesis of hierarchical nanoporous F-doped TiO_2 spheres with visible light photocatalytic activity[J]. Chemical Communications, 2006 (10): 1115-1117.
12. Zang L, Macyk W, Lange C, et al. Visible-light detoxification and charge generation by transition metal chloride modified titania[J]. Chemistry- A European Journal, 2000, 6(2): 379-384.
13. Louis B, Krins N, Faustini M, et al. Understanding Crystallization of Anatase into Binary SiO_2/ TiO_2 Sol− Gel Optical Thin Films: An in Situ Thermal Ellipsometry Analysis[J].

The Journal of Physical Chemistry C, 2011, 115(7): 3115-3122.

14. Pitoniak E, Wu C Y, Londeree D, et al. Nanostructured silica-gel doped with TiO_2 for mercury vapor control[J]. Journal of Nanoparticle Research, 2003, 5(3-4): 281-292.
15. Levene L, Thomas I M. Process of converting metalorganic compounds and high purity products obtained therefrom: U.S. Patent 3,640,093[P]. 1972-2-8.
16. Brinker C J, Scherer G W. Sol gel glass: I. Gelation and gel structure[J]. Journal of Non-Crystalline Solids, 1985, 70(3): 301-322.
17. Yoldas B E. Deposition and properties of optical oxide coatings from polymerized solutions[J]. Applied optics, 1982, 21(16): 2960-2964.
18. Kim S J, Park S D, Rhee C K, et al. Photocatalytic characteristics of homogeneously precipitated TiO_2 nano-sized powders[J]. Scripta materialia, 2001, 44(8): 1229-1233.
19. Aguado J, Van Grieken R, López-Munoz M J, et al. A comprehensive study of the synthesis, characterization and activity of TiO_2 and mixed TiO_2/SiO_2 photocatalysts[J]. Applied Catalysis A: General, 2006, 312: 202-212.
20. Kabra K, Chaudhary R, Sawhney R L. Treatment of hazardous organic and inorganic compounds through aqueous-phase photocatalysis: a review[J]. Industrial & engineering chemistry research, 2004, 43(24): 7683-7696.
21. Machida M, Norimoto K, Watanabe T, et al. The effect of SiO_2 addition in super-hydrophilic property of TiO_2 photocatalyst[J]. Journal of Materials science, 1999, 34(11): 2569-2574.
22. Kamalasanan M N, Chandra S. Sol-gel synthesis of ZnO thin films[J]. Thin Solid Films, 1996, 288(1): 112-115.
23. Wang P, Zakeeruddin S M, Exnar I, et al. High efficiency dye-sensitized nanocrystalline solar cells based on ionic liquid polymer gel electrolyte[J]. Chemical Communications, 2002 (24): 2972-2973.
24. Zribi M, Kanzari M, Rezig B. Structural, morphological and optical properties of thermal annealed TiO thin films[J]. Thin Solid Films, 2008, 516(7): 1476-1479.
25. Yamashita H, Ichihashi Y, Harada M, et al. Photocatalytic degradation of 1-octanol on anchored titanium oxide and on TiO_2 powder catalysts[J]. Journal of Catalysis, 1996, 158(1): 97-101.
26. Caruso F, Spasova M, Salgueiriño‐Maceira V, et al. Multilayer Assemblies of Silica‐Encapsulated Gold Nanoparticles on Decomposable Colloid Templates[J]. Advanced Materials, 2001, 13(14): 1090-1094.

27. Gao L, Zhang Q. Effects of amorphous contents and particle size on the photocatalytic properties of TiO_2 nanoparticles[J]. Scripta materialia, 2001, 44(8): 1195-1198.
28. Dong W, Sun Y, Lee C W, et al. Controllable and repeatable synthesis of thermally stable anatase nanocrystal-silica composites with highly ordered hexagonal mesostructures[J]. Journal of the American Chemical Society, 2007, 129(45): 13894-13904.
29. Li R, Faustini M, Boissière C, et al. Water Capillary Condensation Effect on the Photocatalytic Activity of Porous TiO_2 in Air[J]. The Journal of Physical Chemistry C, 2014, 118(31): 17710-17716.
30. Yang P, Zhao D, Margolese D I, et al. Generalized syntheses of large-pore mesoporous metal oxides with semicrystalline frameworks[J]. Nature, 1998, 396(6707): 152-155.
31. Li D, Zhou H, Honma I. Design and synthesis of self-ordered mesoporous nanocomposite through controlled in-situ crystallization[J]. Nature materials, 2004, 3(1): 65-72.
32. Choi S Y, Mamak M, Coombs N, et al. Thermally stable two-dimensional hexagonal mesoporous nanocrystalline anatase, meso-nc-TiO_2: Bulk and crack-free thin film morphologies[J]. Advanced Functional Materials, 2004, 14(4): 335-344.
33. Carretero-Genevrier A, Boissiere C, Nicole L, et al. Distance dependence of the photocatalytic efficiency of TiO_2 revealed by in situ ellipsometry[J]. Journal of the American Chemical Society, 2012, 134(26): 10761-10764.

CHAPTER 4 Conclusion

In this thesis, spectroscopic ellipsometry technique was used to study photocatalytic activity of TiO_2 and TiO_2/SiO_2 composite mesoporous films. Spectroscopic ellipsometry has been used as tool to characterize the materials structure, porosity and the films optical properties. In addition it has been adapted to characterize the photocatalytic properties of the systems in controlled environment and as function of the material structure and composition.

In the first part, the photocatalytic efficiencies of porous TiO_2 thin films were evaluated by following the refractive index diminution associated to the decomposition of impregnated organic pollutants. It offers here a simple, alternative and complementary method to evaluate the roles of the atmospheric composition in O_2 and H_2O on the reactivity. In the case in which lauric acid is used as pollutant we demonstrated that cleaning a porous semi-conductor films from its impregnated pollutant does not follow a strict-first order kinetic due to the fluctuation in O_2 and H_2O content in the pores as dictated by exchange equilibriums and accessibility of sites for scavenger stabilisation. It is proposed that higher efficiencies was obtained for an optimal ratio and repartition of scavenger/pollutant in the "moderate-dry" conditions, and when pores content liquid water from capillary condensation at high RH. In addition, this study proves that the evaluation of the photocatalytic activity of a given material performed in presence of liquid water is significantly different from that measured in atmosphere, especially for nanoporous photocatalysts (powder too). Thus, usual results of literature obtained from decomposition tests performed in solution should be taken with care whenever atmospheric photocatalysis application is targeted. We also investigate here the influence of the organic probe by using Methylene blue as pollutant and by discussing its efficacy to monitor photocatalysis. An optical model was developed to describe the optical response of the dye and its monomeric or dimeric forms. We highlight that photoreduction occurs when MB is used in O_2 free environments. Experiments in controlled humid atmosphere were conducted. By monitoring independently the real and the imaginary part of refractive index, the results on photodegradation rate suggested that MB can be used as probe for ellipsometric investigations in order to obtain information on the photodegration process and identify the formation of volatile or non-volatile products.

In the second part, in-situ ellipsometry was also used to investigate the morphology and

photocatalytic activity of mesoporous composite TiO_2/SiO_2 films with different Ti/Si ratios. The ordered films have been synthesized using $TiCl_4$ and TEOS as titania and silica source, Pluronic F127 as a template, via a synchronous assembly approach based on an ethanolic EISA process and by dip-coationg, respectively. EEP, SEM, GISAXS, GIWAXS, and HR-TEM techniques has been used to systematically investigate the pore morphology and wall structure. The results showed that the porous morphology varies from grid-like to worm-like structure. The obtained composite mesoporous titania/silica films shows tunable pore size (4.4-7.8 nm) and large porosity (0.35-0.51). The wall structures were finally formed by anatase crystals uniformly embedded in amorphous silica (or titania) which act as the wall surrounding the pores. The amorphous silica separated the anatase crystals which could prevent the anatase species from aggregating. Optical characterization indicates that the refractive index of the layers could be easily tuned by controlling the inorganic phase composition. This is important to potentially integrate such layers into optical devices (antireflective, Bragg-mirrors, transparent coatings…). Lauric acid was impregnated into the porous network to study the photocatalytic activities by in-situ ellipsometry. The mesoporous composite films with SiO_2 content < 40% exhibit remarkable photocatalytic activities. In particular we demonstrated that the mesoporous film with composition $40\%SiO_2/60\%TiO_2$ is a good candidate to be used as optically transparent, photoactive, self-cleaning coating on glass.

As a general conclusion, in-situ ellipsometry was proved to be a good tool to perform fundamental studies of photocatalytic processes into model thin films. However some further advancements can be proposed for the future.

Ellipsometry gives information about the kinetics of decomposition of non-volatile pollutant however the understanding of chemical processes taking place into the films remains a black-box. In this regards, it would be useful to couple ellipsometric analysis with other techniques (such as FTIR or GC) in order to determine the exact composition of the photocatalysis products. IR conducted some preliminary experiments but no significant data were measured due to the low amount of materials on the surface. These experiments would be also needed to confirm the validity of approach of MB to monitor the formation of volatile or non-volatile products.

In this regard, another perspective could be to further investigate the utilization of colored dye, as methylene blue, as a probe for ellipsometry. Concerning methylene blue some aspects

needs to be clarified such as the unusual initial absorption peak and the position evolution with RH.

In here, lauric acid and methylene blue were chosen to study the decomposition behavior. Lauric acid is composed by an alkyl chain (hydrophobic) and a carboxylic tail (hydrophilic) that can bind TiO_2; on the other hand methylene blue is hydrophilic (soluble in water) but not binding TiO_2. One could wonder how the structure and the chemical nature of the pollutant influence the photocatalysis. As function of their composition and structure, the pollutants are thus expected to be decomposed with different kinetics in air or liquid environments. A more systematic study would be interesting even involving a mixture of different pollutants (as in real conditions)

Another perspective consists in developing new photocatalytic films, for example active in the visible range. In my opinion, one interesting system is composed by gold nanoparticles supported on titania (Au/TiO_2). TiO_2 materials can only be excited by UV light (<360 nm); however less than 5% of sunlight is active for TiO_2. For real outdoor and indoor applications, the visible light from a nature source would be more convenient than UV light as excitation source. The most widely used approach to extend the photocatalytic response into the visible region has been doping the TiO_2 material with metals or non-metallic elements.[1-3] In general, it can be concluded that metal doping leads to unstable materials that undergo corrosion and in the long term the metal dopant undergoes leaching causing a gradual decay in the photocatalytic performance of the material.[4-6] On the other hand, doping by non-metallic element requires harsh preparation conditions and the degree of doping is difficult to determine with chemical analyses. Related to metal doping, but conceptually a different type of material, is when preformed TiO_2 is subsequently modified by depositing on the surface metal nanoparticles. The metal that modifies TiO_2 does not form part of the solid framework, but is in a separate phase in interfacial contact with semiconducting TiO_2. The mechanism is based on the gold photosensitization of titania by electron injection into the conduction band. It has a remarkable photostability. Preparation procedures of Au/TiO_2 have been well studied and extensively described, particularly for materials with low gold loading and small particle size.[7-9] One point it seems that the requirements in terms of optimum particle size, morphology and loading for photocatalytic reactions may not coincide exactly with those that are optimal for catalysis and this issue also need specific attention.[10] In this specific case, the gold particle would behave like non-decomposing dye that can be optically described by ellispometry as in the case of methylene blue. Therefore, it would be interesting to study

these structural aspects (and again the influence of the environmental conditions) with ellipsometry.

References

1. P. V. Kamat, Photochemistry on nonreactive and reactive (semiconductor) surfaces[J], Chem. Rev., 1993, 93, 267-300.
2. K. Takahama, N. Nakagawa, K. Kishimoto, JP 09192496 A 19970729, 1997.
3. Brezova V, Blažková A, Karpinský Ľ, et al. Phenol decomposition using M n^{+}/TiO_2 photocatalysts supported by the sol-gel technique on glass fibres[J]. Journal of Photochemistry and Photobiology A: Chemistry, 1997, 109(2): 177-183.
4. Fox M A, Dulay M T. Heterogeneous photocatalysis[J]. Chemical reviews, 1993, 93(1): 341-357.
5. Bekbölet M, Lindner M, Weichgrebe D, et al. Photocatalytic detoxification with the thin-film fixed-bed reactor (TFFBR): clean-up of highly polluted landfill effluents using a novel TiO_2-photocatalyst[J]. Solar Energy, 1996, 56(5): 455-469.
6. Hoffmann M R, Martin S T, Choi W, et al. Environmental applications of semiconductor photocatalysis[J]. Chemical reviews, 1995, 95(1): 69-96.
7. Kimling J, Maier M, Okenve B, et al. Turkevich method for gold nanoparticle synthesis revisited[J]. The Journal of Physical Chemistry B, 2006, 110(32): 15700-15707.
8. Xu Z C, Shen C M, Yang T Z, et al. From aqueous to organic: A step-by-step strategy for shape evolution of gold nanoparticles[J]. Chemical physics letters, 2005, 415(4): 342-345.
9. Buso D, Pacifico J, Martucci A, et al. Gold-Nanoparticle-Doped TiO_2 Semiconductor Thin Films: Optical Characterization[J]. Advanced Functional Materials, 2007, 17(3): 347-354.
10. primo A, Corma A, García H. Titania supported gold nanoparticles as photocatalyst[J]. Physical Chemistry Chemical Physics, 2011, 13(3): 886-910.

ABSTRACTS

Evaluation of photocatalytic activity of porous films by in-situ environmental ellipsometric analysis

Because of their exceptional intrinsic physical chemical properties, TiO_2-based materials have been extensively studied as potential material to be used in photocatalysis, as self-cleaning optical coatings, for solar energy conversion, for energy storage, or in sensing. In particular crystalline mesoporous thin films exhibit increased photocatalytic activities due to their exceptionally high surface area and to the high number of active sites. However the study and the optimization of the photocatalysis in such porous media are not easy to be done due to the fact that the catalytic process is highly dependent from several environmental and structural parameters. The research activities of this thesis were essentially focused on (i) the fabrication of mesoporous TiO_2-based photoactive thin films with tunable composition and nanostructure and (ii) their utilization as platform for fundamental study of the photocatalytic process by in-situ ellipsometry. The mesoporous films with tunable nanostructure will be fabricated by coupling sol-gel chemistry, block-copolymer self-assembly and highly controlled liquid deposition techniques. Among modern analytical tools, 2D-GISAXS, ellipsometry and ellipso-porosimetry, SEM-FEG, HR-TEM and WAXS, were used to obtain a large set of relevant information on such layers. In the first part, a model TiO_2 mesoporous film was analysed by in-situ ellipsometry for fundamental investigations of the photocatalytic process kinetics in air as function of the environmental composition (O_2 and humidity) and the organic pollutant (lauric acid or methylene blue). The large amount of information obtain by in-situ ellipsometry has allowed the proposition of photodegradation mechanisms in the studied conditions. In the second part, composite mesoporous TiO_2/SiO_2 films with tunable optical properties were fabricated by sol-gel chemistry. A structural study on the films porous network and composition was conducted. In-situ ellispometry was also used to determine the photodegradation kinetics into the composite films and to clarify the photocatalytic mechanism.

Evaluation de l'activité photocatalytique de films poreux par analyse ellipsométrique environnementale in-situ

Du fait de leurs exceptionnelles propriétés intrinsèques physico-chimiques, les matériaux à base de TiO_2 ont déjà été très étudiés comme matériaux prépondérants pour être utilisés aussi bien dans le domaine de la photocatalyse, que pour les revêtements optiques autonettoyants, pour la conversion d'énergie solaire, pour le stockage d'énergie, ou encore pour la détection. En particulier, les films minces mésoporeux cristallins de TiO_2 montrent une activité photo-catalytique élevée due à leur surface spécifique incomparable ainsi qu'à leur grand nombre de sites actifs. Cependant, l'étude et l'optimisation de la photocatalyse dans un tel milieu poreux n'est pas si simple car le processus catalytique dépend de plusieurs paramètres environnementaux et structuraux. Les activités de recherche inhérentes à cette thèse se sont essentiellement focalisées sur (i) la conception de couches minces mésoporeuses à base de TiO_2 avec une composition et une nanostructure variée et (ii) leur mise en œuvre comme plateforme pour une étude fondamentale par ellipsométrie *in-situ* concernant le processus photocatalytique. Des films minces mésoporeux avec une nanostructure ajustable ont été produits en couplant la chimie sol-gel, l'auto-assemblage de copolymères à blocs, et des procédés de dépôt liquide parfaitement contrôlés. Parmi des outils de caractérisation analytiques modernes, 2D-GISAXS, ellipsométrie, porosimétrie par ellipsométrie, SEM-FEG, HR-TEM et WAXS sont notamment les techniques qui ont été utilisées pour obtenir une large gamme d'informations sur les couches minces ainsi produites. Dans la première partie du manuscrit, un modèle de film mésoporeux de TiO_2 a été analysé par ellipsométrie *in-situ* pour des investigations fondamentales sur les cinétiques du processus photocatalytique dans l'air en fonction de la composition environnementale (O_2 ou humidité) et du polluant organique (acide laurique ou bleu de méthylène). La grosse quantité d'information obtenue par ellipsométrie *in-situ* a d'ailleurs permis la proposition de mécanismes de photo-dégradation dans les conditions étudiées. Dans la seconde partie du manuscrit, des films minces mésoporeux mixtes TiO_2/SiO_2 avec des propriétés optiques ajustables ont été préparées par voie sol-gel. Une étude structurale a été conduite sur le réseau et la composition des films poreux. L'ellipsométrie *in-situ* a été également mis en œuvre pour déterminer les cinétiques de photo-dégradation à l'intérieur de ces films mixtes et pour clarifier le méchanisme photocatalytique.